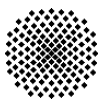


**On the Influence of the Reso-
nance Scattering Treatment in
Monte Carlo Codes on High
Temperature Reactor Charac-
teristics**

Björn Becker



**On the Influence of the Reso-
nance Scattering Treatment in
Monte Carlo Codes on High
Temperature Reactor Charac-
teristics**

von der Fakultät Energie-, Verfahrens-
und Biotechnik der Universität Stuttgart
zur Erlangung der Würde eines
Doktor-Ingenieurs (Dr.-Ing.)
genehmigte Abhandlung

vorgelegt von

Ingénieur Diplômé, M. Eng.

Björn Becker

geboren in Marburg.

Hauptberichter:
Prof. G. Lohnert, Ph.D.

Mitberichter:
Prof. Dr. V. Heinzel

Tag der Einreichung: 09.12.2009

Tag der mündlichen Prüfung: 04.03.2010

ISSN – 0173 – 6892

Juni 2010

IKE 6 - 206



Acknowledgments

I would like to express my gratitude to my advisor Dr. habil. Ron Dagan. The preparation of this work would not have been possible without his support and patience. I am deeply indebted to Prof. Lohnert for his constant support and essential questions. I am furthermore thankful for the assistance and encouragement of Prof. Heinzl.

This work was performed at the Institute for Neutron Physics and Reactor Technology of the Karlsruhe Institute of Technology. I want to express my gratitude to all my colleagues, notably to Dr. Broeders and Mr. M. Becker.

I want to thank Prof. Danon from RPI for explaining his experimental method to validate the resonance dependent scattering kernel.

Financial support for this work was given by the EnBW Kernkraft GmbH. In particular I want to thank Dr. Herrling, Dr. Vogel, Mrs. Schölch and Mrs. Lübben.

Contents

Content	5
List of Figures	7
List of Tables	9
Abstract	11
Introduction	13
1 Neutron Cross Section Theory	15
1.1 Cross Sections	15
1.1.1 General Description of Resonances	15
1.1.2 Resonance Models	18
1.2 Scattering Kernel	21
1.2.1 Angular Expansion of the Scattering Kernel	21
1.2.2 Energy Moments of the Scattering Kernel	22
1.2.3 Asymptotic Scattering Kernel	22
1.3 Doppler Broadening Theory	25
1.3.1 Temperature Dependent Cross Sections	26
1.3.2 Temperature Dependent Scattering Kernel	28
1.4 The Scattering Kernel in the Transport Equation	31
2 A New Developed Stochastic Doppler Broadening Method	33
2.1 The Code <i>DOPPLER-MC</i>	33
2.2 Comparison of the Analytic and Stochastic Doppler Broadening Methods	34
3 The DBRC Method for the Resonance Dependent Scattering Kernel in MC Codes	41
3.1 The Sampling of the Velocity of the Target Nucleus Method	41
3.2 The new DBRC Method	42
3.3 Comparison of the new DBRC and the Standard MCNP Scattering Model	44
3.3.1 Energy Transfer Kernel	45
3.3.2 Up- and Down-Scattering Probabilities	46
3.3.3 Energy Moments of the Scattering Kernel	47
3.3.4 Angular Moments of the Scattering Kernel	47
3.4 The $S(\alpha, \beta)$ Probability Table Method	48
3.5 Summary	50
4 Validation of the DBRC Model	51
4.1 RPI ^{238}U and ^{232}Th Scattering Experiment	51

4.2	nTOF ^{232}Th Experiment	54
4.3	Comparison of DBRC and $S(\alpha, \beta)$ Based MCNP Calculations	55
4.4	Summary	56
5	Impact of the Resonant Dependent Scattering Kernel on HTR	57
5.1	High Temperature Reactors	57
5.1.1	HTR Design Characteristics	58
5.1.2	Current HTR Designs	59
5.2	HTR Unit Cell Calculations	64
5.2.1	TRISO Matrix Unit Cell Study	64
5.2.2	HTR Fuel Pebbles	70
5.2.3	HTR Fuel Compacts	77
5.3	HTR-PM Core Calculations	81
5.3.1	Impact of the DBRC Kernel on the HTR-PM Criticality	82
5.3.2	Impact of the DBRC Kernel on the HTR-PM Doppler Reactivity Coefficient	83
5.3.3	Estimation of the Criticality Shift due to Higher ^{239}Pu Content	85
5.4	Summary	87
	Conclusion and Outlook	89
	Bibliography	91
	Nomenclature	97

List of Figures

1.1	Total, elastic and radiative capture cross section of ^{238}U at 300 K	16
1.2	Total resonance cross section of ^{238}U at 6.67 eV at 300 K	17
1.3	Schematic of entrance and exit channels as used in scattering theory . . .	19
1.4	Trajectories of a neutron and a target nucleus before and after a scattering event in the laboratory reference frame (a,b) and in the center of mass reference frame (c,d), zero Kelvin approximation	23
1.5	Asymptotic scattering kernel of ^{238}U at 6.67 eV	24
1.6	Doppler effect widening of the 6.67 eV resonance scattering cross section of ^{238}U	25
1.7	Wigner-Wilkins scattering kernel of ^{238}U at 6.67 eV and 1200 K	30
1.8	Resonance dependent scattering kernel of ^{238}U at 6.67 eV and 1200 K . .	31
2.1	Scheme of the <i>DOPPLER-MC</i> program	35
2.2	Convergence of the stochastic Doppler broadening algorithm for the scattering and total cross section of ^{238}U at 1200 K and 36.67 eV	36
2.3	Stochastic and analytic Doppler broadening of scattering and total cross section of ^{238}U at 1200 K and 600 K	37
2.4	Stochastic and analytic Doppler broadening of the scattering cross section of ^{232}Th in the energy region from 0.0001 eV to 0.01 eV at 300 K and 3000 K	38
2.5	Stochastic Doppler broadening of the (n, α) cross section of ^{10}B at different temperatures	38
2.6	Stochastic and analytic resonance dependent scattering kernel of ^{238}U at 6.53 eV and 1200 K	39
2.7	Stochastic and analytic resonance dependent scattering kernel of ^{232}Th at 23.2 eV and 1200 K	40
3.1	Stochastic resonance dependent kernel (DBRC) and constant cross section kernel (std. MCNP) of ^{238}U at 6.67 eV and for various temperatures . . .	45
3.2	Stochastic resonance dependent kernel (DBRC) and constant cross section kernel (std. MCNP) of ^{238}U at 6.53 eV and for various temperatures . . .	46
3.3	Up- and down-scattering probabilities (std. MCNP and DBRC) and scattering cross section of ^{238}U at 1200 K	47
3.4	Energy moments and mean energy change of ^{238}U scattering kernel at 1000 K (std. MCNP and DBRC)	48
3.5	First angular moment of the ^{238}U scattering kernel at 6.5 eV and 1000 K (std. MCNP and DBRC)	49
3.6	Second angular moment of the ^{238}U scattering kernel at 6.5 eV and 1000 K (std. MCNP and DBRC)	49
4.1	RPI scattering experiment for ^{238}U	52

4.2	Comparison of the simulated and experimental ^{232}Th resonance scattering-counts for thin ^{232}Th sample	53
4.3	Comparison of the simulated and experimental ^{232}Th resonance scattering-counts for thick ^{232}Th sample	53
4.4	nTOF ^{232}Th capture yield experiment	54
5.1	TRISO coated particle	59
5.2	The Chinese HTR-10	60
5.3	The Japanese HTTR	60
5.4	The HTTR fuel compact, rod and assembly	61
5.5	The HTR-MODUL reactor	63
5.6	Difference of criticality between DBRC and std. MCNP based calculations for different TRISO matrix packing fractions and temperatures	66
5.7	Neutron spectrum for different TPF at $T_f=1200\text{ K}$	67
5.8	Relative difference of the (n,γ) reaction rate of ^{238}U of DBRC and std. MCNP based calculations for different packing fractions	68
5.9	Comparison of neutron flux in the vicinity of four ^{238}U resonances for DBRC and std. MCNP based calculations (TPF=35 % and $T_f=1200\text{ K}$)	68
5.10	Difference in criticality between DBRC and std. MCNP based calculations for different HM contents and fuel temperatures	71
5.11	Pebble unit cell reactivity calculated with DBRC and std. MCNP for different HM contents per pebble and fuel temperatures	72
5.12	Pebble unit cell Doppler reactivity coefficient calculated with DBRC and std. MCNP for different HM contents and fuel temperatures	73
5.13	^{239}Pu inventory per pebble during burn up and difference depending on scattering model (5 g HM per pebble case)	74
5.14	^{239}Pu inventory per pebble during burn up and difference depending on scattering model (10 g HM per pebble case)	74
5.15	Neutron flux in the vicinity of the 69 eV ^{232}Th resonance	76
5.16	HTTR pin cell model	77
5.17	HTTR block model	79
5.18	Spectral zones of HTR-PM in ZIRKUS	81
5.19	Reactivity of the HTR-PM equilibrium core at different fuel temperatures calculated with DBRC and std. MCNP	84
5.20	Doppler reactivity coefficient of the HTR-PM equilibrium core at different fuel temperatures calculated with DBRC and std. MCNP	84
5.21	^{239}Pu concentration during burn up of HTR-PM unit cell for different fuel temperatures calculated with the DBRC and with the standard. MCNP versions	85
5.22	Increase of the ^{239}Pu concentration calculated with DBRC relative to standard MCNP calculation for an HTR-PM unit cell and different fuel temperatures	86

List of Tables

4.1	Criticality k_{∞} of a LWR pin cell at $T_F=1200$ K applying different scattering models	56
4.2	Capture reaction rate of a LWR pin cell at $T_F=1200$ K applying different scattering models	56
5.1	HTR operating in the past	58
5.2	HTR-10 like TRISO particle design	60
5.3	Criticality of the TRISO matrix in dependence of TRISO packing fraction (TPF) and fuel temperature	65
5.4	Resonance parameter of ^{238}U s-wave resonances between 0 and 210 eV . .	69
5.5	Influence of the ^{238}U resonance dependent scattering kernel of specific energy intervals	69
5.6	Criticality of a pebble unit cell for different HM contents and fuel temperatures	71
5.7	Fuel group cross section of HTTR pin cell models for std. MCNP and DBRC based calculations	78
5.8	Criticality of a hexagonal block unit cells for different fuel temperatures .	80
5.9	Criticality of the HTR-PM reactor with different scattering models . . .	82
5.10	Criticality of the HTR-PM core with additional ^{239}Pu	86

Abstract

The different interactions of neutrons in a nuclear reactor like absorption, production or scattering are generally introduced by solving the well known Boltzmann transport equation. Its solution scheme is based on the balance between losses and gain of neutrons. It turns out that all commonly practical ways to solve this basic equation exhibit an intrinsic inconsistency. The neutron scattering loss term includes explicitly the impact of the temperature and cross section shape on the interaction probability, namely the Doppler broadening of the integral scattering cross section. However, the calculations of the neutron gain based on the above mentioned scattering event assumes zero Kelvin temperature and ignores the shape of the cross section. For heavy nuclei with pronounced resonances like ^{238}U this inconsistency leads to noticeable errors in the evaluation of core parameters as was shown by Ouisloumen and Sanchez^[1], and Rothenstein and Dagan^[2] who developed the correct resonance dependent scattering kernel.

In this work, a new approach, namely a stochastic method is presented for the calculation of the Doppler broadened integral cross sections as well as for the new developed resonance dependent scattering kernel. A stochastic methodology, based on an idea of Rothenstein^[3], named as the “Doppler Broadening Rejection Correction” (DBRC) is implemented as a solver for the above mentioned missing resonance dependent kernel in the scattering treatment of Monte Carlo (MC) codes. The flexibility of using the unique form of a rejection method is confirmed, for the first time, by comparing it to the analytic $S(\alpha, \beta)$ scattering tables approach^[4]. However, the DBRC scheme allows for a much wider and practical use of the improved scattering kernel theory. In addition, the DBRC method is validated by several experiments in particular by a dedicated ^{232}Th scattering experiment done at the Gaerttner Institute of the Rensselaer Polytechnic Institute (RPI) in the USA.

The influence of this new, stochastic resonance dependent scattering kernel on core parameters is extensively investigated for High Temperature Reactors (HTR). Both, pebble bed and block type HTR designs are considered. A significant impact is found in unit cell calculations as far as criticality, reaction rates and Doppler reactivity coefficients are concerned. The criticality decreases up to 1.20 % (depending on temperature and on the HTR design). The Doppler coefficient is found to be more negative by up to 10 %. In addition, the neutron flux shape in the vicinity of resonances and the fuel inventory during burn up change noticeably when the new resonance model is applied.

Further on, for industrial relevant purposes, it is shown that for a full scale model of the Chinese HTR-PM reactor, the DBRC kernel leads to a reactivity decrease of about 0.20 % and renders the Doppler reactivity coefficient being more negative by about 6 % to 8 %.

Zusammenfassung

Die verschiedenen Wechselwirkungen von Neutronen in einem Kernreaktor wie zum Beispiel Absorption, Produktion und Streuung werden im Allgemeinen durch die Lösung der Boltzmanntransportgleichung beschrieben. Vereinfacht ausgedrückt bilanziert diese den Verlust gegen den Gewinn von Neutronen. Dabei weisen die üblichen Lösungsmethoden insofern eine Inkonsistenz auf, als sie im Neutronenverlustterm den Einfluss von Tem-

peratur und Wirkungsquerschnittsform auf die Streuwahrscheinlichkeit von Neutronen, die so genannte Dopplerverbreiterung des integralen Streuwirkungsquerschnitts, explizit berücksichtigt. Für den Neutronengewinnterm hingegen werden diese Effekte unter der Annahme der Neutronenstreuung an ruhenden Kernen (“Null-Grad-Kelvin-Näherung”) vernachlässigt. Für schwere Nuklide mit einer stark ausgebildeten Resonanzstruktur, wie zum Beispiel ^{238}U , führt diese Inkonsistenz zu deutlichen Fehlern bei der Berechnung von Kernparametern. Dies wurde von Ouisloumen und Sanchez^[1] und von Rothenstein und Dagan^[2], die den exakten, resonanzabhängigen Streukern entwickelt haben, gezeigt.

In dieser Arbeit wird eine neue, stochastische Methode für die Berechnung von Doppler verbreiterten, integralen Wirkungsquerschnitten wie auch des resonanzabhängigen Streukerns vorgestellt. Des Weiteren wird basierend auf einer Idee von Rothenstein^[3] mit Hilfe einer stochastischen Methode, der so genannten “Doppler Broadening Rejection Correction” (DBRC), der resonanzabhängige Streukern in die Streubehandlung von Monte Carlo (MC) Codes eingefügt. Erstmals wird diese “Rejection” Methode durch einen Vergleich mit analytischen $S(\alpha, \beta)$ Tabellen^[4] bestätigt. Das DBRC Schema ermöglicht hierbei eine allgemeinere und praktischere Verwendung der erweiterten Resonanzstreuungstheorie. Die DBRC Methode wurde darüber hinaus durch zahlreiche Experimente validiert. Insbesondere wird ein ^{232}Th Streuexperiment, welches am Gaerttner Institut des Rensselaer Polytechnic Institute (RPI) in den USA durchgeführt wurde, zur Validierung herangezogen.

Der Einfluss des neuen, stochastischen und resonanzabhängigen Streukerns auf die neutronenphysikalischen Eigenschaften von Hochtemperaturreaktoren (HTR) wird in dieser Arbeit detailliert untersucht. Sowohl für Kugel- als auch Blockdesigns konnten in Einheitszellrechnungen im Vergleich zu üblichen Verfahren deutliche Unterschiede bezüglich der Kritikalität, Reaktionsraten und Dopplerreaktivitätskoeffizienten nachgewiesen werden. Die Kritikalität sinkt, abhängig von der Temperatur und des HTR Designs, um bis zu 1.2 % ab. Der Dopplerreaktivitätskoeffizient wird um bis zu 10 % negativer. Zusätzlich ändern sich der Neutronenflussverlauf in der Nähe von Resonanzen und das Brennstoffinventar während des Abbrandes merklich, wenn das neue Streumodell angewendet wird.

Zuletzt wurde ein vollständiges Modell des chinesischen HTR-PM Reaktors untersucht. Das DBRC Streumodell führt zu einer Reduktion der errechneten Kritikalität um 0.2 %. Der Dopplerreaktivitätskoeffizient wird um ca. 6 % bis 8 % negativer.

Introduction

The early developments of nuclear reactor engineering in the middle of the last century allowed for the construction of the first critical reactor, Chicago Pile-1, of the Manhattan project and the first electricity producing reactor the Obninsk Nuclear Power Plant. Since then the endeavor in mathematical and numerical methods concerning nuclear reactor theory has been growing steadily. Major efforts have been directed toward improving the approximation techniques used to solve the basic neutron transport (Boltzmann) equation, which govern the description of neutrons reactions within a nuclear reactor. The development of new fast computers increased the capability of more accurate numerical deterministic codes to solve the Boltzmann equation employing fine geometry meshes with a large number of neutron energy groups allowing for enhanced accuracy. Moreover, the use of stochastic codes with very detailed geometry and continuous energy description of the neutron was significantly increased. These codes are also known as Monte Carlo (MC) codes.

Even though significant progress has been made for analytic (deterministic) and MC techniques, several physical phenomena have not been solved completely. One of the approximations concerns the prediction of the neutrons energy and flight direction after a scattering interaction with a nucleus. The general description of the secondary energy and angular distribution of neutrons is referred to as the so-called scattering kernel which is the double differential part of the scattering cross section. Commonly, the assumption was made that the impact of the cross section (resonance) shape and of the temperature on the scattering kernel is negligible. Thereafter, the asymptotic (0 K) scattering kernel was used. This assumption is incorrect for heavy nuclei such as ^{238}U with pronounced resonance structures^[1,2]. In addition, it causes an inconsistency in the very basic solution of the Boltzmann equation. The integral cross section explicitly includes the temperature and resonance shape effects (the well known Doppler broadening definition) whereas its differential part which also appears within the transport equation ignores these effects. Furthermore the effect of the correct scattering kernel on light water reactors was shown to be significant^[5,4].

In this work, the resonances scattering kernel theory is extended and further developed. In particular, the use of stochastic methods is specifically explored. Alternative stochastic Doppler broadening methods are introduced for the calculation of the integral as well as the differential part of the scattering cross section. Consequently, the need for correcting the inconsistency within the Boltzmann equation is highlighted. By applying a stochastic formalism for the resonance dependent scattering kernel in MC codes as proposed by Rothenstein^[3], it becomes possible, for the first time, to confirm the analytical solution for the secondary energy distribution of Rothenstein^[5] and Dagan^[4]. This new implemented scheme allows for a much wider and practical use of the improved scattering kernel theory. In this work, the new introduced, stochastic method is validated by dedicated scattering experiments performed at the Rensselaer Polytechnic Institute (RPI).

Furthermore, the possibility of calculating innovative core concepts more accurately is improved in comparison to the $S(\alpha, \beta)$ approach for resonant materials as suggested by Dagan^[4].

In this study, the influence of this new, stochastic resonance dependent scattering kernel is extensively investigated for high temperature reactors (HTR). HTRs are part of the future generation of nuclear reactors, namely the Generation IV type reactors^[6]. In general, the Generation IV reactor types are believed to have highly improved nuclear safety, improved proliferation resistance and minimized waste production, and being at the same time highly economical. Most of these designs are not expected to be available for commercial construction before 2030 with exception of the Chinese HTR-PM-500 which is already in the construction phase. The modular HTR design is currently the most advanced HTR concept which is based on inherent safety and economic competitiveness.

In this work, representative unit cell calculations are analyzed for various HTR designs and the impact of the new scattering kernel on safety relevant core parameters is deducted. Special emphasis is placed on the resonance scattering kernel of ^{238}U . A detailed model of the Chinese HTR-PM reactor is used to investigate the influence of the resonance dependent scattering kernel and also on its equilibrium core parameters.

Based on the above introduction, the work is organized in the following manner:

1. In the first chapter the relevant theory of neutron cross section and, in particular the cross section resonances are introduced. The effect of temperature, i.e. Doppler broadening, on cross sections and notably on the scattering kernel is introduced. The analytic Doppler broadening models are discussed with emphasis on the broadening of the scattering kernel in the vicinity of resonances.
2. In the second chapter, a new stochastic methodology for Doppler broadening of cross sections and of the scattering kernel is introduced and compared to analytic methods.
3. In the third chapter, the implementation of the resonance dependent scattering kernel into MC codes is presented by exemplary use of MCNP. The use of analytic scattering tables is identified. A new developed, stochastic method, the so called *Doppler Broadening Rejection Correction* (DBRC) is highlighted. The deviations from the default MCNP scattering kernel are pointed out and analyzed.
4. The fourth chapter gives a validation of the DBRC scattering model by the use of two different dedicated scattering experiments using ^{238}U and ^{232}Th targets. A comparison between the new DBRC and the analytic models is made for a simple unit cell.
5. The fifth chapter discusses the influence of the resonance dependent scattering kernel on High Temperature Reactors. The analyzed models include very basic unit cell calculations of fuel particles in a graphite matrix, unit cell calculations of spherical and cylindrical fuel elements, and finally reach a full core model of the HTR-PM reactor. Aspects like criticality, Doppler reactivity coefficient and fuel inventory during the fuel cycle are discussed.

The work is completed by a conclusion and an outlook.

1 Neutron Cross Section Theory

In this chapter, the relevant theory of neutron cross section is presented. A special emphasis is made on the resonance cross section and the scattering kernel since the combination of those form the essence of this work. The dependence of the cross sections on temperature, namely the Doppler broadening, is discussed.

For a detailed study of neutron resonance cross sections one should address to standard nuclear engineering books (e.g. Bell and Glasstone^[7], Stacey^[8]) in addition to more specific publications (e.g. Fröhner^[9], Lynn^[10], Bethe^[11], Vogt^[12]).

1.1 Cross Sections

The interaction probability of neutrons with matter in space is based on the concept of neutron cross sections. It is represented by a cross sectional area of a nucleus which is the probability for an interaction with the oncoming neutron and is expressed in area units called barns ($1 b = 10^{-24} \text{ cm}^2$). Several reaction processes are possible when a nucleus, e.g. ^{238}U , is bombarded by a neutron whereas each reaction type x (also called reaction channel) is represented by its own specific cross section σ_x .

In nuclear reactors one distinguishes between two interactions. The first one is a direct interaction of the neutron with the target nucleus in a one-step process e.g. potential scattering σ_p . The cross section of this hard sphere scattering is about the size of the geometrical cross section of the nucleus (several barns).

The second process is a two-step interaction. The neutron and the target form a so-called compound nucleus (CN). This nucleus exists for a certain time and decays subsequently by various possible decay channels: e.g. elastic scattering (σ_s), inelastic scattering ($\sigma_{s'}$), radiative capture (σ_γ), fission (σ_f) or other reactions involving different secondary particles like protons ($\sigma_{(n,p)}$) or alpha particles ($\sigma_{(n,\alpha)}$).

All specific cross sections sum up to the total interaction probability namely the total cross section σ_t .

$$\sigma_t = \sigma_\gamma + \sigma_f + \sigma_s + \sigma_{(n,\alpha)} + \dots \quad (1.1)$$

1.1.1 General Description of Resonances

Neutron cross sections depend on the energy of the neutron. The scattering cross section of ^{238}U for example may rise by several magnitudes at specific energies (see figure 1.1). This behavior is called a resonance of the cross section. Similar behavior as the scattering cross section shows the capture cross section at the very same energies. The space between the distinct resonances decreases with increasing energy. Figure 1.1 shows that the scattering cross sections exhibits a dip on the lower energy side of the resonance. This dip is due to the interference range of the potential and resonance scattering. The capture resonance on the other hand is fully symmetric.

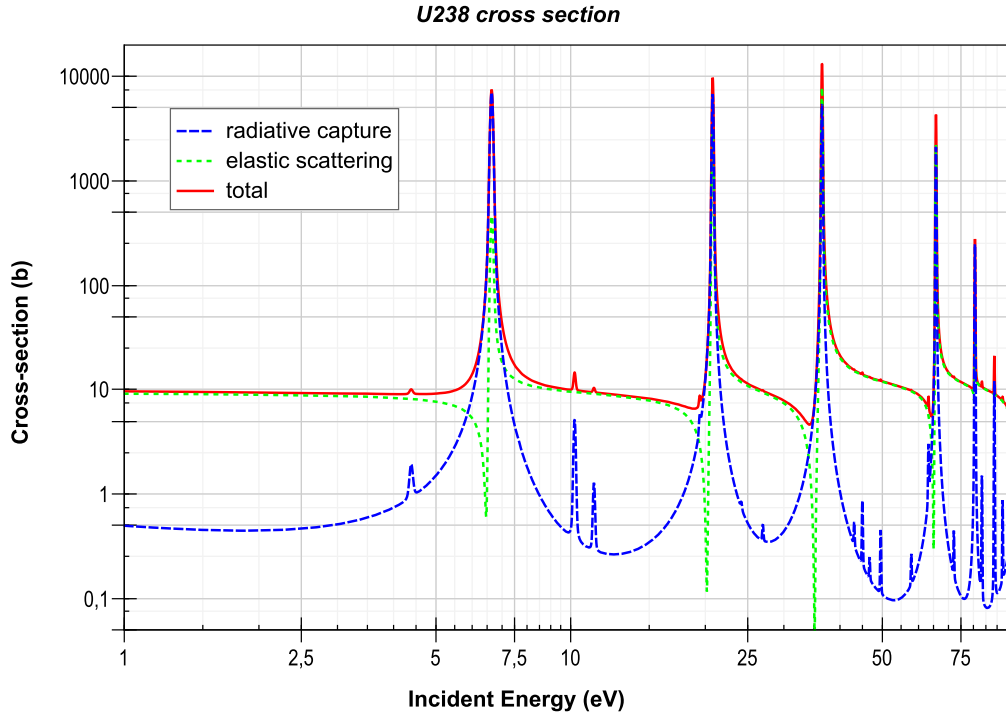
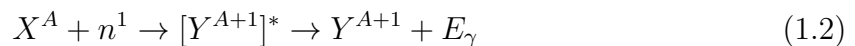


Figure 1.1: Total, elastic and radiative capture cross section of ^{238}U at 300 K^[13,14]

Figure 1.2 shows the total cross sections in the vicinity of the first ^{238}U resonance at 6.67 eV. A cross section resonance is characterized by the resonance energy E_0 , the peak cross section σ_{max} as well as by the resonance widths Γ at half maximum $\frac{1}{2}\sigma_{max}$. Each reaction x has its very own width Γ_x . The ratio of the reaction width to the width of the total cross section Γ denotes the relative reaction probability. The ratio Γ_n/Γ gives for example the relative probability of resonance scattering, where Γ_n is the scattering width.

The distinct resonance structure of the neutron cross section of most heavy nuclei and of some light nuclei arises from the formation of the compound nucleus of the neutron and the target based on Bohrs compound nucleus theory^[15]. The neutron enters the target nucleus X of mass number A and a compound nucleus Y of mass $A + 1$ is formed. This nucleus is unstable due to its high excitation energy state (indicated by an asterisk in formula 1.2). Therefore, after its formation the compound nucleus decays by expulsion of one or several particles (n , α , p , γ) or by breaking in a fission process. A radiative capture process for example can be allegorized by:



The excitation energy E^* is the sum of the kinetic energy E of the incident neutron and of the binding energy E_B of the absorbed neutron in the compound system:

$$E^* = E_B + E \quad (1.3)$$

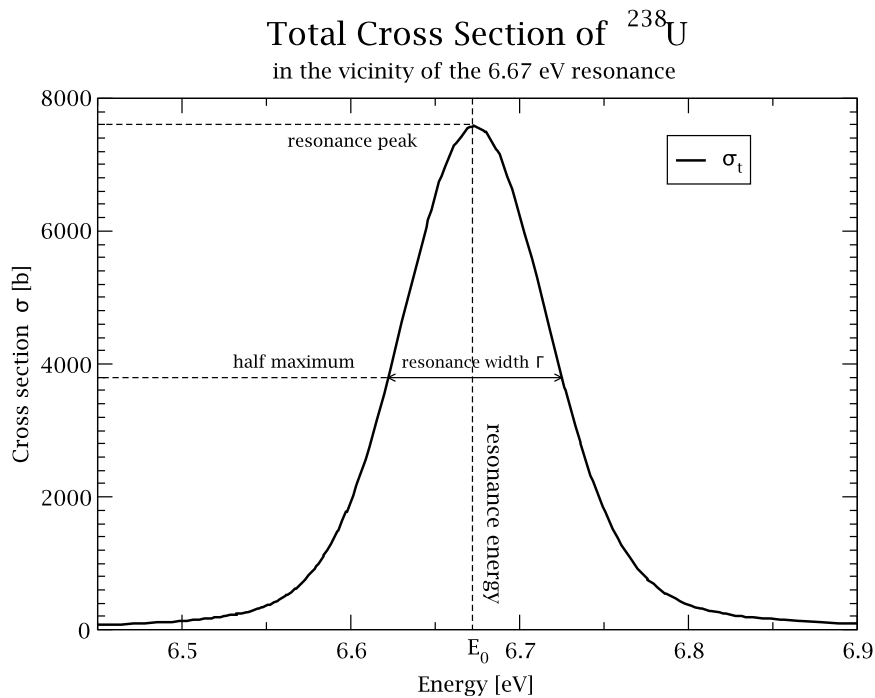


Figure 1.2: Total resonance cross section of ^{238}U at 6.67 eV at 300 K

The compound-nucleus formation favors specific neutron energies to obtain a definite quantum state of the formed nucleus. The excitation energy E^* matches in this case a specific energy level and the interaction probability, i.e. the cross section, increases sharply.

In the following, several decay channels of the compound nucleus, i.e. reaction types, are discussed.

Radiative Capture

In a radiative capture reaction (n, γ) one or more gamma-ray photons are emitted from the compound nucleus. The nucleus attains eventually its ground-state. In that case, the emitted gamma-ray energy is the sum of the neutron kinetic energy and the binding energy of the neutron in the compound nucleus.

In general the radiative capture process is the dominating neutron absorption process for slow neutrons besides fission. Emission of charged particles (e.g. α , p) is quite rare at this energy. Due to the positive charge, the particles have to overcome the Coulomb electrostatic potential which means that an additional energy is needed to detach the particle from the nucleus; this happens only for a small number of low mass elements.

Fission

In a fission process (n, f) the compound nucleus breaks up into two parts of medium weighted nucleus - the fission products. Instantaneous gamma rays and usually two or three neutrons are emitted. The fission products decay subsequently and beta and gamma particles are emitted over a period of time. The easiest model to understand the

fission process is the liquid-drop model^[16]. The critical energy for fission depends on the charge and mass of the target nucleus^[17]. If the binding energy of a neutron is higher than the critical energy, the compound nucleus is likely to fission at any neutron energy. For ²³⁵U about 200 MeV of energy is released per fission. Over 80 % of this energy is kinetic energy of the fission products, while the rest is distributed as kinetic energy of the neutrons, instantaneous gamma ray emission and beta particle, neutrino and gamma ray emission from fission products.

Elastic and Inelastic Scattering

Contrary to the hard sphere scattering, in elastic scattering (n, n) via a compound nucleus formation the nucleus decays immediately by emitting a neutron. The target nucleus attains its initial ground state.

The inelastic scattering process is a combination of a scattering process and an (n, γ) process which is likely to happen at fast neutron energies. The compound nucleus decays by emitting a neutron of lower energy than the captured, incident neutron. The target nucleus is left in an excited stage. Inelastic scattering is not important in the energy range, which is of interest in this work.

1.1.2 Resonance Models

In this section, the basic principle of the commonly used resonance models is briefly discussed. These models describe the shape of the resonance cross sections which is an essential element in this work.

The incident neutron as well as the incident target nucleus and both emerging reaction products may be described quantum mechanically by ingoing and outgoing wave functions. The incident and emerging particles are denoted as the incident channels (c) and the exit channels (c'), respectively. The target is characterized by its spin quantum number I which can be zero or a multiple of $1/2$. The neutron spin on the other hand is always $1/2$. These two spins combine to the so-called channel spin $s = I + 1/2$. It is convenient to represent the relative motion of the neutron in angular moments of the ingoing wave with the momentum l which is zero or a positive integer. Resonances are classified according to the contributing partial wave. s-, p-, d-, f-resonances corresponds to moments of 0, 1, 2, 3, respectively.

Due to the short ranged nuclear forces the interaction configuration can be separated into an external region and an internal region (see figure 1.3). It is assumed that the nuclear forces in the external region are negligible. The wave functions of the free particles can therefore be derived analytically. The compound nucleus on the other hand is formed inside the internal region. Here the wave functions are unknown due to the complexity of the compound nucleus. However, it is possible to match the ingoing wave function of neutron and nucleus (incident channel) and the internal wave function of the compound nucleus at the boundary of the nuclear forces. For each ingoing wave one finds the transition probability to different outgoing waves (outgoing channel) and thus the partial cross section.

It is assumed that the transition time from external to internal region ($\approx 10^{-20}$ s) is significantly shorter than the lifetime of the compound nucleus ($\approx 10^{-14}$ s^[18]). Due to this relative long lifetime, the disintegration of the compound nucleus is essentially

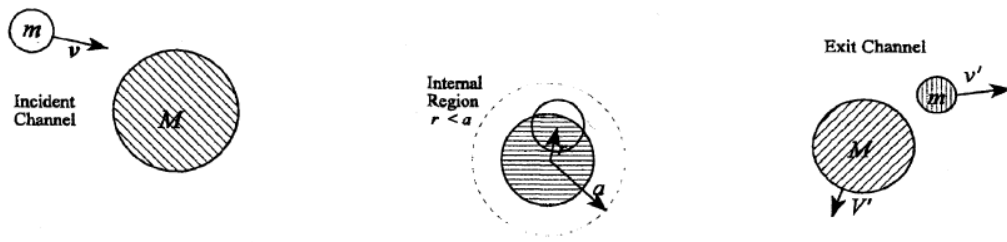


Figure 1.3: Schematic of entrance and exit channels as used in scattering theory^[20]

independent of the original mode of formation which means that the incident and outgoing channels are decoupled. Therefore secondary particles, e.g. scattered neutrons, are essentially emitted isotropically in the center of mass reference frame. For detailed information see Fröhner^[9] and Lane and Thomas^[19].

The transition probability from a specific incident channel (c) to an exit channel (c'), namely the partial cross section, can be written most generally by the R-matrix expression^[19] (equation 1.4) where the specific channels are characterized by the above mentioned quantum numbers. This formalism can be applied to various incident particles. However, in this work only incident neutrons interacting with a target nucleus are considered as incident channel. The partial cross section from incident channel c to exit channel c' is defined as^[8]:

$$\sigma_{cc'} = \pi \lambda_c^2 g_c |\delta_{cc'} - U_{cc'}| \quad (1.4)$$

where λ is the reduced de Broglie wavelength of the neutron. g is the so called statistical spin factor defined by $g = (2J+1)/2(2I+1)$ which describes the probability that a neutron with angular momentum l and the target spin add to the total spin quantum number J . $\delta_{cc'}$ is the Kronecker delta which is 1 for $c = c'$ and otherwise 0. $U_{cc'}$ is the so-called collision matrix or S matrix which is basically a probability matrix between the incident channels and the outgoing channels. This collision matrix can then be described by the well-known resonance descriptions^[8,21,9]:

- **Single-Level Breit-Wigner (SLBW):** The SLBW approximation is limited to the case of well separated resonances with no resonance-resonance interference. Furthermore, this approximation can produce nonphysically negative scattering cross sections in some cases.
- **Multi-Level Breit-Wigner (MLBW):** The MLBW approximation includes resonance-resonance interference effects in the elastic scattering and total cross sections. In contrast to the SLBW, cross sections are guaranteed to be positive. For light and medium-mass nuclei and for fissile actinides the MLBW approximation is often inadequate^[9].
- **Adler-Adler (AA):** The AA approximation is usually restricted to the s-wave resonances of the fissionable nuclei in the low energy region. Level-level and channel-channel interference effects are included in all cross sections via "effective" resonance parameters.
- **Reich-Moore:** The Reich-Moore formalism has become the dominant choice for resonance cross section representation. This formalism describes in detail nearly all

resonances in the peak, the interference dips and the multilevel interference region. Light, medium and heavy nuclei both fissile and non fissile can be equally well described.

The simplest model to describe the resonance shape is given by the SLBW formalism which is shortly presented in the following:

It is possible to reduce the general equation 1.4 to simple expressions for the capture, fission and scattering cross section by using a specific SLBW collision matrix^[9]. By introducing the maximum resonance cross section σ_0 at energy E_0 , one obtains the well known Breit-Wigner single-level formula. The neutron capture and fission resonance cross section can then be written as^[8]:

$$\sigma_{\gamma,f} = \sigma_0 \frac{\Gamma_{\gamma,f}}{\Gamma} \left(\frac{E_0}{E} \right)^{1/2} \frac{1}{1 + y^2} \quad (1.5)$$

with:

$$y = \frac{2}{\Gamma} (E - E_0) \quad (1.6)$$

Γ_γ and Γ_f are the partial width of the resonance of the radiative capture and the fission reaction. The $\frac{\Gamma_\gamma}{\Gamma}$ and $\frac{\Gamma_f}{\Gamma}$ fractions denote the probability that the compound nucleus decays via the γ or the fission channel, respectively. The maximum resonance cross section σ_0 is defined as:

$$\sigma_0 = 4\pi\lambda^2 \frac{\Gamma_n}{\Gamma} g = 2.608 \cdot 10^6 \frac{(A+1)^2}{A^2 E} \frac{\Gamma_n}{\Gamma} g \quad (1.7)$$

where the neutron energy E is given in eV.

The Breit-Wigner single-level formula for elastic scattering is composed of three terms: the resonance scattering, the interference scattering and the potential scattering. The interference of resonance and potential scattering causes a cross section dip on the lower energy side of the resonance. The SLBW scattering cross section can be written as:

$$\sigma_s = \underbrace{\sigma_0 \frac{\Gamma_{\gamma,f}}{\Gamma} \left(\frac{E_0}{E} \right)^{1/2} \frac{1}{1 + y^2}}_{\text{resonance scattering}} + \underbrace{\frac{\sigma_0 2R}{\lambda} \frac{y}{1 + y^2}}_{\text{interference scattering}} + \underbrace{4\pi R^2}_{\text{potential scattering}} \quad (1.8)$$

where $\frac{\Gamma_n}{\Gamma}$ is the probability of the elastic scattering channel. R is the radius of the target nucleus which is approximately $R \approx 1.25 \cdot 10^{-13} A^{1/3}$ cm. λ is the wavelength of the neutron.

A precise representation of the resonance cross section is crucial for reactor calculations and in particular for determining the neutron balance. In the slowing down process, neutrons are particularly absorbed by the resonances of the main fuel constituents, e.g ^{238}U .

1.2 Scattering Kernel

The Scattering Kernel $\sigma_s(E \rightarrow E', \vec{\Omega} \rightarrow \vec{\Omega}')$ is the derivative of the the scattering cross section $\sigma_s(E)$ with respect to energy and angular direction of scattered neutrons. It denotes the probability that a neutron with energy E , traveling in direction Ω is scattered to energy E' and in direction Ω' . The scattering kernel can be rewritten as:

$$\sigma_s(E \rightarrow E', \vec{\Omega} \rightarrow \vec{\Omega}') = \sigma_s(E) P(E \rightarrow E', \vec{\Omega} \rightarrow \vec{\Omega}') \quad (1.9)$$

where P represents the scattering probability. A commonly used simplification is to assume that the scattering depends only on the angle between the initial and secondary unit vectors Ω and Ω' : $\Omega \cdot \Omega' = \mu_0 = \cos \vartheta$. This approximation holds in general for non crystalline structures. It follows:

$$\sigma_s(E \rightarrow E', \vec{\Omega} \rightarrow \vec{\Omega}') = \sigma_s(E \rightarrow E', \mu_0) \quad (1.10)$$

The integration over the secondary energy and angular distribution of the scattering kernel leads evidently to the scattering cross section:

$$2\pi \int_0^\infty dE' \int_{-1}^1 d\mu_0 \sigma_s(E \rightarrow E', \mu_0) = \sigma_s(E) \quad (1.11)$$

1.2.1 Angular Expansion of the Scattering Kernel

For most deterministic transport methods it is customary to expand the double differential scattering cross section into orthogonal Legendre polynomials^[22]:

$$\sigma_s(E \rightarrow E', \vec{\Omega} \rightarrow \vec{\Omega}') = \sum_{n=0}^{\infty} \frac{2n+1}{4\pi} \sigma_{sn}(E \rightarrow E') P_n(\mu_0) \quad (1.12)$$

where $P_n(\mu_0)$ are the Legendre polynomials of the cosine of the scattering angle μ_0 in the laboratory reference frame. $\sigma_{sn}(E \rightarrow E')$ are the Legendre moments of the scattering kernel which can be found by:

$$\sigma_{sn}(E \rightarrow E') = \int_1^{-1} 2\pi P_n(\mu_0^{lab}) \sigma_s(E \rightarrow E', \vec{\Omega} \rightarrow \vec{\Omega}') d\mu_0^{lab} \quad (1.13)$$

Using the zeroth order Legendre polynomials, $P_0(x) = 1$, an integration over the scattering angle, i.e. the isotropic scattering kernel is obtained, which describes solely the energy transfer $\sigma_{s1}(E \rightarrow E') = \sigma_s(E \rightarrow E')$. Using the first order Legendre polynomial, $P_1(x) = x$, one obtains the first moment of the scattering kernel $\sigma_{s1}(E \rightarrow E')$. This moment is used to determine the mean cosine of the scattering angle:

$$\bar{\mu}_0^{lab}(E) = \frac{\int_0^\infty \sigma_{s1}(E \rightarrow E') dE'}{\sigma_s(E)} \quad (1.14)$$

which is commonly used in deterministic codes.

1.2.2 Energy Moments of the Scattering Kernel

In addition to the angular Legendre expansion, an expansion into energy moments $A_k(E)$ is of great help. These energy moments are then used as matrix elements of the scattering operator in deterministic transport methods^[23], which is obtained by multiplying the energy transfer with the corresponding neutron energy loss and by integrating over the secondary energy distribution:

$$A_k(E) = \int_0^\infty (E' - E)^k \sigma_{s0}(E \rightarrow E') dE' \quad (1.15)$$

These moments can be used to calculate the mean energy loss per collision at energy E :

$$\langle E - E' \rangle_{av} = -\frac{A_1(E)}{A_0(E)} \quad (1.16)$$

1.2.3 Asymptotic Scattering Kernel

The elastic scattering process can be treated by laws of classic mechanics of two-body kinetics with energy and momentum conservation. In the following the so-called asymptotic scattering kernel is derived which describes the secondary energy and angular distribution of scattered neutrons at zero Kelvin. Three assumptions are made:

- *Isotropic scattering*: An important, commonly used assumption is made that the neutron scattering is isotropic in the center of mass reference frame (COM) (see 1.1.2)
- *Hard spheres*: It is assumed that both, the neutron and the nucleus, behave like perfect elastic hard spheres (two body kinetics). Resonance effects are neglected.
- *Zero Kelvin temperature*: It is considered that the target is at rest in the laboratory reference frame (LAB) i.e. the target is at 0 K temperature. Consequently, the target can not transfer kinetic energy to the neutron.

In the laboratory frame, a neutron with mass unity moves with speed v towards the target with mass A (see Figure 1.4). In the COM frame the neutron moves with speed:

$$u = \frac{Av}{A+1} \quad (1.17)$$

and the nucleus with speed:

$$U = -\frac{v}{A+1} \quad (1.18)$$

The total momentum in the COM frame is zero:

$$A m U + m u = -A m \frac{v}{A+1} + m \frac{Av}{A+1} = 0 \quad (1.19)$$

The conservation of momentum and kinetic energy gives a relation to the secondary velocities of neutron u' and of the target U' in the COM system:

$$u' + AU' = 0 \quad (1.20)$$

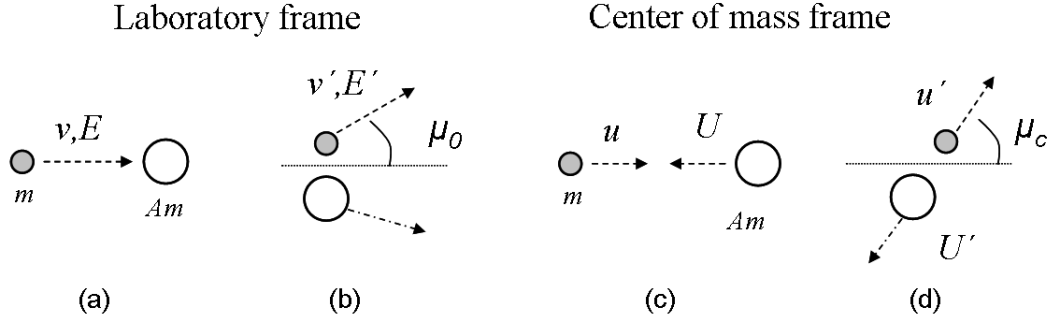


Figure 1.4: Trajectories of a neutron and a target nucleus before and after a scattering event in the laboratory reference frame (a,b) and in the center of mass reference frame (c,d), zero Kelvin approximation

$$\frac{1}{2}(u')^2 + \frac{1}{2}A(U')^2 = \frac{1}{2}(u)^2 + \frac{1}{2}A(U)^2 = \frac{1}{2}\left(\frac{Av}{A+1}\right)^2 + \frac{1}{2}A\left(\frac{v}{A+1}\right)^2 \quad (1.21)$$

which gives for the secondary velocities:

$$u' = \frac{Av}{A+1} \text{ and } U' = \frac{v}{A+1} \quad (1.22)$$

Consider μ_C and μ_0 the cosines of the scattering angles in the COM and LAB frame, respectively one has:

$$\frac{E'}{E} = \frac{1 + 2A\mu_C + A^2}{(1 + A)^2} \quad (1.23)$$

and

$$\mu_0 = \frac{1 + A\mu_C}{(1 + 2A\mu_C + A^2)^{1/2}} \quad (1.24)$$

where E and E' are the neutron energy before and after the scattering process, respectively. Both, the secondary energy E' and the scattering angle in LAB frame μ_0 depend on μ_c . Defining the ratio $\alpha = (A - 1)^2 / (A + 1)^2$ we obtain:

$$\frac{E'}{E} = \frac{1}{2}[(1 + \alpha) + (1 - \alpha)\mu_C] \quad (1.25)$$

The minimum energy transfer E'_{min}/E occurs if μ_C is unity. Then the neutron does not lose energy. The maximum energy transfer E'_{max}/E is given for $\mu_C = -1$. One obtains:

$$\frac{E'_{min}}{E} = 1 \text{ and } \frac{E'_{max}}{E} = \alpha \quad (1.26)$$

The mean energy loss $\langle E - E' \rangle_{av}$ is given by:

$$\langle E - E' \rangle_{av}(E) = \frac{1}{2}(1 - \alpha)E \quad (1.27)$$

and the mean cosine of the scattering angle $\bar{\mu}_0^{lab}$ is given by:

$$\bar{\mu}_0^{lab} = \frac{2}{3A} \quad (1.28)$$

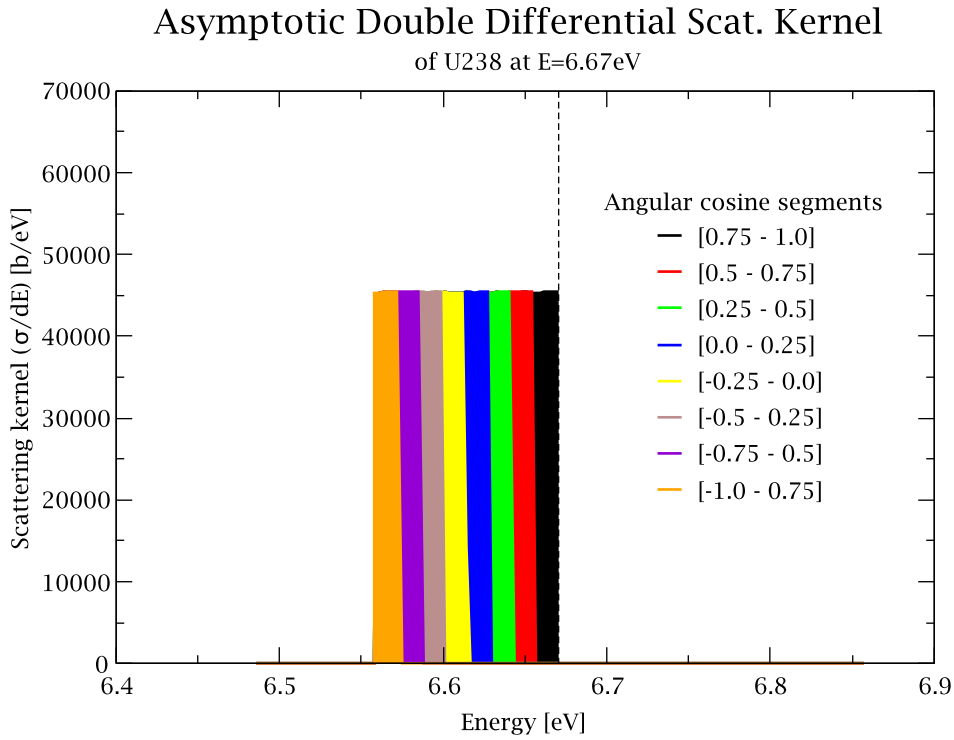


Figure 1.5: Asymptotic scattering kernel of ^{238}U at 6.67 eV

The energy transfer kernel can be rewritten as:

$$\sigma(E \rightarrow E') = \frac{\sigma(E)}{(1 - \alpha)E} \quad (1.29)$$

which is only non-zero in the interval: $E \geq E' \geq \alpha E$. The secondary neutrons are equally distributed between the incident neutron energy E and αE . The energy transfer depends strongly on the mass number of the collision partner of the neutron. For Hydrogen ($A = 1$ and $\alpha=0$) the neutron may lose its entire energy in a single collision. For heavy nuclei, the possible energy loss of a neutron in an elastic scattering is significantly smaller.

Figure 1.5 shows the asymptotic scattering kernel of ^{238}U for an incident neutron with energy 6.67 eV. The distribution of the scattering angle is illustrated by using angle segments. Each segment corresponds to a range of scattering angles (e.g. red corresponds to the range $-0.75 < \mu = \cos\vartheta < -0.5$ where ϑ is the scattering angle). In the case of the asymptotic kernel of ^{238}U at 6.67 eV, the minimum energy of a scattered neutron is $E_{min} = 6.67 \text{ eV} \cdot \left(\frac{237}{239}\right)^2 = 6.558 \text{ eV}$ while the mean energy loss is $\langle E - E' \rangle_{av} = 0.056 \text{ eV}$ and the mean cosine angle is $\bar{\mu}_0^{lab} = 0.0028$. The integral of this scattering kernel is normalized to the 0 K cross section at 6.67 eV energy.

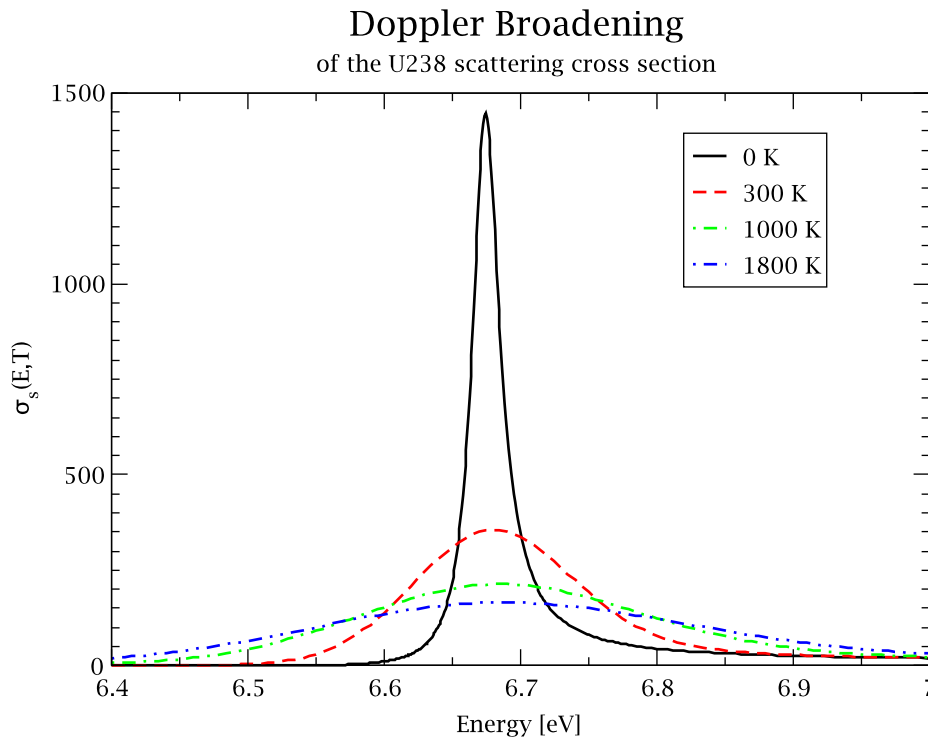


Figure 1.6: Doppler effect widening of the 6.67 eV resonance scattering cross section of ^{238}U

1.3 Doppler Broadening Theory

The temperature of the target has a significant impact on the shape of the resonance. As temperature increases, the width of the resonance tends to broaden while the peak cross section decreases (see figure 1.6). This behavior is known as *Doppler broadening*. The reason for this is that the target nuclei are thermally agitated at non-zero K temperature.

In order to take into account the movement of the targets, one has to distinguish between the laboratory (LAB) reference frame and the target-at-rest (TR) frame. The zero Kelvin cross section denotes only the interaction probability in the TR reference frame of a specific nucleus. On the other hand, the temperature dependent cross section of a bulk of thermally agitated nuclei in the LAB frame is calculated by averaging the zero Kelvin cross section over the target velocity distribution. The well known Doppler broadening equation is then given by:

$$\sigma_x(v, T) = \frac{1}{v} \int_{\text{all } V: v_r > 0} v_r \sigma_x(v_r, 0) M^T(V) dV \quad (1.30)$$

where $\sigma_x(v, T)$ is the Doppler broadened cross section of reaction x, $\sigma_x(v_r, 0)$ is the zero-Kelvin cross section and v_r is the relative speed of the neutron in the TR frame. $M^T(V)$ is the spectrum of the target velocities given by a velocity distribution $p(V)$. Commonly it is assumed that the target nuclei behave like atoms of a free gas. Their velocity distribution $p(V)$ for this free gas model (FGM) is then given by a Maxwell Boltzmann distribution:

$$M^T(V) = \frac{4}{\sqrt{\pi}} \beta^{3/2} V^2 e^{-\beta V^2} \quad (1.31)$$

with:

$$\beta = \frac{M}{2k_B T} \quad (1.32)$$

and where V is the speed and M is the mass of target. k_B is the Boltzmann constant.

In this section the analytic Doppler broadening methods are introduced for the cross sections, as well as for the scattering kernel which is the differential part of the scattering cross section.

1.3.1 Temperature Dependent Cross Sections

There are several methods used to Doppler broaden resonance cross sections in an analytic way. They can be divided into two different methodologies. One way of Doppler broadening is to address directly to the complex resonance shape functions $\psi + i\chi$ used for example in the Single-Level Breit-Wigner (SLBW) formalism. Using equation 1.5 and 1.30 the temperature dependent capture cross section becomes:

$$\sigma_\gamma(E, T) = \frac{\sigma_0 \Gamma_\gamma}{\Gamma} \left(\frac{E_0}{E} \right)^{1/2} \psi(\xi, q) \quad (1.33)$$

where E_0 is the resonance energy. Γ and Γ_γ are the total and capture resonance widths. The variables q and ξ are defined as:

$$q = \frac{2}{\Gamma} (E - E_0) \quad \text{and} \quad \xi = \frac{\Gamma}{(4E_0 k_B T / A)^{1/2}} \quad (1.34)$$

and the temperature dependent function ψ :

$$\psi(\xi, q) = \frac{\xi}{2\sqrt{\pi}} \int_{-\infty}^{\infty} e^{-(1/4)(q-p)^2 \xi^2} \frac{dp}{1+p^2} \quad (1.35)$$

In the same way the temperature dependent scattering cross section can be obtained for SLBW resonances:

$$\sigma_s(E, T) = \frac{\sigma_0 \Gamma_n}{\Gamma} \psi(\xi, q) + \frac{\sigma_0 R}{\lambda_0} \chi(\xi, q) + 4\pi R^2 \quad (1.36)$$

where Γ_n is the scattering resonance width. The additional temperature dependent function χ is defined as:

$$\chi(\xi, q) = \frac{\xi}{\sqrt{\pi}} \int_{-\infty}^{\infty} p e^{-(1/4)(q-p)^2 \xi^2} \frac{dp}{1+p^2} \quad (1.37)$$

This formalism has been extended by Fröhner^[9] to treat also multilevel resonance formalism (see section 1.1.2) using the so called Turing's Method.

However, a much more widely used method for Doppler broadening is based on tabulated point data of the zero Kelvin cross section. The so called SIGMA1 method was proposed by Cullen and Weisbin^[24] and later integrated in the Doppler broadening mod-

ule BROADR of the well known cross section processing code NJOY^[25]. For this method cross sections are stored on a specific energy grid such that it is possible to interpolate linearly between the points:

$$\begin{aligned}\sigma(E) &= \frac{E - E_k}{E_{k+1} - E_k} \sigma_{k+1} + \frac{E_{k+1} - E}{E_{k+1} - E_k} \sigma_k \quad (E_k \leq E \leq E_{k+1}) \\ &= A_k + B_k E\end{aligned}\quad (1.38)$$

with the interpolation constants A_k and B_k . σ_k is the cross section at energy E_k . A_k and B_k are the interpolation constants. This interpolation with energy can be introduced in terms of velocity:

$$\sigma(x) = a_k + b_k x^2 \quad (1.39)$$

with the interpolation constants a_k and b_k .

Substituting $y^2 = \beta V^2$ and $x^2 = \beta v_r^2$ in equation 1.30 and 1.31 and replacing σ by equation 1.39 leads to^[24]:

$$\begin{aligned}\sigma(v, T) &= \frac{1}{y^2} \left(\frac{1}{\pi}\right)^{1/2} \int_0^\infty x^2 \sigma(x) \left[e^{-(x-y)^2} - e^{-(x+y)^2} \right] dx \\ &= \frac{1}{y^2} \left(\frac{1}{\pi}\right)^{1/2} \sum_k \int_{x_k}^{x_{k+1}} x^2 (a_k + b_k x^2) \left[e^{-(x-y)^2} - e^{-(x+y)^2} \right] dx \\ &= \sigma^*(y, T) - \sigma^*(-y, T)\end{aligned}\quad (1.40)$$

By substituting $Z = x - y$ and collection in terms of powers of Z one obtains for $\sigma^*(y, T)$:

$$\begin{aligned}\sigma^*(y, T) &= \frac{1}{y^2} \left(\frac{1}{\pi}\right)^{1/2} \sum_k \int_{x_k}^{x_{k+1}} \left[b_k Z^4 + 4b_k y Z^3 + (a_k + 6b_k y^2) Z^2 \right. \\ &\quad \left. + (2a_k y + 4b_k y^3) Z + (a_k y^2 + b_k y^4) \right] e^{(-Z^2)} dZ\end{aligned}\quad (1.41)$$

The integral can be solved using the relation:

$$\frac{2}{\sqrt{\pi}} \int_{x_k}^{x_{k+1}} Z^n e^{-Z^2} dZ = F_n(x_k + 1) - F_n(x_k) \quad (1.42)$$

where $n = 0, 1, 2, 3, 4$ and where F_n is defined as:

$$\begin{aligned}F^0(x) &= \text{ERF}(x) \\ F^1(x) &= (1/\pi)^{1/2} + (1 - e^{-x^2}) \\ F^2(x) &= 1/2 \text{ERF}(x) - a/\sqrt{\pi} e^{-x^2} \\ F^3(x) &= (1/\pi)^{1/2} \left[1 - (1 + x^2)e^{-x^2} \right] \\ F^4(x) &= 3/4 \text{ERF}(x) - (1/\pi)^{1/2} \left(\frac{3x}{\pi} + x^3 \right) e^{-x^2}\end{aligned}\quad (1.43)$$

With the set of equations 1.40 to 1.43 a complete method is given to Doppler broaden any energy dependent cross section .

1.3.2 Temperature Dependent Scattering Kernel

Since the scattering kernel is the double differential part of the scattering cross section, it evidently depends on temperature as well. As shown before, the asymptotic scattering kernel neglects the velocity distribution of the targets and thus its temperature dependence (see section 1.2.3). Consequently, any energy transfer from the target nucleus to the scattered neutron is not possible. For low energies and resonant cross sections the asymptotic kernel is evidently unjustified as was shown in the previous section. Therefore, parallel to equation 1.30 the temperature dependent scattering kernel should be derived by solving the following equation:

$$\sigma_s^T(E \rightarrow E', \vec{\Omega} \rightarrow \vec{\Omega}') = \frac{1}{v} \int_{\text{all } V: v_r > 0} v_r \sigma_s(v_r, 0) P(v, V \rightarrow E', \vec{\Omega}') M^T(V) dV \quad (1.44)$$

where $\sigma_s^T(E \rightarrow E', \vec{\Omega} \rightarrow \vec{\Omega}')$ is the scattering kernel from neutron energy E to E' and from direction $\vec{\Omega}$ to $\vec{\Omega}'$. v and v_r denote the neutron speed in the laboratory and in the target-at-rest reference frame, respectively. V is the target speed. M^T is the spectrum of V , namely the Maxwell Boltzmann distribution in case of a free gas model. $P(v, V \rightarrow E', \vec{\Omega}')$ is the probability density of v and V , which leads to the specific values of E' and $\vec{\Omega}'$ after scattering. $\sigma_s(v_r, 0)$ is the zero Kelvin scattering cross section.

In 1944, Wigner and Wilkins^[26] developed the first temperature dependent scattering kernel by solving equation 1.44 for moderator materials without internal structures, i.e. without cross section resonances. Their isotropic kernel introduced the possibility of an energy transfer from a target nucleus to a neutron. For constant cross section σ_s equation 1.44 becomes:

$$\sigma_s^T(E \rightarrow E', \vec{\Omega} \rightarrow \vec{\Omega}') = \frac{\sigma_s}{v} \int_{\text{all } V: v_r > 0} v_r P(v, V \rightarrow E', \vec{\Omega}') M^T(V) dV \quad (1.45)$$

This leads to the zeroth moment of the scattering kernel of the solution of Wigner and Wilkins:

$$\begin{aligned} \sigma_{s0}^T(E \rightarrow E') &= \frac{\sigma_s A}{8E} e^{-\frac{E'-E}{2k_B T}} (G_1 + G_2) \\ G_1 &= e^{+\frac{v_{max}^2 - v_{min}^2}{2}} [ERF(\Theta v_{max} - \zeta v_{min}) - ERF(\Theta v_{max} + \zeta v_{min})] \\ G_2 &= e^{-\frac{v_{max}^2 - v_{min}^2}{2}} [ERF(\Theta v_{max} - \zeta v_{min}) + ERF(\Theta v_{max} + \zeta v_{min})] \end{aligned} \quad (1.46)$$

with $\Theta = (A + 1)/(2\sqrt{A})$ and $\zeta = (A - 1)/(2\sqrt{A})$. v_{max} and v_{min} are the larger and smaller value of the incident neutron speed v and secondary neutron speed v' .

In 1967 Blackshaw and Murray^[27] introduced a new form of the scattering probability function in the velocity space, i.e. the isotropic velocity scattering kernel for energy dependent scattering cross sections as well as the angular moments of this kernel.

Ouisloumen and Sanchez^[1] integrated in 1991 (and shortly later Kurchenkov and Laletin^[28]) an energy dependent cross section into their evaluation of the effective, temperature dependent moments of the scattering kernel. They focused on an energy transfer change in the vicinity of ²³⁸U scattering resonances compared to the asymptotic kernel. They showed that neutrons predominantly gain energy in a collision at some energies in the vicinity of resonances.

In 1998, Rothenstein and Dagan^[2] extended the work of Ouisloumen and Sanchez^[1] to the double differential, resonance dependent scattering kernel. This kernel described for the first time the full secondary energy and angular distribution of neutrons scattered with a nucleus at a resonance energy. They showed that the integration of their full double differential kernel cover all angles gives exactly the isotropic solution of Ouisloumen and Sanchez. The full double differential kernel for energy dependent cross sections is given in the following as obtained by Rothenstein and Dagan^[2]:

$$\begin{aligned}
\sigma_s^T(E \rightarrow E', \vec{\Omega} \rightarrow \vec{\Omega}') &= \frac{1}{2\pi} \sigma_s^T(E \rightarrow E', \mu_0^{lab}) \\
&= \frac{1}{2\pi} \sqrt{\frac{A+1}{A\pi}} \frac{\exp(E/k_B T)}{E} \int_0^\infty dt [t \sigma_s^{tab}(E_r, 0)] e^{-t^2/A} \\
&\quad \left[H(t_+ - t) H(t - t_-) \int_{\epsilon_{max}-t}^{t+\epsilon_{min}} dx e^{-x^2} + H(t - t_+) \int_{t-\epsilon_{min}}^{t+\epsilon_{min}} dx e^{-x^2} \right] \\
&\quad \frac{P(u, \hat{\mu}_0^{CM})}{2\pi} \frac{4\epsilon_{max}\epsilon_{min}x^2}{B_0 \sin \hat{\varphi}} 2H(\cos \hat{\varphi} + 1) H(1 - \cos \hat{\varphi})
\end{aligned} \tag{1.47}$$

where $\sigma^{tab}(E_r)$ is the tabulated value of the so called bound cross section σ_b at zero Kelvin which is denoted by: $\sigma_b(E_r) = [(A+1)/A]^2 \sigma(E_r)$. H is the Heaviside function. The speed variables t , x and ϵ describe neutron and center of mass velocities and are given by $t = u\sqrt{A+1}$, $x = c\sqrt{A+1}$, $\epsilon = v\sqrt{A+1}$ and $\epsilon' = v'\sqrt{A+1}$. ϵ_{max} and ϵ_{min} are the larger and the smaller value of ϵ and ϵ' . t_\pm is given by $t_\pm = (\epsilon_{max} + \epsilon_{min})/2$. $\hat{\mu}_0^{lab}$ and $\hat{\mu}_0^{CM}$ are the polar scattering angles in the laboratory and in the center of mass reference frame, respectively. $P(u, \hat{\mu}_0^{CM})$ is the scattering probability density function in the center of mass reference frame.

In equation 1.47 the polar scattering angel $\hat{\mu}_0^{CM}$ is related to the angle φ by:

$$\hat{\mu}_0^{CM} = \frac{A_0 + B_0 \cos \hat{\varphi}}{4t^2 x^2} \tag{1.48}$$

with:

$$A_0 = [\epsilon^2 - x^2 - t^2] [\epsilon'^2 - x^2 - t^2] \tag{1.49}$$

$$B_0 = \sqrt{[(t+x)^2 - \epsilon^2] [(t+x)^2 - \epsilon'^2] [\epsilon^2 - (t-x)^2] [\epsilon'^2 - (t-x)^2]} \tag{1.50}$$

The expansion of equation 1.47 into Legendre moments is done by multiplying the double differential kernel with $2\pi P_n(\mu_0^{lab})$, where P_n is the n^{th} Legendre polynomial, and by integrating over the polar scattering cosine μ_0^{lab} (see 1.2.1). The n th moment of the resonance dependent scattering kernel is defined as:

$$\begin{aligned}
\sigma_{sn}^T(E \rightarrow E') &= \sqrt{\frac{A+1}{A\pi}} \frac{\exp(E/k_B T)}{E} \int_0^\infty dt t \sigma_s^{tab}(E_r) \exp(-t^2/A) \\
&\quad \left[H(t_+ - t) H(t - t_-) \int_{\epsilon_{max}-t}^{t+\epsilon_{min}} dx e^{x^2} + H(t - t_+) \int_{t-\epsilon_{min}}^{t+\epsilon_{min}} dx e^{x^2} \right] \\
&\quad \int_0^{2\pi} d\varphi \frac{P(u, \hat{\mu}_0^{CM})}{2\pi} P_n(\hat{\mu}_0^{lab})
\end{aligned} \tag{1.51}$$

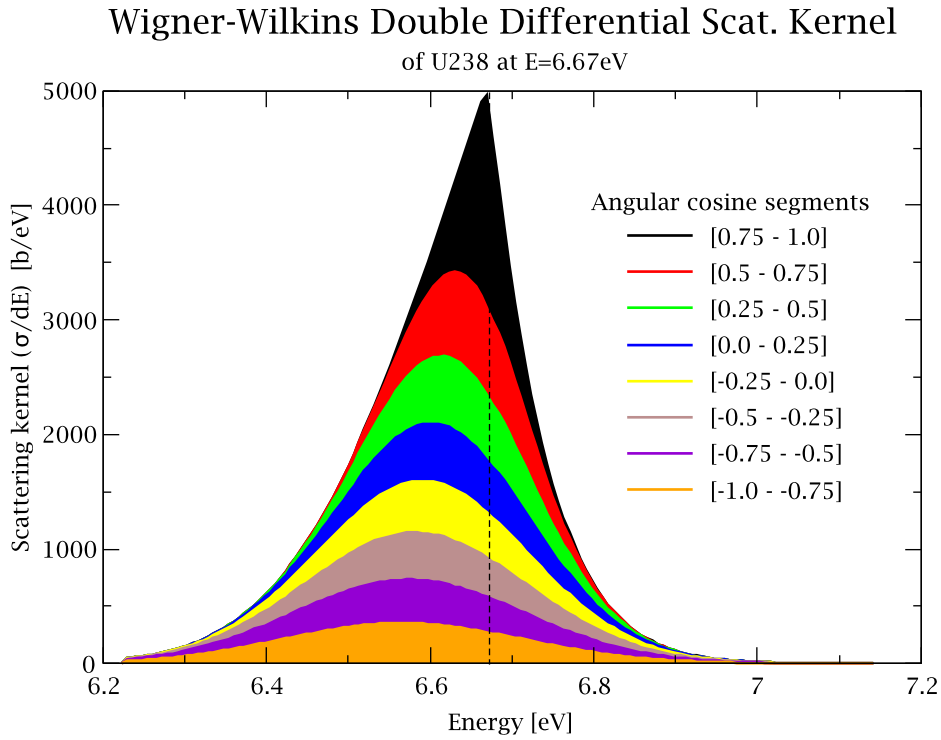


Figure 1.7: Wigner-Wilkins scattering kernel of ^{238}U at 6.67 eV and 1200 K

which is similar to the Legendre moments obtained by Ouisloumen and Sanchez^[1].

The energy transfer kernel, i.e. the 0th moment of the scattering kernel, can be rewritten as:

$$\sigma_{s0}^T(E \rightarrow E') = \sqrt{\frac{A+1}{A\pi}} \frac{\exp(E/k_B T)}{E} \int_0^\infty dt t \sigma_s^{tab}(E_r) \exp(-t^2/A) \left[H(t_+ - t) H(t - t_-) \int_{\epsilon_{max}-t}^{t+\epsilon_{min}} dx e^{x^2} + H(t - t_+) \int_{t-\epsilon_{min}}^{t+\epsilon_{min}} dx e^{x^2} \right] P(u, \hat{\mu}_0^{CM}) \quad (1.52)$$

Figures 1.7 and 1.8 show the Wigner-Wilkins (based on equation 1.45) and resonance dependent (based on equation 1.47) scattering kernel for ^{238}U at 6.67 eV and 1200 K, respectively. A similar representation is used as is done for the asymptotic scattering kernel of figure 1.5 in section 1.2.3. In contrast to the asymptotic kernel, the integral of the temperature dependent scattering kernels is equal to the Doppler broadened scattering cross section. Besides the normalization, the temperature dependent scattering kernel differs significantly from the asymptotic kernel. The neutron scatters to a much broader energy range. In particular, an energy gain by the neutron is possible. In addition, in case of the asymptotic kernel, the energy of the neutron is directly related to the scattering angle. In case of the temperature dependent kernel, the energy distribution of a specific scattering angle expands significantly.

The differences of the Wigner Wilkins and the resonance dependent scattering kernel are discussed in detail in section 3.3.

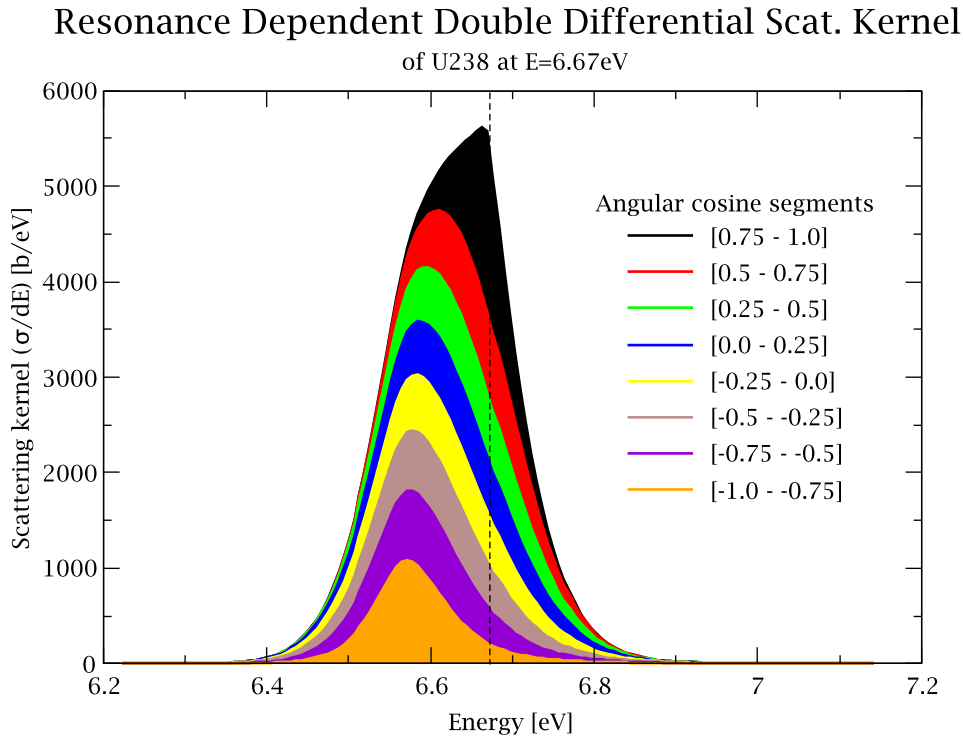


Figure 1.8: Resonance dependent scattering kernel of ^{238}U at 6.67 eV and 1200 K

1.4 The Scattering Kernel in the Transport Equation

In today's reference neutronic codes either the asymptotic scattering kernel is used or the Wigner-Wilkins approximation; yet not the resonance dependent scattering kernel. This causes an important inconsistency in the very basic treatment of the neutron transport equation. The transport equation for the neutron vector flux f at location r , in direction $\vec{\Omega}$ and at energy E is:

$$\frac{1}{v} \frac{\partial f(E, r, \vec{\Omega}, t)}{\partial t} + \vec{\Omega} \cdot \nabla f(E, r, \vec{\Omega}, t) + [\Sigma_s(E) + \Sigma_a(E)] f(E, r, \vec{\Omega}, t) = \int_{\vec{\Omega}'} \int_0^\infty \Sigma(E' \rightarrow E, \vec{\Omega}' \rightarrow \vec{\Omega}) f(E', r, \vec{\Omega}', t) d\vec{\Omega}' dE' + S(E, r, \vec{\Omega}, t) \quad (1.53)$$

where $\Sigma_s(E)$, $\Sigma_a(E)$ and $\Sigma(E' \rightarrow E, \vec{\Omega}' \rightarrow \vec{\Omega})$ are the macroscopic scattering cross section, the absorption cross sections and the macroscopic scattering kernel, respectively.

The use of the scattering kernel approximations leads to the following contradiction: on the left side of the equation the scattering cross section depends evidently on energy and temperature. On the right side, however, the double differential part of the scattering cross section, namely the scattering kernel, excludes the energy and temperature dependence.

In the documentation of the THERMR module of NJOY^[25] this inconsistency in the

transport equation is directly addressed:

*"Strictly speaking, the scattering law for free-gas scattering given in Eq. (10) [$S(\alpha, \beta)$ equation] is only applicable to scatterers with no internal structure. However, many materials of interest in reactor physics have strong scattering resonances in the thermal range (for example, ^{240}Pu and ^{135}Xe). The Doppler broadened elastic cross section produced by BROADR is formally correct for a gas of resonant scatterers, but the cross section resulting from Eq. (10) [$S(\alpha, \beta)$ equation] is not. In order to allow for resonance scattering in a way that at least provides the correct total cross section, THERMR renormalizes the free-atom scattering to the broadened elastic cross section. **The secondary energy distribution will still be incorrect.**"*

Several groups studied the impact of the analytic resonance dependent scattering kernel compared to the asymptotic kernel. Ouisloumen and Sanchez^[1] compared both energy transfer kernels in view of their energy dependence, up- and down-scattering probabilities (see also 3.3.2) and average neutron energy after collision. Kurchenkov and Laletin^[28] performed similar comparisons. Bouland, Kolesov and Rowlands^[29] investigated the impact of the resonance dependent scattering kernel on the ^{238}U resonance absorption rate and the Doppler reactivity effect of a LWR pin cell compared to the asymptotic kernel. An increased absorption and Doppler effect of 1% and 9 % respectively was found. Dagan and Rothenstein^[30] integrated the isotropic resonant kernel into the fineflux OZMA code and confirmed results of Bouland et al.^[29]. Similar results were obtained by Kurchenkov and Sidorenko^[31] who investigated the impact on a VVER pin cell.

Dagan and Rothenstein^[2] and Rothenstein^[5] compared the resonance dependent scattering kernel to the Wigner-Wilkins kernel with special emphasis on the secondary angular distribution and showed the strong anisotropy in the laboratory frame of reference in the vicinity of a pronounced resonance. Dagan^[4] showed the impact of the resonant scattering kernel on the benchmark of Tellier et. al.^[32] using the Monte Carlo code MCNP with $S(\alpha, \beta)$ scattering tables for the resonance range of ^{238}U in a similar manner as it is done for light nuclei. An increased Doppler effect of up to 17.5 % and an increased ^{238}U resonance absorption of up to 2.1 % was found. Dagan and Broeders^[33] extended this investigation to LWR burn-up benchmarks and concluded an increased breeding of ^{239}Pu .

Recently, Lee et al.^[34] investigated the influence of the resonant kernel on an increase of the LWR Doppler-coefficient (10 %) and on a criticality decrease for LWR (0.20 %) and Next Generation Nuclear Plant (NGNP) (0.45 %), using a modified code version of CASMO-5. Oberle^[35] implemented the resonance dependent scattering kernel in the fineflux solver ULFISP for group cross section generation and studied the impact on full PWR core.

A detailed description of the analytic derivation of the resonance dependent scattering kernel and its application is given by Dagan^[36]. The impact of using the resonance dependent scattering kernel on HTR reactor calculations is studied in detail in chapter 5.

2 A New Developed Stochastic Doppler Broadening Method

In this chapter, the basic Doppler broadening equation 1.30 is solved by means of a new developed Monte Carlo code called *DOPPLER-MC*. For the first time, it is possible to perform stochastically the Doppler broadening of cross sections and in particular to determine stochastically the temperature and resonance dependent scattering kernel. Angular moments as well as energy moments of the resonant scattering kernel are calculated. In addition, this new code can be used to Doppler broaden scattering kernels employing the Wigner-Wilkins approximation.

In the following, the code *DOPPLER-MC* is introduced and its convergence is discussed.

2.1 The Code *DOPPLER-MC*

A stochastic code named *DOPPLER-MC* was developed which simulates directly an interaction of an incident neutron with a target nuclide. The code evaluates the effective temperature dependent cross section of various reactions (such as total, scattering or absorption cross section) as well as the secondary energy and angular distribution of neutron and target in case of a scattering event. With these distributions the code reconstructs the double differential scattering kernel.

DOPPLER-MC is based on a common method to sample the motion of the target nuclide in addition to the movement of the neutron. In the manual of Monte Carlo code MCNP^[37] this method is referred to as "*sampling the velocity of the target nucleus*" (SVT). In the following the theoretical model of the developed code *DOPPLER-MC* is presented:

- In a first step, the code samples the velocity, i.e. the energy, of a specific target nucleus (V , E_T), according to a probability density function based on the Maxwellian distribution for a given temperature (equation 1.31). The direction of the target nucleus with respect to the incident neutron is sampled with an isotropic distribution in the laboratory frame of reference. μ_T denotes the cosine of the angle between neutron and target directions.
- Then, the incident neutron kinetic parameters are transferred into the target-at-rest system (TR) by subtracting the target velocity V from the neutron velocity v . The relative velocity v_r of the neutron is obtained. In this reference frame, the zero Kelvin cross section $\sigma_x(v_r, 0)$ depicts the reaction probability of the specific sampled nucleus and the neutron. In case of a scattering event, the secondary parameters of the neutron, the energy after the collision E' and the cosine of the scattering angle μ_0^{TR} in the TR frame, are evaluated with equations 1.23 and 1.24.

- Finally, a weight (w_i) is associated to the sampled pair of neutron and target, which can be directly derived from the very basic equation (1.30) of the effective cross-section:

$$w_i = \frac{v_r}{v} \sigma_x(v_r, 0) \quad (2.1)$$

This weight denotes the probability that a neutron would react with the specific modeled target. The sum of the weights of different iterations is collected. In case of a scattering event the secondary neutron velocity and scattering angle are transferred back into the LAB system. The weight w_i of each iteration is accumulated in a specific energy-angle segment ($\Delta E', \Delta \mu_0$) of the outgoing neutron energy E' and the scattering angle μ_0 .

This sampling procedure is repeated N times. By accumulating all repetitive histories of those weighted probabilities at each energy point of the zero K cross section, one gets the Doppler broadened cross section:

$$\sigma(E, T) = \frac{1}{N} \sum_{i=1}^N w_i \quad (2.2)$$

In addition, the double differential part of the effective cross section, namely the scattering kernel, can be evaluated by considering only a specific energy-angle segment $\Delta E', \Delta \mu_0$:

$$\frac{\partial \sigma(E, T)}{\partial E \partial \Omega} = \frac{1}{N} \sum_{i=1} w_i \text{ if } E' \text{ and } \mu_0 \text{ in } (\Delta E', \Delta \mu_0) \quad (2.3)$$

In case of the use of the Wigner-Wilkins approximation the cross section σ_x in equation 2.1 is set to be “one” for all energies. At the end of the run the obtained scattering kernel has to be renormalized to the Doppler broadened cross section.

Figure 2.1 shows a scheme of the *DOPPLER-MC* program. Due to the stochastic nature of the *DOPPLER-MC* code, the results obtained for the Doppler broadened cross section and the kernel are always associated with a specific uncertainty. With increasing the number of simulated collisions, the uncertainty however decreases and the result converges to the theoretical value. A reliable convergence is reached when the associated uncertainty is less than the experimental uncertainty of the measured cross sections.

As an example, the total and scattering cross section of ^{238}U resonance peak at 36.67 eV and at 1200 K are stochastically Doppler broadened using the *DOPPLER-MC* code. The convergence of the code is studied at this energy and temperature. For this, the number of iteration is steadily increased until the stochastic results converge (figure 2.2). After about $2 * 10^4$ iterations the stochastic solution converges.

2.2 Comparison of the Analytic and Stochastic Doppler Broadening Methods

In this section, the stochastic Doppler broadening method is compared to the analytic SIGMA1 method. In a first part, the developed code *DOPPLER-MC* and the NJOY code are used to broaden several integral cross sections. A set of characteristic cross sections is chosen for comparing different aspects of the Doppler broadening, namely

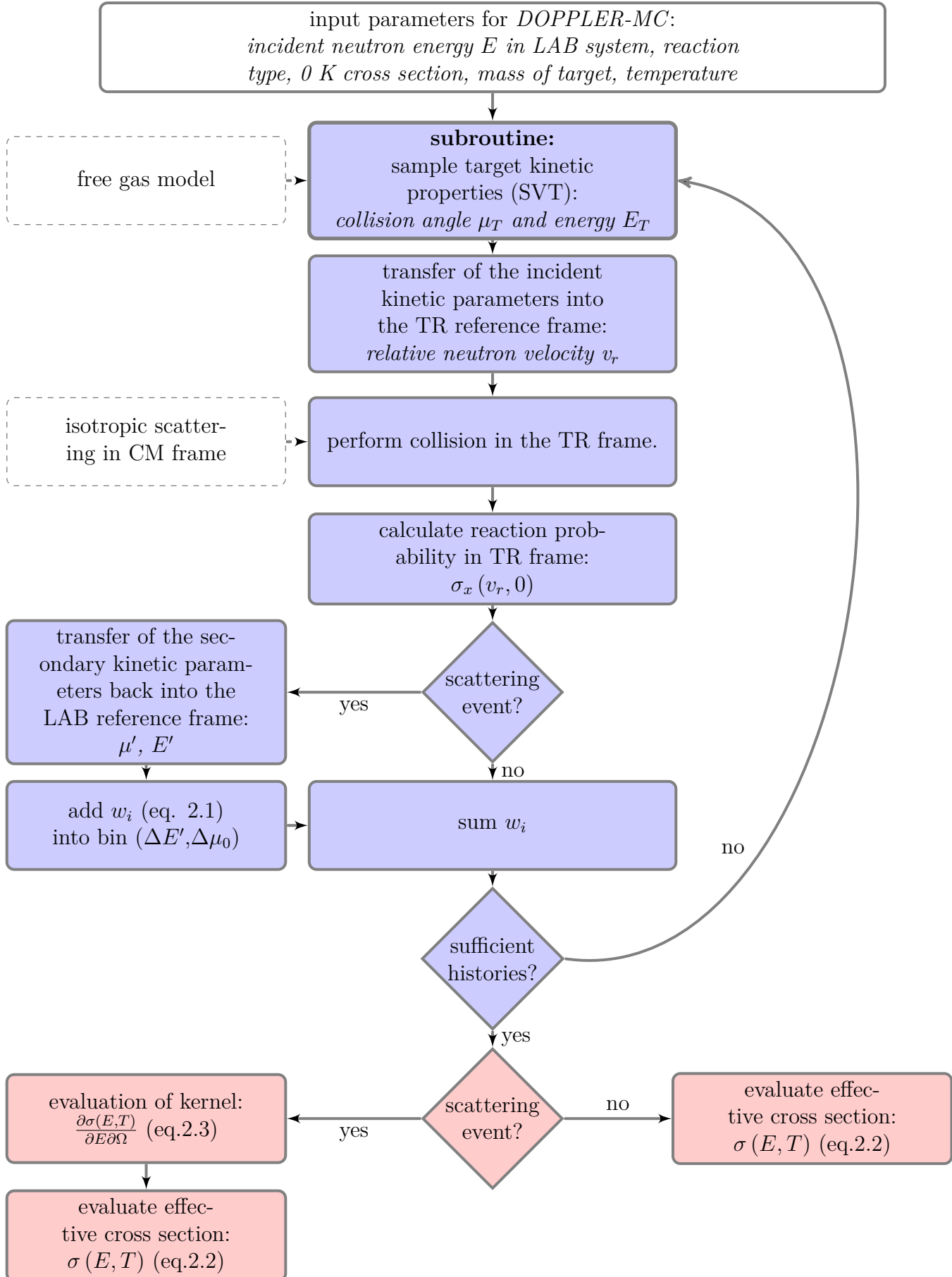


Figure 2.1: Scheme of the *DOPPLER-MC* program (blue boxes denote steps inside the history iteration, red boxes denote analysis steps and dashed boxes denote model assumptions)

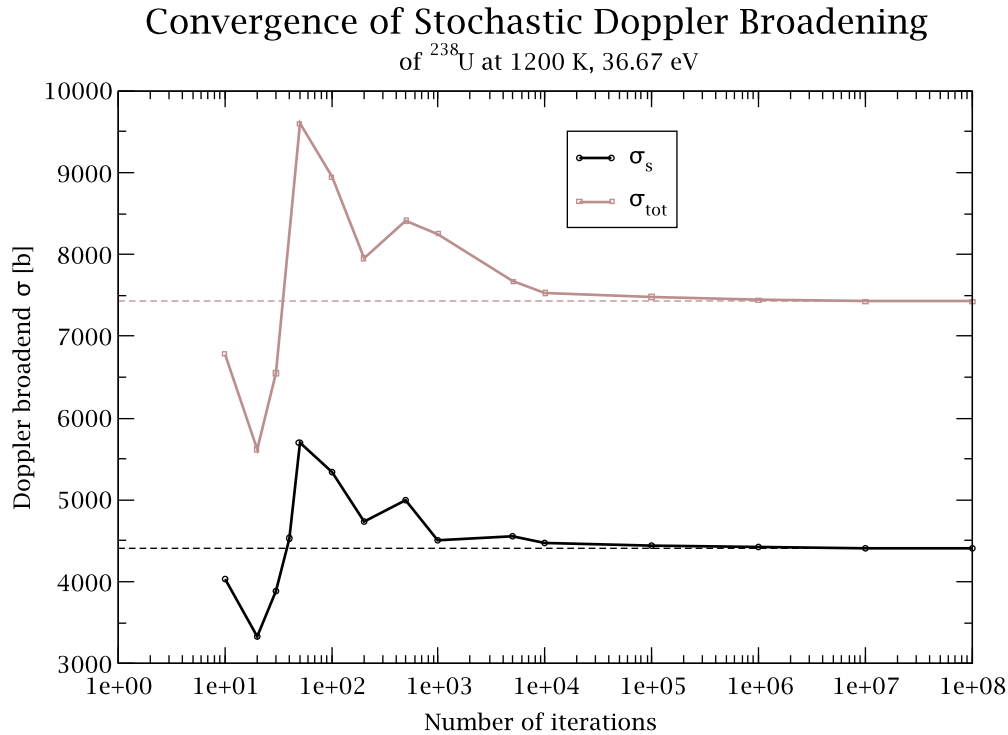


Figure 2.2: Convergence of the stochastic Doppler broadening algorithm for the scattering and total cross section of ^{238}U at 1200 K and 36.67 eV

resonance broadening, Doppler broadening of a constant cross section and broadening of a $1/v$ -shape cross section.

In a second part, the *DOPPLER-MC* code is used to Doppler broaden stochastically scattering kernels. These are then compared to analytically broadened kernels based on equation 1.47. The JEFF 3.1 nuclear data cross sections library^[13] is used with linear interpolation.

Cross Section Comparison

The Doppler broadening of resonance cross sections leads to a decrease of the resonance peak while the width broadens. Both, the stochastic *DOPPLER-MC* code and the NJOY code are used to Doppler broaden the scattering and total cross section of ^{238}U at 1200 K and 600 K, respectively. The energy scale ranges from 32 to 40 eV. It covers the 3rd main S resonance of ^{238}U at 36.6 eV. Both methods give exactly the same Doppler broadened cross sections (see figure 2.3).

In the low energy region, cross sections develop the so-called $1/v$ tail due to the Doppler broadening. This originates from the $1/v$ term in the basic Doppler broadening equation (1.30). The 0 K scattering cross section of ^{232}Th for example is constant in the energy range from 0.0001 eV to 0.01 eV. Figure 2.4 shows the $1/v$ tail of the ^{232}Th scattering cross sections at 300 K and 3000 K temperature in comparison to the constant zero K cross section. *DOPPLER-MC* and NJOY give the same Doppler broadened cross sections.

A property of the basic Doppler broadening equation is that a zero Kelvin cross sec-

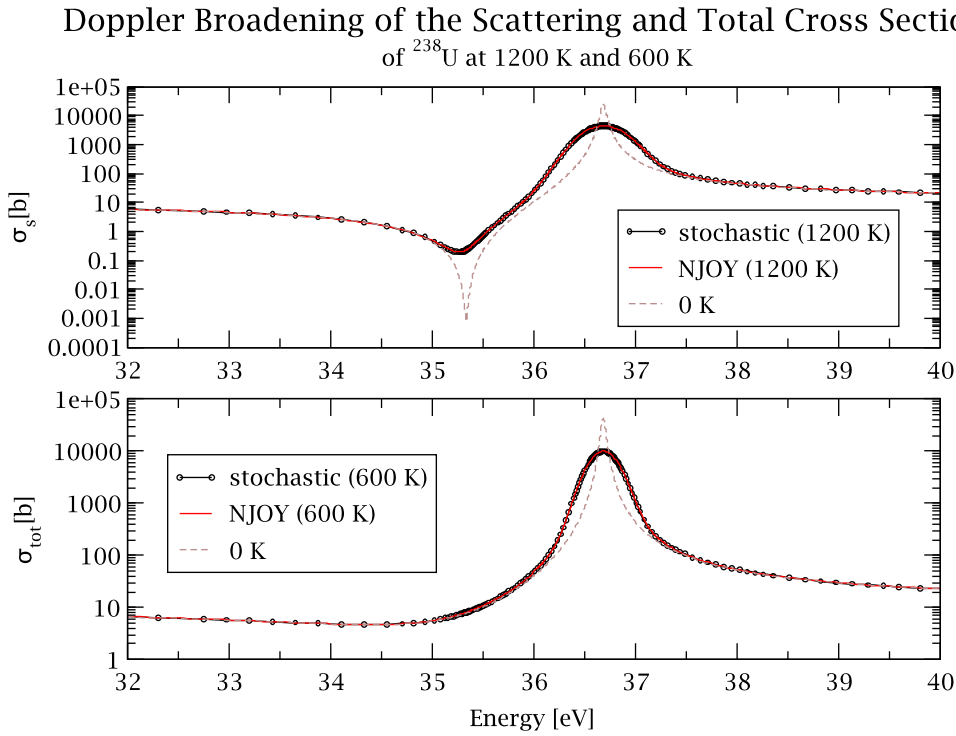


Figure 2.3: Stochastic and analytic Doppler broadening of scattering σ_s and total σ_{tot} cross section of ^{238}U at 1200 K and 600 K

tion with a $1/v$ shape remains unchanged under Doppler broadening. The integration in equation 1.30 is reduced to an integration over the Maxwell Boltzmann probability distribution $p(V)$ which leads evidently to the value 1. The (n,α) cross section of ^{10}B for example exhibits a $1/v$ shape in the low energy range. The *DOPPLER-MC* code is used to Doppler broaden stochastically this cross section for 300 K and 3000K. As can be seen in figure 2.5 the anticipated behavior is clearly obtained.

All representative cases studied show that the stochastic procedure of Doppler broadening gives exactly the same Doppler broadened cross section when compared to the analytical SIGMA1^[24] based solution (equation 1.40) using in NJOY.

Comparison of Scattering Kernels

The *DOPPLER-MC* is used to calculate the ^{238}U scattering kernel at 6.53 eV and at 1200 K temperature. This energy corresponds to the lower interference dip of the 6.67 eV main S resonance. This stochastic kernel is compared to the scattering kernel produced by analytical means^[30] based on equation 1.47 (figure 2.6). The contour of the kernel represents the energy distribution of the scattered neutrons. Eight segments represent the angular distribution of scattered neutrons. Unlike the kernel figures of the previous chapter, here the segments are represented for comparison reasons only by separating lines instead of colored areas. The stochastic and analytic kernel are in good agreement. However, the stochastic kernels exhibit small numerical instabilities for the forward scattering segment (0.75 - 1.0).

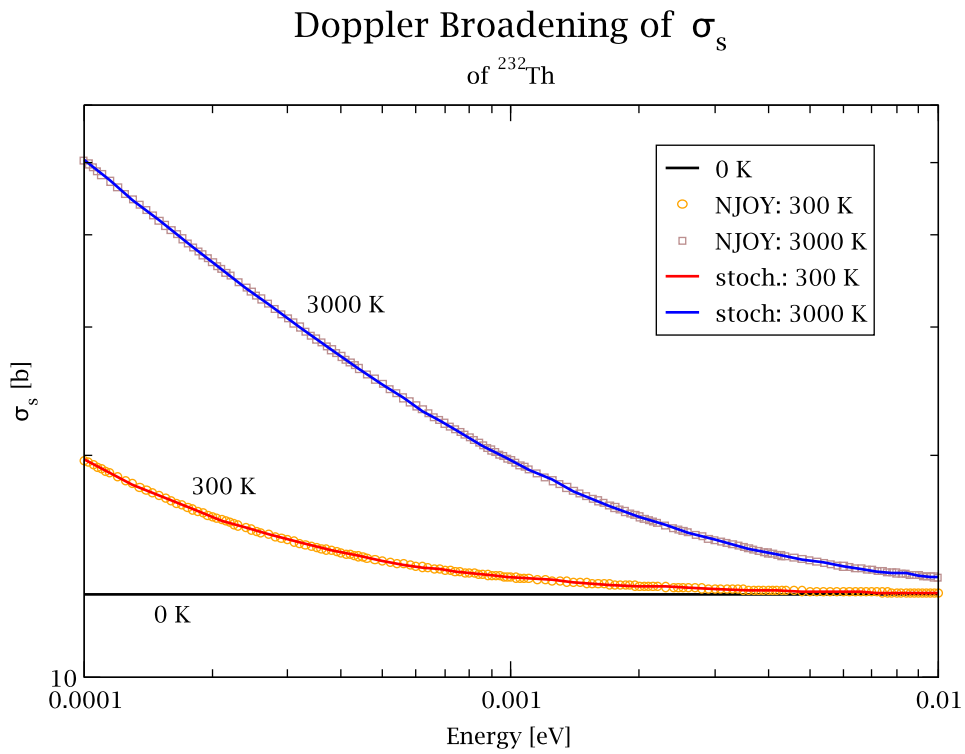


Figure 2.4: Stochastic and analytic Doppler broadening of the scattering cross section of ^{232}Th in the energy region from 0.0001 eV to 0.01 eV at 300 K and 3000 K

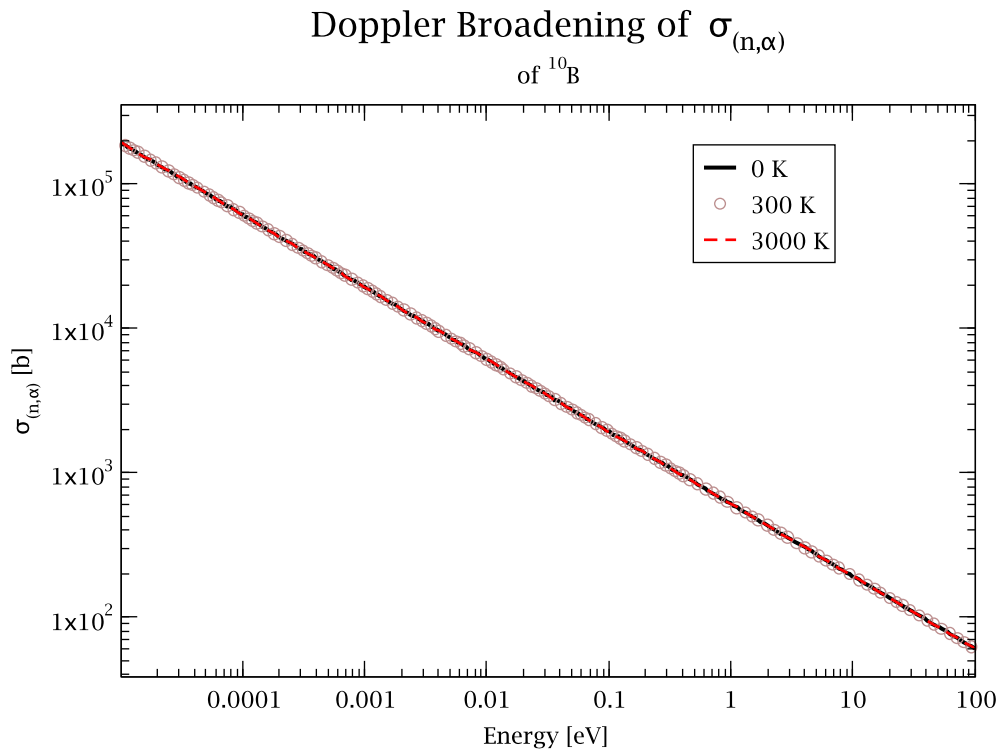


Figure 2.5: Stochastic Doppler broadening of the (n,α) cross section of ^{10}B at different temperatures

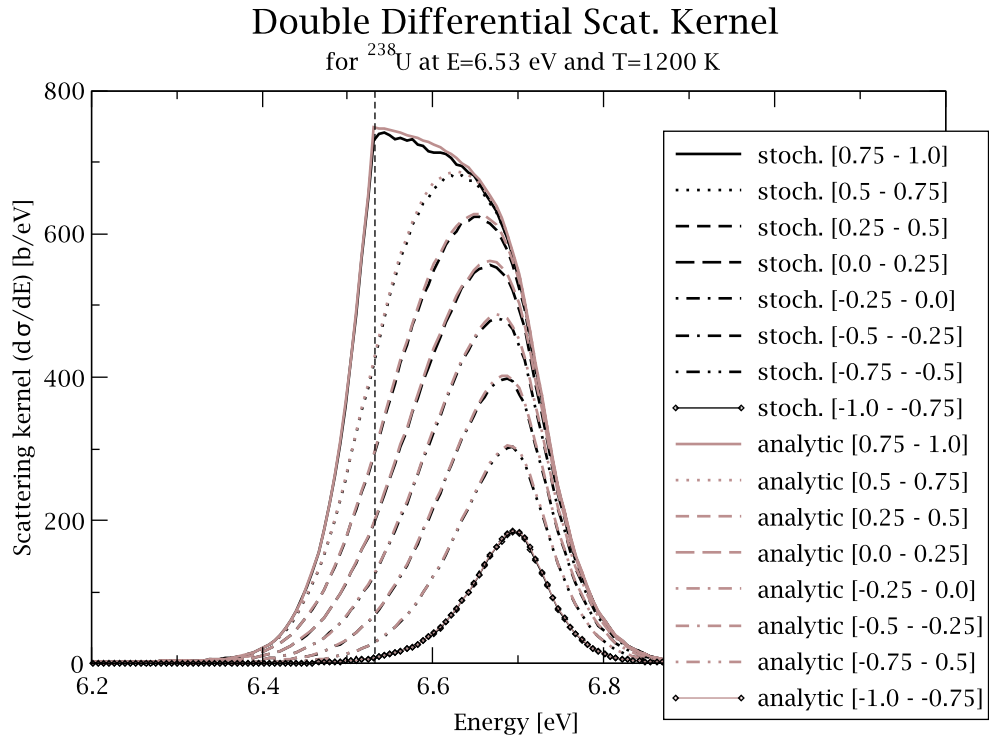


Figure 2.6: Stochastic and analytic resonance dependent scattering kernel of ^{238}U at 6.53 eV and 1200 K

In addition, the *DOPPLER-MC* and analytic kernel of ^{232}Th at the interference range (23.2 eV) of 2nd main S resonances at 1200 K are compared (figure 2.7). Again the stochastic and analytic kernel agree completely for both, the energy and angular distribution.

It should be noted that the stochastic method for Doppler broadening necessitate a significant higher computer time compared to the SIGMA1^[24] approach. In addition, the obtained values for the cross sections are subject to statistical uncertainties. However, Fröhner pointed out^[9] that even the SIGMA1 approach of Cullen and Weisbin is not exact since the linear interpolation between tabulated cross sections introduces some error. Milgram et. al.^[38] proposed to use the method of antithetic variance reduction to accelerate the convergence of the stochastic Doppler broadening method. A speedup by a factor 2 is reached with a simple choice of a two-part antithetic transform referred to as weighted stratification in^[39].

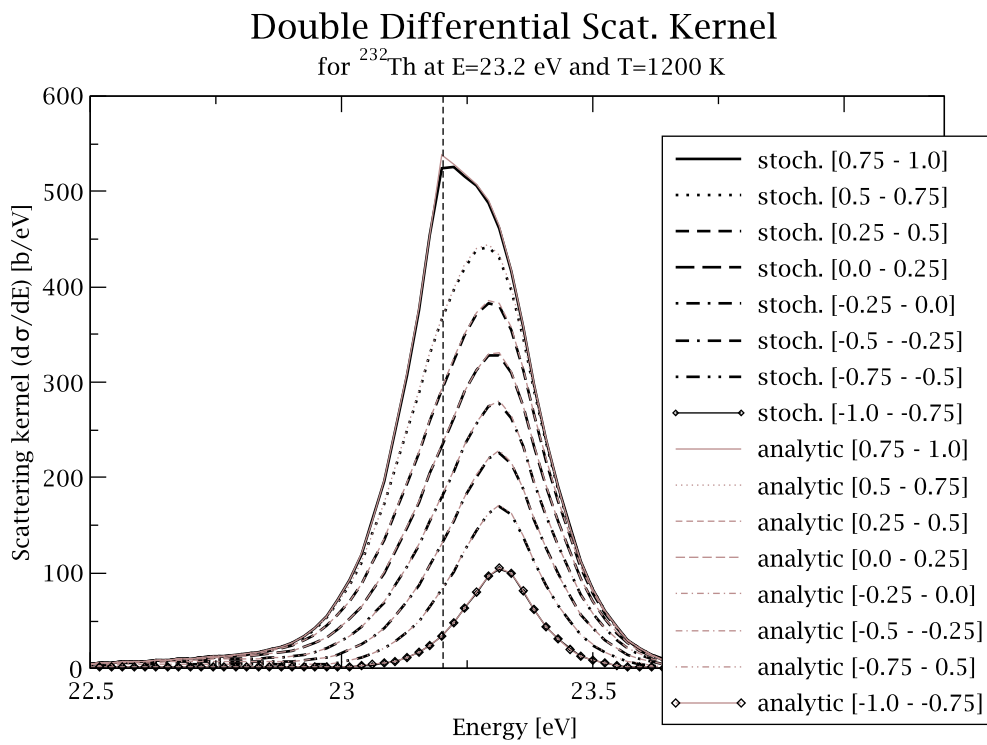


Figure 2.7: Stochastic and analytic resonance dependent scattering kernel of ^{232}Th at 23.2 eV and 1200 K

3 The DBRC Method for the Resonance Dependent Scattering Kernel in Monte Carlo Codes

Monte Carlo (MC) codes are widely used for radiation transport problems and in particular for nuclear reactor physics calculations such as the MCNP codes (MCNP4^[40], MCNP5^[37], MCNPX^[41]), MONK^[42] or PSG2/Serpent^[43].

In Monte Carlo transport codes, the transport problem is stochastically solved by accumulating so-called histories of particles. A high precision regarding geometry can be obtained. The movement of neutrons is directly simulated by probabilities of interaction processes. The neutron undergoes several interactions with matter like elastic or inelastic scattering until it is finally absorbed e.g. in an (n, γ) or a fission reaction. The neutron contributes to specific tallied parameter (like criticality level, flux and reaction rates) in its lifetime. Millions of particle histories are sampled in order to achieve a high confidence of the tallied parameters. Monte Carlo codes are widely accepted as a reference method. They should therefore use as few approximations as possible.

In the following, the commonly used approximative method of MC codes concerning the free gas scattering kernel for heavy nuclei is discussed. This method is called the “Sampling of the Velocity of the Target nucleus” (SVT). In order to introduce the correct, energy and temperature dependent, double differential scattering kernel this SVT method is modified and the so-called “Doppler Broadening Rejection Correction” (DBRC) is consequently developed. This correction is solely based on stochastic considerations. The resulting impact of DBRC correction on the secondary parameters of scattered neutrons is discussed in detail. In the last section of this chapter an alternative method to introduce the resonance dependent scattering into Monte Carlo Codes is presented. This “S(α, β)-probability-table-method” is based on the analytic formula (equation 1.47) and was developed by Rothenstein^[5].

3.1 The Sampling of the Velocity of the Target Nucleus Method

The method currently used in Monte Carlo codes to determine the energy and angle of a scattered neutron is based on the “Sampling of the Velocity of the Target nucleus” (SVT) approach mentioned in section 2.1. The underlying idea of this method is that a single target is sampled with a specific velocity V and direction Ω_T . This target is subsequently used as a collision partner for a neutron. The exact target probability density function,

based on the Doppler broadening equation 1.30, is:

$$P(V, \mu_t) = \frac{\sigma_s(v_r, 0) v_r p(V)}{2\sigma_s(E, T)v} \quad (3.1)$$

where V is the target velocity and μ_t is the cosine of the angle between incident neutron and target. $p(V)$ is the target velocity distribution. A Maxwell Boltzmann distribution is assumed. However MCNP e.g. further assumes that^[37]:

"the variation of $\sigma_s(v_r, 0)$ with target velocity can be ignored. The justification for this approximation is that (1) for light nuclei, $\sigma_s(v_r, 0)$ is slowly varying with velocity, and (2) for heavy nuclei, where $\sigma_s(v_r, 0)$ can vary rapidly, the moderating effect of scattering is small so that the consequences of the approximation will be negligible."

The probability density function becomes then:

$$P(V, \mu_t) \approx \sqrt{v^2 + V^2 - 2Vv\mu_t} V^2 e^{-\beta^2 V^2} \quad (3.2)$$

This can be written as:

$$P(V, \mu_t) \approx \left\{ \frac{\sqrt{v^2 + V^2 - 2Vv\mu_t}}{v + V} \right\} [V^3 e^{-\beta^2 V^2} + vV^2 e^{-\beta^2 V^2}] \quad (3.3)$$

which is used in MCNP to sample the target velocity. MCNP uses for the first part of the equation 3.3 a rejection function $R(V, \mu_t)$ ^[44]:

$$R(V, \mu_t) = \frac{\sqrt{v^2 + V^2 - 2Vv\mu_t}}{v + V} = \frac{v_r}{v + V} \leq 1 \quad (3.4)$$

This part represents the ratio of the relative velocity to the laboratory velocity of the neutron. The second part of equation 3.3 is sampled directly.

MCNP uses the SVT procedure if the energy of the neutron is less than $400 k_B T$ (10.034 eV at 300 K and 41.363 eV at 1200 K) or if the target is ^1H . It should be noted that the scattering kernel method as described above is rather based on equation 1.45 than on equation 1.30 because the cross section is assumed to be constant. Therefore MCNP uses not a resonance dependent scattering kernel but the Wigner-Wilkins approximation described analytically by equation 1.46.

If the neutron energy is higher than $400 k_B T$ and the target is not ^1H , the scattering kernel is not Doppler broadened at all. In this case, the asymptotic kernel is used. This means that MCNP effectively neglects the energy and temperature dependence of cross sections with regard to the scattering kernel.

3.2 The new DBRC Method

In 1996, a stochastic method was proposed by Rothenstein^[3] to account for the energy dependent cross section in a scattering process. This method, namely the *Doppler Broadening Rejection Correction (DBRC)* method, consists of a modification of the probability density function which MCNP uses to simulate the target velocity V and the angle be-

tween neutron and target μ_t . Equation 3.1 can be changed to:

$$\begin{aligned} P(V, \mu_t) &= C \left\{ \frac{\sigma_s(v_r, 0)}{\sigma_s^{max}(v_\xi, 0)} \right\} \left\{ \frac{v_r}{v+V} \right\} \{(v'+V)p(V)\} \\ &= C \left\{ \frac{\sigma_s(E_r, 0)}{\sigma_s^{max}(E_\xi, 0)} \right\} \left\{ \frac{v_r}{v+V} \right\} \{(v'+V)p(V)\} \end{aligned} \quad (3.5)$$

with the normalization constant C :

$$C = \frac{\sigma_s^{max}(E_\xi, 0)}{2v\sigma_s(E, T)} \quad (3.6)$$

where $\sigma_s^{max}(E_\xi, T)$ is the largest scattering cross section in a specific energy interval in the vicinity of the actual scattering cross section $\sigma_s(E, T)$. This energy interval corresponds to the dimensionless interval which is used in the Doppler broadening algorithm SIGMA1 by Weisbin and Cullen^[24]. In this interval, the argument of the integration in equation 1.40 has a non-negligible contribution to the integral. Typically an interval of $\xi \pm 4.0$ is chosen where ξ is the dimensionless speed of the neutron $\xi = \sqrt{AE/k_B T}$. C is a normalization constant. It neither depends on the target velocity V nor on the relative neutron velocity v_r , but only on the neutron velocity in the laboratory frame and the scattering cross section. Note that the basic Doppler broadening equation 1.30 is an integration over the target velocity.

Equation 3.5 can be written as:

$$\begin{aligned} P(V, \mu_t) &= C' \left\{ \frac{\sigma_s(E_r, 0)}{\sigma_s^{max}(E_\xi, 0)} \right\} \\ &\quad \left\{ \frac{v_r}{v+V} \right\} \\ &\quad \left\{ \frac{2\beta^4 V^3 e^{-\beta^2 V^2} + (\beta v \sqrt{\pi}/2)(4\beta^3/\sqrt{\pi})V^2 e^{-\beta^2 V^2}}{1 + \beta v \sqrt{\pi}/2} \right\} \end{aligned} \quad (3.7)$$

with

$$C' = \frac{\sigma_s^{max}(E_\xi, 0)(1 + \beta v \sqrt{\pi}/2)}{2v\sigma_s(E, T)\beta\sqrt{\pi}/2} \quad (3.8)$$

The two last brackets of equation 3.7 are sampled in the MCNP code (see equation 3.3). The last line corresponds to the Maxwell-Boltzman distribution multiplied by the factor $(V+v)$. MCNP samples according to the distributions $2\beta^4 V^2 e^{-\beta^2 V^2}$ and $(4\beta^3 \sqrt{\pi})V^3 e^{-\beta^2 V^2}$ which are associated by weights ‘‘one’’ and $(\beta v \sqrt{\pi}/2)$, respectively, with respect to the sum of the weights. Then a rejection method $R_1(V, \mu_t)$ is used (see equation 3.4) as a constraint on the choices of V and μ_t which corresponds to the second bracket of equation 3.7. The first curly bracket of equation 3.7 is an additional constraint on the choice of V and μ_t . This is exactly the term which MCNP neglects. Since this ratio of cross sections can not exceed unity, a second rejection method is applied:

$$R_2(V, \mu_t) = \frac{\sigma_s(E_r, 0)}{\sigma_s^{max}(E_\xi, 0)} \leq 1 \quad (3.9)$$

The DBRC method is in principle similar to the stochastic determination of the res-

onant scattering kernel with *DOPPLER-MC*. The *DOPPLER-MC* weighting procedure can be replaced by a rejection method similar to R_2 .

With the corrected probability density function (equation 3.7), MCNP is able to include the effect of the energy dependence of the cross sections on the scattering kernel. However, in his publication^[3] Rothenstein stresses the fact that the ratio of cross sections can lead to an extensive number of rejections in the vicinity of resonances, especially at the interference dip on the lower energy side of a resonance. In addition, he saw a problem of fundamental nature in the method of "sampling the velocity of the target nucleus". It represents the sampling of an additional variable, namely the velocity of the target nucleus, during the neutron history. The explicit dependence of the sampled value of V might introduce a bias in the calculation. Rothenstein points out that the scattering of the neutron should be not only be based on a singled sampled target but on the entire double differential scattering kernel, which includes all possible target velocities. For these reasons, Rothenstein abandoned the idea of a direct solution within MCNP and focused on the development of the analytic double differential scattering kernel and its introduction into NJOY (see section 3.4).

For this work the probability density function of MCNPX was changed according to the above presented method. The new modified MCNPX version now performs the following additional steps:

- When a neutron undergoes a scattering process with a nucleus in COLLIDN.F and its energy is below a certain threshold (typically 210 eV), the code checks if the zero Kelvin cross section of the nucleus is present in the data storage. If so, the DBRC flag is set for an extended simulation of the target velocity. The best way to load the natural cross section into the memory of the code is to use a flux tally (f4) in any cell with a flux multiplier of the zero Kelvin scattering cross section of the investigated nucleus.
- Within the subroutine TGTVEL.F the code searches the largest zero Kelvin scattering cross section $\sigma_s^{max}(E_\xi, T)$ in the above mentioned finite interval $\xi \pm 4.0$ if the DBRC flag is set.
- The code simulates the target in its standard way. The relative neutron energy in the TR frame is calculated. The additional rejection method is performed: if a random number is larger than the ratio $\sigma_s(E_r, 0) / \sigma_s^{max}(E_\xi, T)$ the code starts a new simulation of the target. If the random number is smaller than the cross section ratio the target is accepted and MCNPX continues in its usual way.

In the following, the differences between the DBRC corrected MCNP version and the standard MCNP version are discussed. A validation of the new DBRC model is given in chapter 4.

3.3 Comparison of the new DBRC and the Standard MCNP Scattering Model

In this section, a detailed comparison of the standard MCNP scattering kernel, namely the Wigner-Wilkins approximation, and the resonance dependent DBRC scattering kernel is made in order to highlight the introduced changes in terms of the scattering physics by

using the exact kernel. The energy transfer kernel, up- and down-scattering probabilities, energy moments and angular moments of the resonance dependent kernel and of the Wigner-Wilkins kernel of ^{238}U are discussed.

The new *DOPPLER-MC* code can easily be used to create the standard MCNP scattering kernel based on the constant cross section kernel (equation 1.45). To do this the weight associated to a sampling of a neutron collision with a specific target (equation 2.1) has to be set to one.

3.3.1 Energy Transfer Kernel

The energy transfer is described by the zeroth moment of the scattering kernel which is the contour of the kernel. Energy transfer kernels based on standard MCNP and on DBRC are compared. Different nuclei at various temperatures and energies are considered. Figures 3.1 and 3.2 show the scattering kernel of ^{238}U at the peak of the 6.67 eV resonance and at its lower energy interference range at 6.53 eV. Three different temperatures are considered: 100 K, 1000 K and 5000 K. The highest temperature is to some extent unrealistic for reactor applications, but illustrates the general dependence of the kernels with temperature. In the interference range the scattering cross section exhibits a dip due to the potential and the resonance scattering interference (see section 1.1.2). The area of the energy transfer kernel is equal to the integral cross section. Therefore, the area of the kernel at the resonance peak decrease with increasing temperature (figure 3.2) while the area of the kernel at the resonance dip increases as a consequence of a positive temperature gradient. The difference between the standard MCNP and the resonance

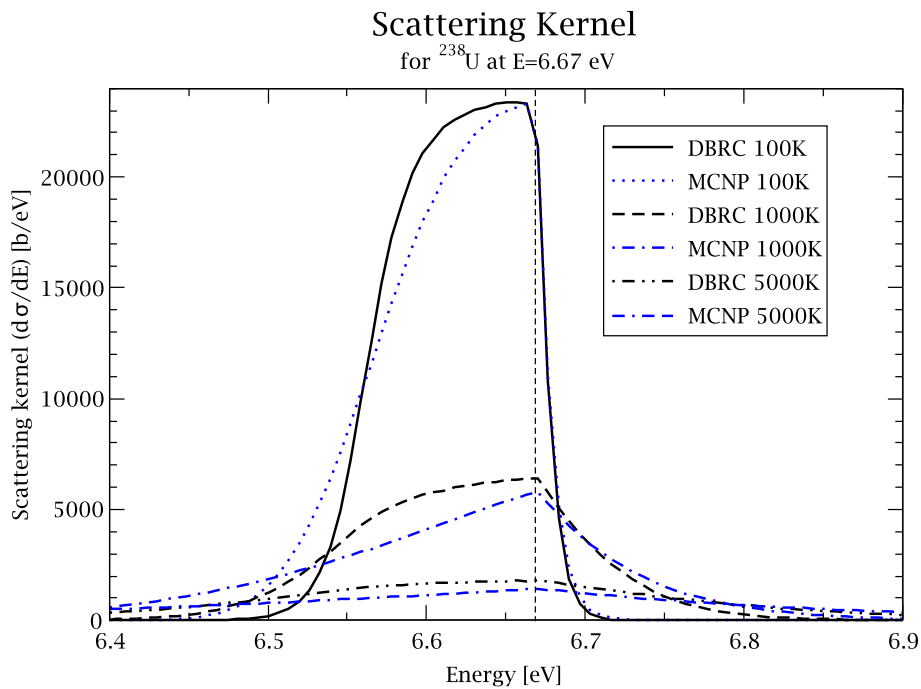


Figure 3.1: Stochastic resonance dependent kernel (DBRC) and constant cross section kernel (std. MCNP) of ^{238}U at 6.67 eV and for various temperatures

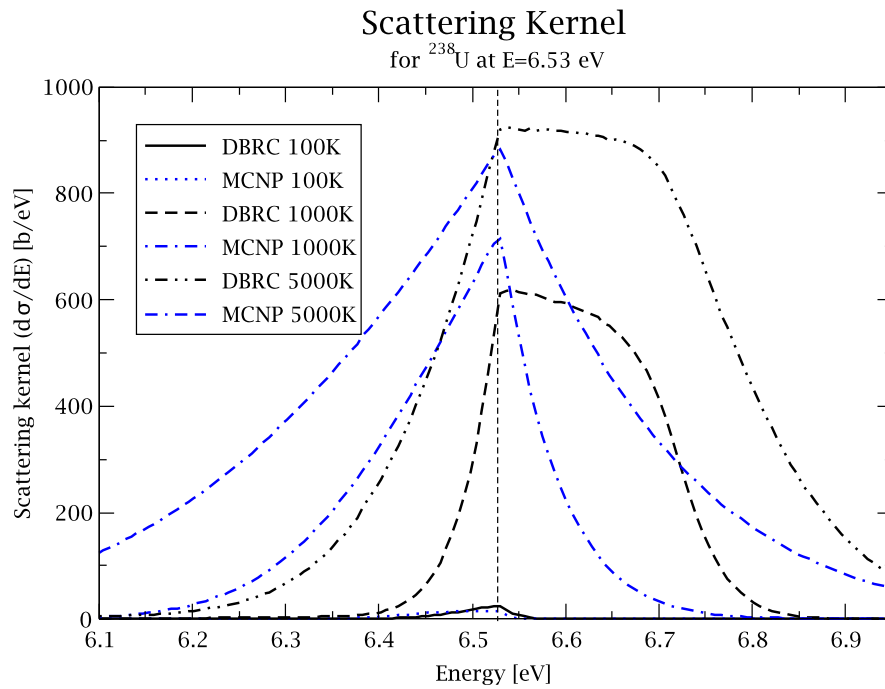


Figure 3.2: Stochastic resonance dependent kernel (DBRC) and constant cross section kernel (std. MCNP) of ^{238}U at 6.53 eV and for various temperatures

dependent scattering kernel is clearly shown in both figures. Neutrons tend to gain energy in a scattering event at the energy of the resonance dip taking into account the influence of the cross section (figure 3.2). At the resonance energy itself neutrons mainly lose energy, however with the improved model the energy range to which neutrons are scattered is smaller.

3.3.2 Up- and Down-Scattering Probabilities

A practical way to compare the standard MCNP and the DBRC kernel is to measure the fraction of up and down scattered neutrons, i.e. the fraction of neutrons which have a higher and lower energy after a scattering with a nucleus. Figure 3.3 shows these fractions for ^{238}U at a temperature of 1200 K in the energy range of 5 to 42 eV applying the DBRC and standard MCNP kernel as well as the zero Kelvin scattering cross section. The up- and down-scattering probabilities are similar for both approaches in the energy range between the resonances where the scattering cross section is relatively constant. However, in the vicinity of the resonances significant differences are pronounced. On the lower energy side of the resonance the up-scattering is enhanced while on the higher energy range the down-scattering is amplified for the resonance dependent model. On the lower energy side of the 6.67 eV ^{238}U resonance for example the up-scattering probability increases from about 30 % in case of the standard MCNP kernel to about 85 % in case of the DBRC kernel. On the higher energy side the up-scattering decreases to about 10 % while the down scattering increases consequently from 80 % to 90% when the DBRC is considered. This trend means that more neutrons are scattered towards the resonance

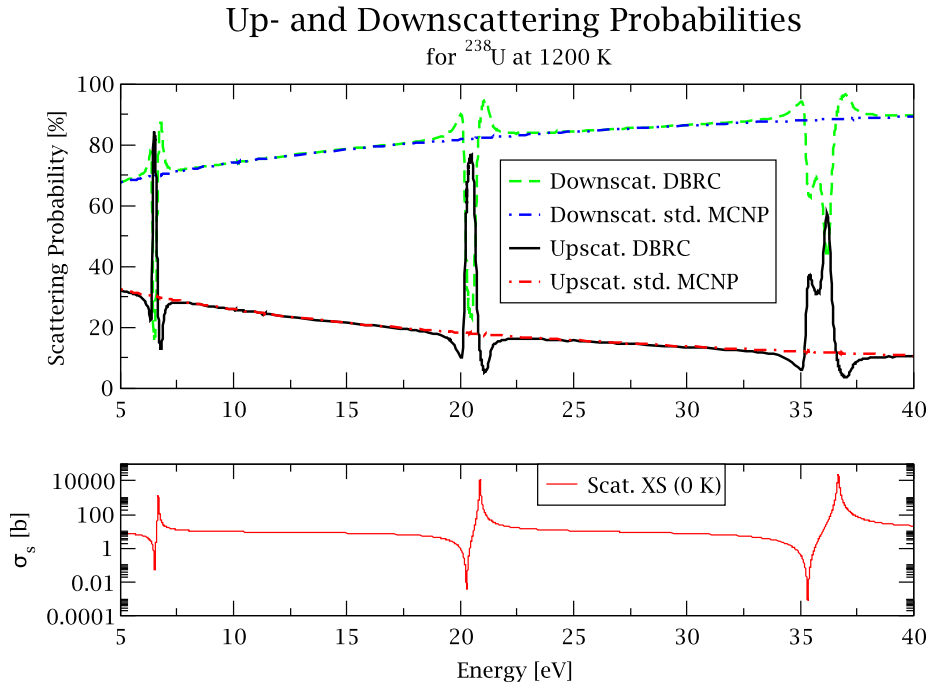


Figure 3.3: Up- and down-scattering probabilities (std. MCNP and DBRC) and scattering cross section of ^{238}U at 1200 K

energy. Therefore the probability of a subsequent resonance absorption increases.

3.3.3 Energy Moments of the Scattering Kernel

The scattering kernel is expanded into energy moments (see section 1.2.2 and Williams^[23]) and the mean neutron energy loss per collision with ^{238}U is calculated at 1000 K temperature in the vicinity of the 6.67 eV resonance (see figure 3.4). The standard MCNP and DBRC scattering models are considered. The zeroth energy moment $A_0(E)$ is an integration of the energy transfer kernel and therefore gives the Doppler broadened cross section itself. The mean energy loss $\langle E - E' \rangle_{av}$ is calculated by the negative ratio of the first $A_1(E)$ and zeroth $A_0(E)$ energy moment (equation 1.16). In case of the DBRC kernel an energy gain is observed at the lower energy side of the resonance which is consistent with an increased up-scattering probability (figure 3.3). The standard MCNP scattering kernel however ignores the resonance and shows an almost flat mean energy loss in the entire considered energy range. As concluded in the previous subsection, neutrons are scattered towards the resonance energy when the correct physics is applied.

3.3.4 Angular Moments of the Scattering Kernel

In general, Monte Carlo transport codes like MCNP do not use Legendre moments to solve the transport equation. Nevertheless, a comparison of the Legendre moments (equation 1.13) of the Wigner-Wilkins scattering kernel used by the standard MCNP code and of the resonance dependent kernel, used by the DBRC MCNP version, illustrates the

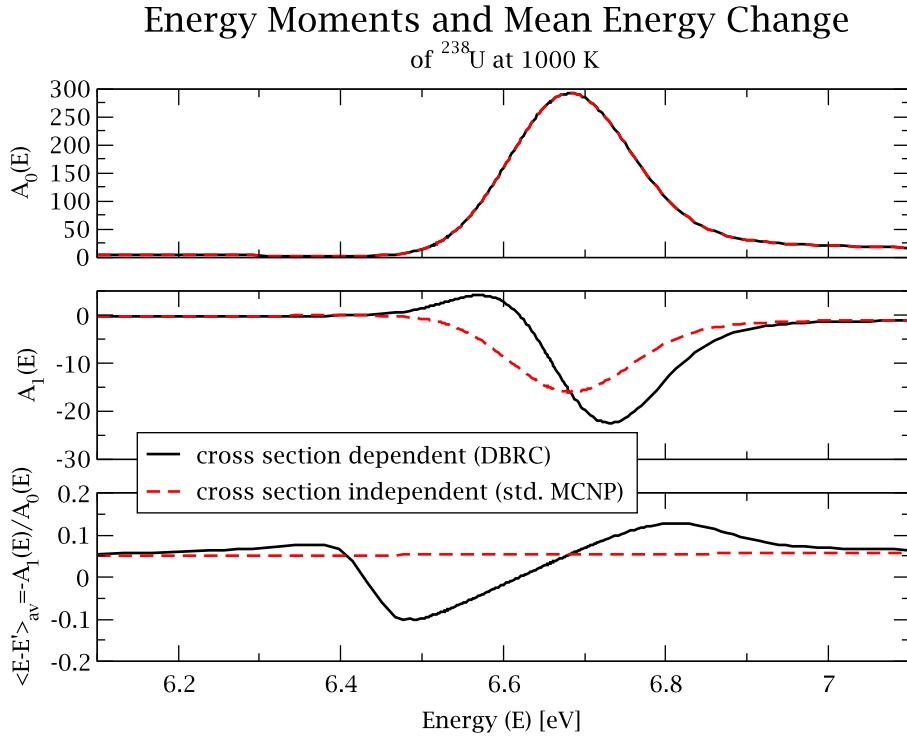


Figure 3.4: Energy moments and mean energy change of ^{238}U scattering kernel at 1000 K (std. MCNP and DBRC)

difference of secondary angular distribution of scattered neutrons. Figures 3.5 and 3.6 show the first and second moment of ^{238}U scattering kernel at 6.5 eV in the dip of the 6.67 eV resonance at 1000 K. Significant differences of the first and second moment are shown. In the case of the Wigner-Wilkins scattering kernel, most of the negative part of the first moment is on the down-scattering energy side while the negative part of the resonance dependent scattering kernel moment is on the up-scattering side. Backwards scattering dominates when the first moment becomes negative. The second moments of both kernels show strong deviations in the up-scattering region as well.

As mentioned in section 1.2.1, the angular Legendre moments of the scattering kernel can be used to determine the mean cosine of the scattering angle $\bar{\mu}_0^{lab}(E)$ by applying equation 1.14. Using the first moment of figure 3.5 at 6.5 eV and considering the Wigner-Wilkins approximation a mean cosine of the scattering angle $\bar{\mu}_0^{lab}$ of 0.00280 is obtained which means that scattering is slightly orientated in forward direction. This value is similar to the theoretical zero Kelvin mean cosine for ^{238}U calculated by equation 1.28. In case of the resonance dependent scattering kernel the mean cosine $\bar{\mu}_0^{lab}$ is -0.00344 and therefore slightly backwards directed.

3.4 The $S(\alpha, \beta)$ Probability Table Method

In this section, an alternative method to introduce the resonance dependent scattering kernel into Monte Carlo calculations is presented. This method is based on $S(\alpha, \beta)$

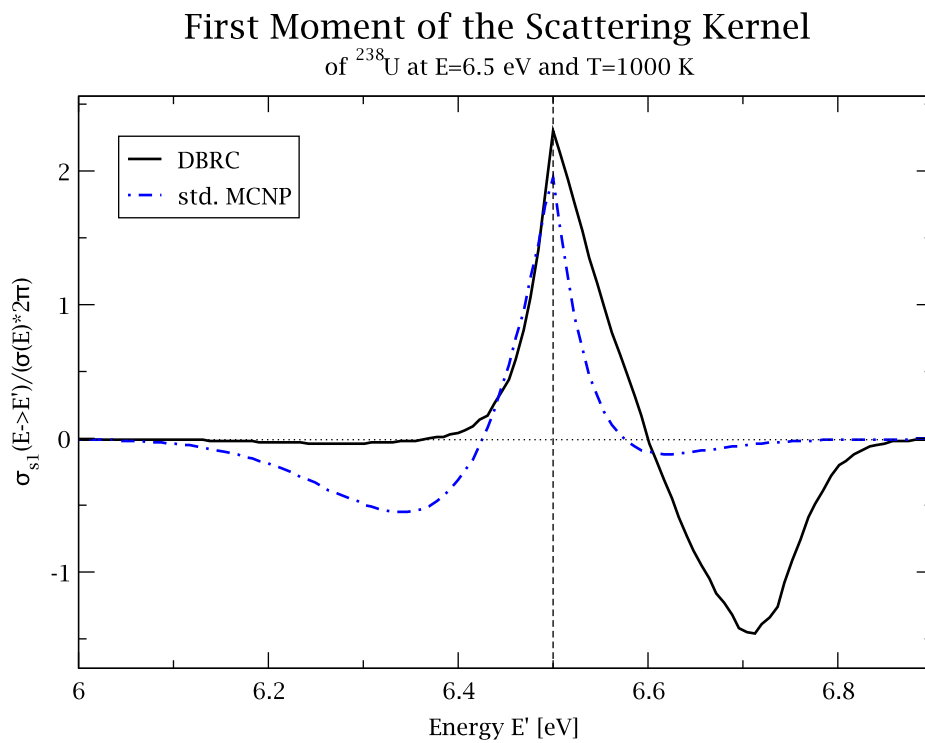


Figure 3.5: First angular moment of the ^{238}U scattering kernel at 6.5 eV and 1000 K (std. MCNP and DBRC)

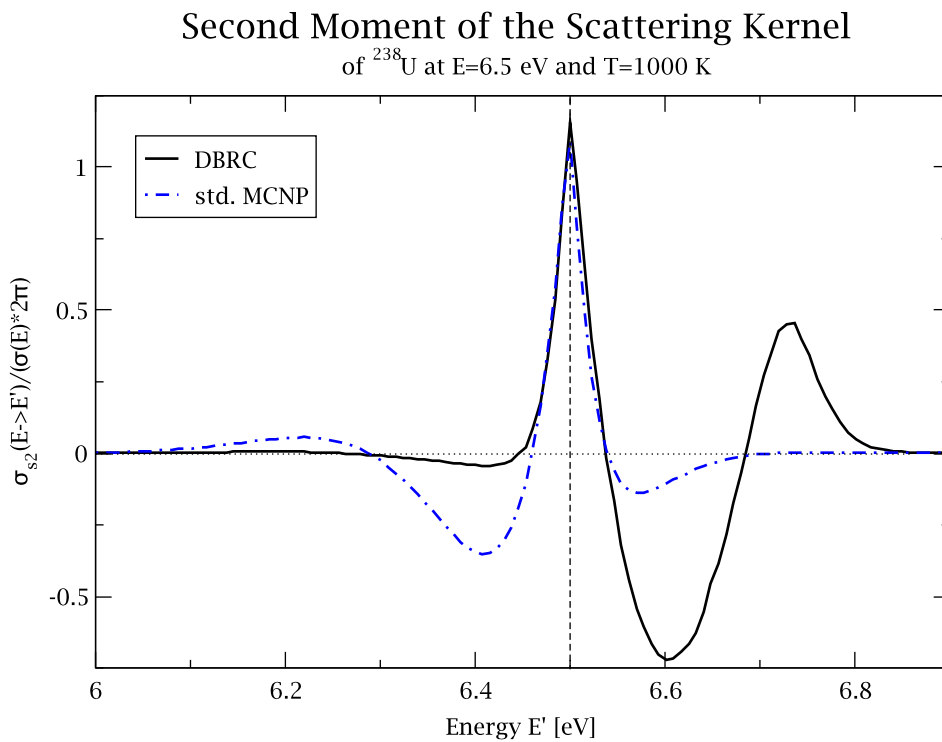


Figure 3.6: Second angular moment of the ^{238}U scattering kernel at 6.5 eV and 1000 K (std. MCNP and DBRC)

probability tables which are commonly used to account for the impact of solid state effects of light nuclei. The $S(\alpha, \beta)$ treatment is a complete representation of the neutron scattering. A coupled energy-angle representation can be derived from the ENDF $S(\alpha, \beta)$ scattering law:

$$\sigma_s^T(E \rightarrow E', \mu_0^{lab}) = \frac{\sigma_b}{4\pi k_B T} \sqrt{\frac{E'}{E}} e^{-\beta/2} S(\alpha, \beta) \quad (3.10)$$

where α and β are the momentum and energy transfer in dimensionless units:

$$\alpha = \frac{E + E' - 2\sqrt{EE'}\mu_0^{lab}}{Ak_B T}, \quad \beta = \frac{E' - E}{k_B T} \quad (3.11)$$

The $S(\alpha, \beta)$ term in equation 3.10 denotes the probability of a specific momentum and energy transfer. In the case of the short-time-collision approximation and energy independent cross sections, the $S(\alpha, \beta)$ term can be written as^[21]:

$$S(\alpha, \beta) = \frac{e^{-\frac{\alpha^2 + \beta^2}{4\alpha}}}{2\sqrt{\pi\alpha}} \quad (3.12)$$

The $S(\alpha, \beta)$ tables can be used in the MCNP code via the so-called "mt-card"^[37]. Typically three dimensional tables are used: for each point of the incident neutron energy scale a distribution of secondary energies is represented by a set of equal probable final energies. 16 or 32 equiprobable sets are commonly used for the secondary energies. For each of those sets a set of equally probable cosine bins is defined. MCNP samples first the secondary energy and then the scattering angle out of the probability sets. Linear interpolation is used inside a specific angle set.

In 2004, Rothenstein^[5] introduced the resonance dependent scattering kernel model into the THERMR module of the NJOY code^[25]. The model is based on a modified version of equation 1.47 suitable for fast numerical evaluations. This work enabled to generate resonance dependent $S(\alpha, \beta)$ tables for heavy nuclei which were first used by Dagan^[4] for ^{238}U in a LWR pin cell benchmark. The generated scattering tables covered an energy range of up to 210 eV. More than 1000 tables were necessary to take into account the important changes of the scattering kernel in the vicinity of resonances. In general, a fine energy grid has to be separately chosen for each nuclei due to the individual resonance structures. Therefore, $S(\alpha, \beta)$ tables are less practical to use than the more general DBRC method.

3.5 Summary

A new method for introducing the resonance dependent scattering kernel into Monte Carlo Codes is presented. This method, based on an idea of Rothenstein^[3], modifies the existing "Sampling of the Velocity of the Target nucleus" approach by using solely stochastic considerations. A detailed comparison of the new DBRC scattering kernel and the standard MCNP kernel shows significant differences of the secondary energy and angular distribution of scattered neutrons in the vicinity of cross section resonances. The transfer kernel, up- and down-scattering probabilities, energy moments and angular moments are used to illustrate these differences.

4 Validation of the DBRC Model

The implementation of the resonant scattering kernel effect and in particular the DBRC model raised the need for an experimental validation to confirm that the free gas model indeed governs the resonance scattering reaction and that the role of chemical binding effect^[45,46] is negligible. Two different kinds of experiments are presented: the Rensselaer Polytechnic Institute $^{238}\text{U}/^{232}\text{Th}$ scattering experiments and the CERN nTOF ^{232}Th capture yield experiment. In addition, the DBRC based calculations are compared to analytic $S(\alpha, \beta)$ based calculations for an LWR pin cell model.

4.1 RPI ^{238}U and ^{232}Th Scattering Experiment

In 2008, the Gaerttner Institutue of the Rensselaer Polytechnic Institute (RPI) in Troy, New York, performed the first ^{238}U scattering experiment dedicated to investigate the validity of the resonance dependent scattering kernel^[47,48,49]. In the experiment of Danon et. al., the RPI electron accelerator is used to create neutrons by bombarding a water cooled tantalum (Ta) target. These neutrons are thermalized in the coolant and in a polyethylene block located between target and sample. The produced thermal and epithermal neutrons hit a depleted ^{238}U sample which scatters the incident neutrons (as shown on figure 4.1). The experiment is based on the time of flight (TOF) method. The scattered neutrons enter a 25.6 m lang tube. At the end of this tube they are detected by a Li-Glass detector. This long flight distance is used to determine the neutron energy. Two different angles were analyzed: (1) 143.8° backwards scattering and (2) 38.9° forward scattering.

In the original study, Danon et al.^[47] compared the experimental results with a standard MCNP calculation, a MCNP calculation with enlarged energy range for the Wigner-Wilkins scattering method, a standard Geant4 calculation and an MCNP calculation with specific ^{238}U resonance dependent $S(\alpha, \beta)$ scattering tables (see section 3.4). Their comparison showed that only the $S(\alpha, \beta)$ based calculation agreed with the experiment in case of backscattering. In all other calculations the count rate of the neutrons scattered by resonances was about half the size of the experimental values. In case of the forward scattering, all calculations gave the same count rates and agreed well with the experiment. Similar results were obtained for the experiments with thin and thick targets. In order to validate the resonance dependent DBRC model the calculation of the scattering experiment is performed with the new implemented model. Complete agreement to the $S(\alpha, \beta)$ based calculation is found and consequently to the scattering experiment.

In 2009, the RPI experiment was redone using a ^{232}Th target. The experimental setup was arranged to obtain a backwards scattering angle of 156.7° . Two different ^{232}Th samples were: a thin sample of 0.1524 cm thickness with a density of $2.9265 \text{ } 10^{22} \text{ at/cm}^3$ and a thick sample of 0.3048 cm thickness with a density of $2.9364 \text{ } 10^{22} \text{ at/cm}^3$. Here the

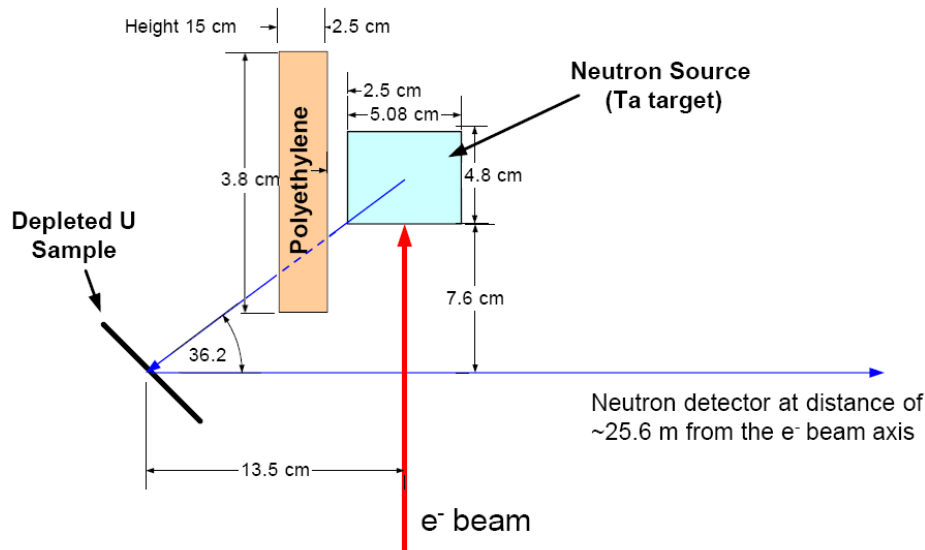


Figure 4.1: RPI scattering experiment for ^{238}U (presented at M&C 2009 meeting by Danon et al.^[47])

experimental result of the thin and thick target are used to validate the DBRC model.

Two different calculations are compared to the experiment. The first one is a MCNP calculation with enlarged energy range for the Wigner-Wilkins kernel. The second is a DBRC based calculation. TOF detector counts are simulated. Figures 4.2 and 4.3 show the comparison for the scattering reflection of the 69.2 eV resonance for the thin and thick target, respectively. A newly written code performs a regression analysis of the simulated detector counts to the experimental values. The sum of the squared residuals is minimized in an energy range of 67 eV to 71 eV. This energy interval is chosen as it includes the entire reflection peak, the selfshielding range of the resonance and a small part of the reflection of the higher energy wing of the resonance. It should be noted that this analysis focuses on the shape of the reflection rather than on the peak level. The simulated data is projected to the experimental energy grid using linear interpolation. The sum of the squared errors (SSE), the mean squared residuals SSE/N and the mean deviation of simulated and measured detector counts $\sqrt{SSE/N}$ are calculated.

A full agreement of the DBRC simulated detector counts and the experiment within the experimental uncertainty is found in case of the thin target (figure 4.2). The uncertainty of the experiment is estimated to be less than 10 % in the vicinity of the resonance scattering^[50]. The mean deviation of simulated and measured detector counts is $\sqrt{SSE/N}=15$ counts.

The Wigner-Wilkins based MCNP calculation underestimates the resonance reflection. The top of the resonance reflection is only about 72 % of the experimental counts. In addition, the width of the reflection is not calculated accurately. Therefore, the mean squared residuals is significantly larger than in the case of the DBRC simulation. The mean deviation is $\sqrt{SSE/N}=45$ counts.

The results of the experiment with the thicker ^{232}Th target are less evident than the results for the thin target. Nevertheless, the DBRC based calculation of the detector

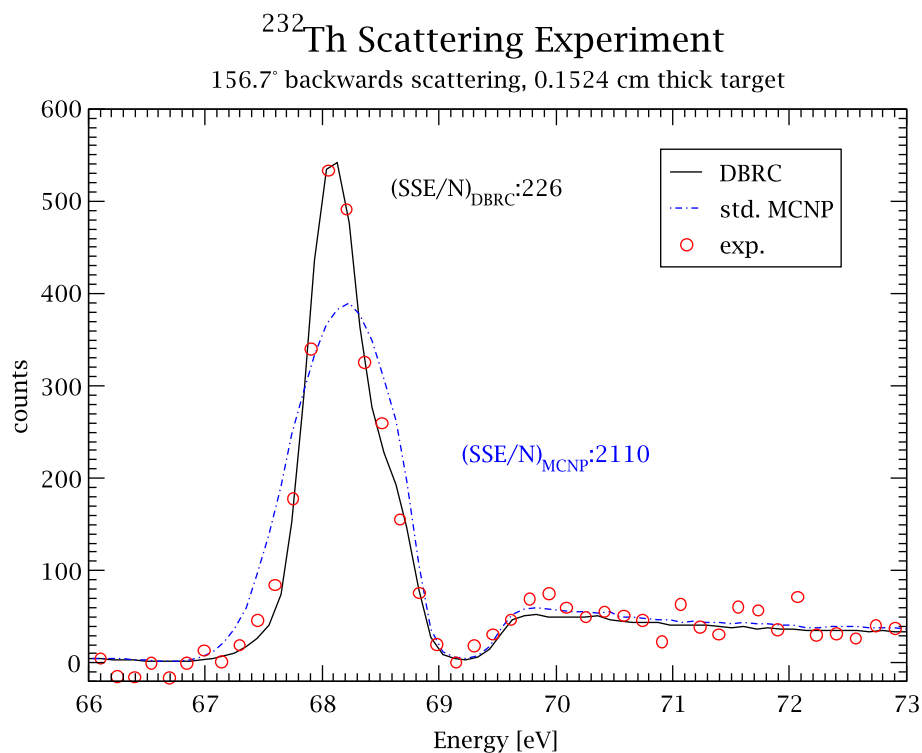


Figure 4.2: Comparison of the simulated and experimental ^{232}Th resonance scattering-counts for thin ^{232}Th sample

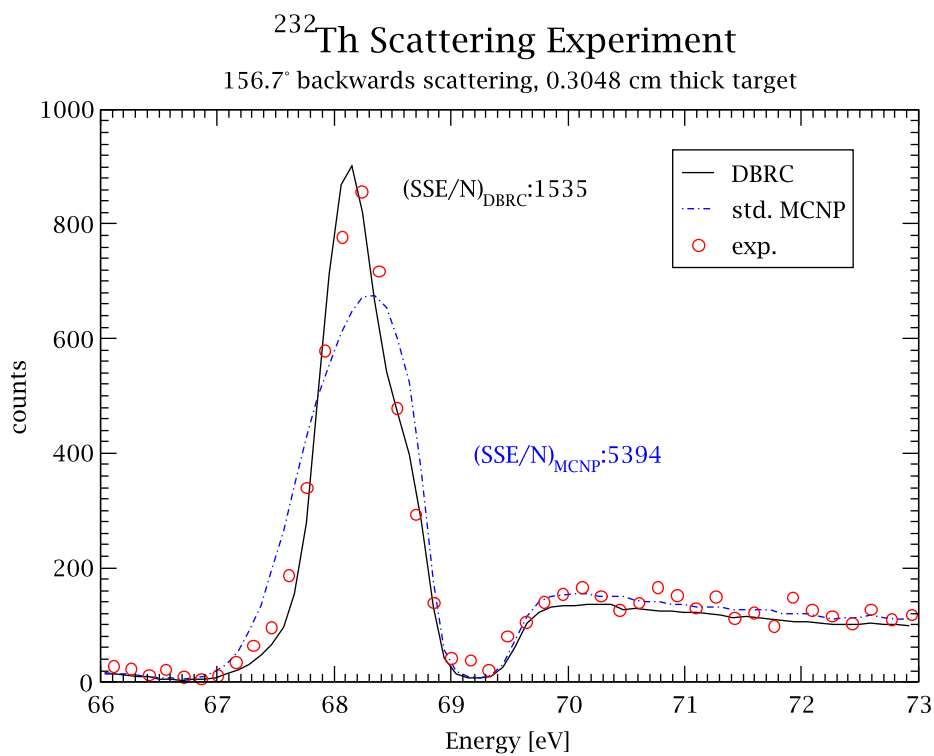


Figure 4.3: Comparison of the simulated and experimental ^{232}Th resonance scattering-counts for thick ^{232}Th sample

counts fit much better the experimental values than the standard MCNP based calculations, however the agreement is less distinct (figure 4.3). In case of the DBRC calculation, the mean deviation is 39 counts in the considered fit range. This mean deviation is 73 counts when the standard MCNP code is used. The MCNP underestimates the reflection peak (77 %) and over estimates the reflection width.

The ^{232}Th scattering experiments as well as the briefly mentioned ^{238}U experiment show clearly that the DBRC model introduced into MCNP improves the prediction capability of scattering experiment simulations with the MC code.

4.2 nTOF ^{232}Th Experiment

The second experiment being relevant for the resonance scattering kernel analysis was performed at the neutron time-of-flight facility nTOF at CERN^[51]. The CERN nTOF team measured the ^{232}Th capture cross section from 1 eV to 1 MeV. The CERN pulsed proton beam was used to create neutrons with a lead target. The used ^{232}Th sample consisted of 99.5 % purity and an isotopic thickness of 0.1 mm. The nTOF team observed that for some ^{232}Th resonances the measured resonance shape did not agree with the expected shape calculated by the data analysis code SAMMY^[53,20] or by MCNP. This was especially the case for the 69.2 eV resonance. Several studies were made to explain the difference between the simulation and the experiment while none of them, like the

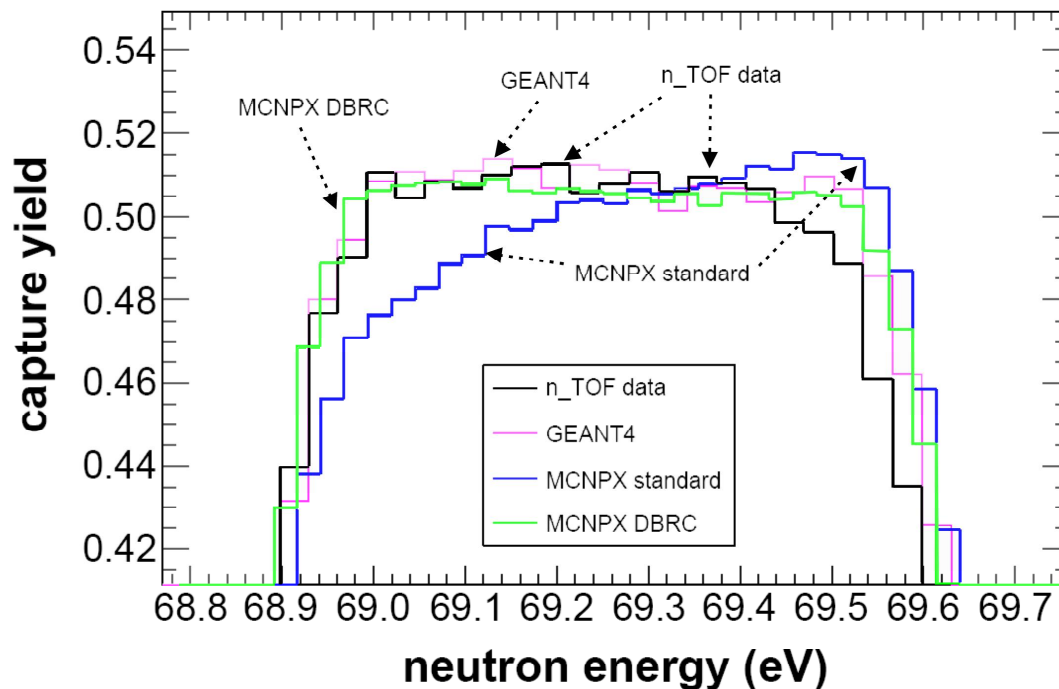


Figure 4.4: nTOF ^{232}Th capture yield experiment (by Gusing^[52]): capture yield calculated with standard MCNPX, with the resonance dependent version of GEANT4 and MCNPX DBRC in comparison to the nTOF experimental data

dead time of the detector or the background noise, was found to be coherent^[51]. Although the multiple scattering effect was considered, SAMMY uses the similar scattering model as MCNP^[54] (asymptotic model) based on constant cross sections and is therefore not accurate.

Gunsing^[52] investigated the impact of the resonance-dependent scattering kernel on the shape of the 69.2 eV ^{232}Th resonance. Gunsing integrated the zeroth moment of the resonance dependent scattering kernel (equation 1.52) into the Monte Carlo code GEANT4^[55]. He used the new developed DBRC model for MCNP as well. Figure 4.4 shows the saturated capture yield of the 69.2 eV resonance of the ^{232}Th experiment. The focus is on the shape of the saturated resonance which exhibits a flat tableau like behavior around the resonance energy.

Gunsing performed calculations of the capture yield with the modified GEANT4 code, the standard MCNP and with the DBRC version of MCNP (figure 4.4). Standard MCNP calculates a slope of the capture yield in the vicinity of the resonance energy. This clearly does not match the experimental results which exhibits a rather flat behavior of the capture yield. On the low energy side of the resonance standard MCNP largely under-predicts the capture yield while on the higher energy side it over-predicts the yield. Modified GEANT4 and DBRC MCNP, on the contrary, reproduce well the shape of the experimental capture yield with exception of the high resonance energy side where they slightly over-predict the capture yield.

4.3 Comparison of DBRC and $S(\alpha, \beta)$ Based MCNP Calculations

In this section, both methods to introduce the resonance dependent scattering kernel into MCNP, namely the DBRC method and the $S(\alpha, \beta)$ method, are compared based on simple MCNP test case calculations. A standard LWR pin cell model is used which is based on the geometrical specifications of a PWR subassembly benchmark proposed by Porsch et al.^[56]. An infinite array of identical fuel pins are modeled using reflective boundary conditions. The fuel enrichment is 4 w/% ^{235}U . A high fuel temperature of $T_F=1200$ K is assumed while clad and water temperature are 600 K. The criticality and the ^{238}U capture reaction rate are calculated.

$S(\alpha, \beta)$ scattering tables are prepared for ^{238}U with 1260 energy points which cover the energy range from 10^{-5} to 210 eV. 8 cosine and 16 cosine bins are used for the polar angle distribution. All standard and $S(\alpha, \beta)$ calculations are performed with MCNPX Beta Version 2.6.f. Cross sections are based on JEFF3.1 nuclear data files. The DBRC method was implemented into the MCNPX Beta Version 2.6.f. The following four different scattering options are applied for the ^{238}U neutron scattering:

1. The standard MCNP version is used which employs the ‘‘Sampling of the Velocity of the Target nucleus’’ (SVT) subroutine for neutrons with energy up to 400 k_BT.
2. Resonance dependent $S(\alpha, \beta)$ scattering tables are used (8 polar scattering cosine segments and an energy grid of 1260 points up to 210 eV to cover accurately all main S resonances in this energy range).
3. Resonance dependent $S(\alpha, \beta)$ tables with 16 scattering cosine segments are used.
4. The new DBRC option is used for neutrons with energy up to 210 eV.

Table 4.1: Criticality k_∞ of a LWR pin cell at $T_F=1200$ K applying different scattering models

Method		k_∞
(1)	standard MCNP: k_1	1.31137 +/-6E-5
(2)	$S(\alpha, \beta)$ (8 bins): k_3	1.30775 +/-6E-5
(3)	$S(\alpha, \beta)$ (16 bins): k_4	1.30772 +/-6E-5
(4)	DBRC: k_5	1.30791 +/-6E-5
<i>Differences:</i>		
	$k_2 - k_1$	-0.362 %
	$k_3 - k_1$	-0.365 %
	$k_4 - k_1$	-0.346 %
	$k_4 - k_3$	0.019 %

Table 4.2: Capture reaction rate of a LWR pin cell at $T_F=1200$ K applying different scattering models

Energy bin [eV]	Capture reaction rate r [<i>arb.Unit</i>] (sdev. (1σ) < 4E-6)			Differences (sdev. (1σ) < 0.13 %)		
	std. MCNP: r_1	$S(\alpha, \beta)$: r_2	DBRC: r_3	$\frac{r_2-r_1}{r_1}$	$\frac{r_3-r_1}{r_1}$	$\frac{r_3-r_2}{r_2}$
4.0 - 9.88	1.108E-02	1.110E-02	1.110E-02	0.22	0.22	0.00
9.88 - 16.0	4.129E-04	4.119E-04	4.117E-04	-0.24	-0.28	-0.04
16.0 - 27.7	6.173E-03	6.313E-03	6.311E-03	2.27	2.24	-0.03
27.7 - 48.1	4.799E-03	5.079E-03	5.062E-03	5.84	5.48	-0.34
48.1 - 75.5	2.328E-03	2.371E-03	2.370E-03	1.83	1.81	-0.02
75.5 - 149	4.227E-03	4.262E-03	4.249E-03	0.83	0.53	-0.30

The results of the pin cell study (Table 4.1) show that the criticality calculation which is based on the DBRC model (4) agrees well to the $S(\alpha, \beta)$ based calculations (2,3). The difference is within the range of $20 \cdot 10^{-5}$. The choice of either 8 or 16 cosine segments for the angular distribution of the $S(\alpha, \beta)$ table has a negligible influence on the criticality of the pin cell. The obtained criticality for the constant cross section scattering model (1) is by far higher in comparison to all resonance dependent scattering models (2,3,4). The difference ranges from 0.34 % to about 0.36 %.

In Table 4.2 capture reaction rates calculations are compared. The difference between the DBRC and the $S(\alpha, \beta)$ tables based calculations with 16 segments is less than 0.3 %. Contrarily, the standard MCNP calculation differs significantly from both, the DBRC and the $S(\alpha, \beta)$ tables algorithm by about 5.8 % and 5.4 %, respectively.

4.4 Summary

The scattering experiments as well as the neutron capture experiment show that the DBRC-method agrees much better with the experimental data than the standard MCNP-method. Through the experimental confirmation and by the comparison to the analytic based $S(\alpha, \beta)$ tables, it is assumed that a sufficient high degree of validation is reached for the DBRC scattering model. This implies the necessity of the implementation of the DBRC method. Beyond the common sense argument of the consistency of the transport equation (see 1.4) the enhanced impact on criticality and reaction rates is pronounced.

5 Impact of the Resonant Dependent Scattering Kernel on High Temperature Reactors

The impact of the temperature and cross section dependent scattering kernel on neutron physics calculations is investigated with regard to high temperature gas-cooled reactors (HTGR or HTR). In the first section a brief overview of different HTR designs is given. Then, the new DBRC scattering model integrated into MCNP is compared to the standard MCNP scattering model on the basis of unit cell calculations. This is done for both the compact and the pebble fuel element design. The HTR-10 and the HTTR fuel elements are used as reference designs. Finally, a detailed model of the entire Chinese HTR-PM core is studied with regard to the scattering models.

5.1 High Temperature Reactors

The HTR is one of the promising nuclear reactors for future energy production of the GEN-IV initiative^[6,57]. The future and current HTR designs emphasize inherent safety characteristics and a high coolant temperature leading to a high efficiency and possibilities for process heat applications .

Already in the 1950s gas cooled nuclear reactors were considered for electricity production which led to the construction and operation of the so-called MAGNOX reactors in the UK and France. These reactors used metallic natural uranium fuel pin design with a magnesium-aluminum cladding and pressurized CO₂ as a coolant. Their coolant outlet temperature was however limited to 415 °C. The MAGNOX reactors were followed by the Advanced Gas-Cooled Reactor (AGR) which used uranium oxide as fuel contained in a stainless steel cladding and reached a coolant outlet temperature of 675 °C, which later on had to be reduced.

In the 1960s, the development of a High Temperature Reactor cooled by Helium and based on spherical fuel elements, the so-called pebble-bed reactor, was initiated in Germany and led to the construction and operation of the "Arbeitsgemeinschaft Versuch-sreaktor" (AVR) pebble-bed reactor in 1968. The AVR had a power of about 45 MW. This research reactor effort was followed by the construction of the Thorium High Temperature Reactor (THTR) in the 1970s which went into operation in 1985. The THTR had a largely increased power (770 MW) and could reach an outlet temperature of 750 °C. Furthermore, the THTR was aimed to apply a thorium fuel cycle, using highly enriched (93 %) ²³⁵U with ²³²Th as the fertile material.

At about the same time when the HTR development started in Germany, the UK and the US HTR efforts focused on another type of reactors. In 1964, the OECD DRAGON reactor reached first criticality, which used special pin type fuel. In 1967, the US Peach

Table 5.1: HTR operating in the past

Reactor	MAGNOX/AGR	AVR	DRAGON	Peach Bottom	THTR	Fort St. Vrain
First power operation	1956	1967	1964	1967	1984	1976
Country	UK / France	Germany	UK	US	Germany	US
Power [MWe]	35-590	15	20 (th.)	40	300	330
Efficiency [%]	19-34	30	-	35	40	39
Fuel element	Slugs	Pebbles	Rods (hex.)	Cylinders	Pebbles	Hex. block
Fuel loading	Nat. U	UO ₂ /(U,Th)O ₂ /C ₂	U-ThC	U-ThC	U-ThO ₂	U-ThC
Enrichment ²³⁵ U [%]	0	10/17	93	93.5	93	93
Coolant	CO ₂	He	He	He	He	He
Coolant T _{out} [°C]	335-415	950	750	770	750	770
Power dens. [MW/m ³]	0.5-1.8	2.2	14	8.3	6.0	6.3

Bottom HTR using cylindrical fuel pins in hexagonal elements was constructed and went in operation. In 1968, the US began with the construction of the demonstration plant Fort St. Vrain which went critical in 1976. This reactor used also hexagonal fuel elements and was targeted to reach an outlet temperature of 770 °C.

Table 5.1 gives an overview of gas-cooled reactors that operated in the past.

5.1.1 HTR Design Characteristics

Nearly all HTR designs which are considered today use graphite both as structural material and as reflector material. Graphite is also the neutron moderator causing a thermal neutron flux spectrum depending on the HTR design. The fuel of this reactor type is distributed in the core in fine dispersed manner. Typically a uranium dioxide kernel is encapsulated into several protective layers which form coated fuel particles. The advantage of such fuel particles is that each microsphere represents essentially a safe barrier to retain all fission products during normal operation. These particles are introduced into a graphite matrix. The matrix and an additional protective graphite layer form the fuel elements. Spherical elements (pebbles) and cylindrical elements (compacts) are currently used.

The today's design HTR is cooled by Helium. Helium outlet temperatures of up to 1000°C are envisaged in order to reach a high efficiency of electricity production or to use the nuclear reactor for process heat applications. Due to dispersed coated particles in the graphite matrix the heat conductivity of the fuel elements is about the same as the heat conductivity of graphite. This enables relatively low fuel temperatures even though high coolant temperatures are reached.

The HTR TRISO Fuel Particle

The most commonly used coated particles are the so called TRISO particles^[58,59]. They consist of the fuel kernel and four surrounding shells:

- The UO₂ (or a UC) fuel kernel is the most inner part of the TRISO particle. It has a diameter of about 500 μm .
- The first shell is a porous carbon buffer layer of about 95 μm thickness. This layer provides a free volume for fission gases and prevents the coatings from damage caused by recoiling fission fragments and by overpressurization.

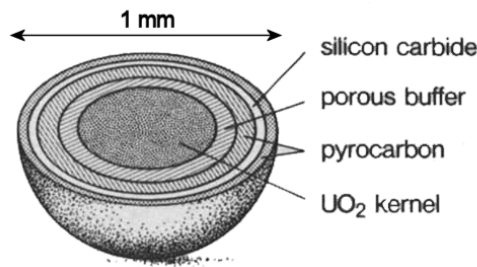


Figure 5.1: TRISO coated particle^[59]

- The second shell is the Inner Pyrolytic Carbon (IPyC) layer (ca. $40 \mu\text{m}$ thickness) with a high density which seals the porous carbon layer. This layer is the first part of the TRISO pressure vessel shell concept. This shell attenuates the fission product migration and reduces the chemical interaction of fission products with SiC layer.
- The third shell is a Silicon Carbide (SiC) layer (ca. $35 \mu\text{m}$ thickness). This shell provides strength for the coatings and acts as a strong fission products release barrier even at high temperatures up to 1600°C .
- The fourth shell is the Outer Pyrolytic Carbon (OPyC) layer (ca. $40 \mu\text{m}$ thickness). This second high density layer is again a fission products barrier and protects the SiC layer.

The TRISO particle concept has the high potential of retaining fission products up to a relatively high temperature: at normal operating conditions, the particles have a temperature of up to 1100°C . However, the TRISO particles are able to retain a high fraction of the fission products in accident scenarios where the temperature is below 1600°C . Below this temperature the particle maintain its integrity and only a fraction of about 4×10^{-5} of the TRISO particles show a defective coating (compared to 3×10^{-5} during normal operation). Figure 5.1 shows the TRISO particle with its fuel kernel and different protective layers.

It can be concluded that as long as the TRISO particle temperature stays below 1600°C any hazardous radiation dose to the environment can be excluded for a least ca. 500 hours in any accident^[59].

5.1.2 Current HTR Designs

Today there are basically two working HTRs in the world: the Chinese HTR-10 pebble-bed test reactor^[60] and the Japanese HTTR block type test reactor^[61]. The most advanced full scale HTR concept is the Chinese HTR-PM^[62] which is based on the German HTR-MODUL design^[63]. All three reactors designs are presented in the following and are of interest for the following studies concerning the impact of the resonance dependent scattering kernel.

HTR-10

The Chinese research and development program for the high temperature gas cooled reactor began in the mid-1970s with the the aim to construct a 100 MW thorium thermal

Table 5.2: HTR-10 like TRISO particle design

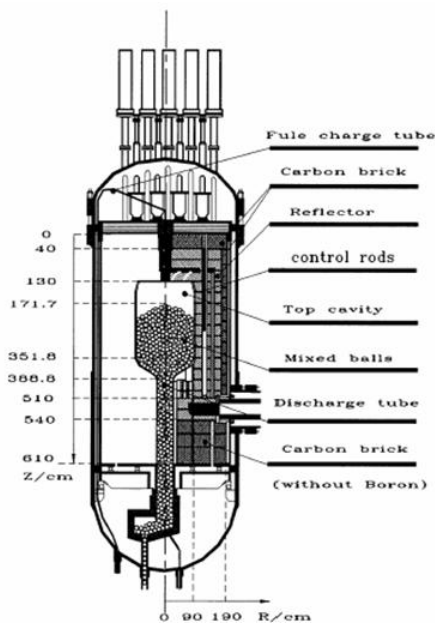
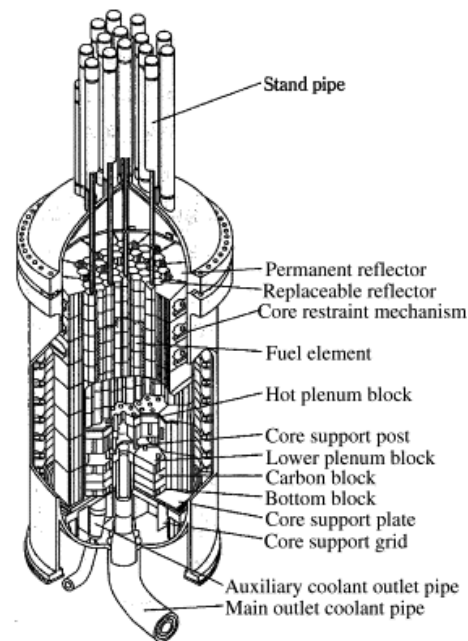
layer	material	thickness [cm]	density [g/cm ³]
fuel kernel	UO ₂	0.025 (radius)	10.4
buffer layer	graphite	0.009	1.1
inner carbon layer	pyrolytic graphite	0.004	1.9
SiC layer	silicon carbide	0.0035	3.18
outer carbon layer	pyrolytic graphite	0.004	1.9

breeder. Later the focus shifted towards an HTR design based on the HTR-MODUL (see below)^[60]. In 1988, the conceptual design of a 10 MW HTGR-Test Module (HTR-10) began at the Institute of Nuclear Energy Technology (INET) of the Tsinghua University in Beijing jointly with Siemens/Interatom^[64]. The main objective of the HTR-10 was to demonstrate the inherent safety features of the modular design. In 1992 the Chinese government approved to build the HTR-10.

The HTR-10 is a small sized test reactor. The active part of the reactor is formed of a pebble bed of 180 cm diameter and 197 cm in average height with 27000 pebbles (see figure 5.2). The mean power density at full power condition is 2 MW/m³. Each pebble contains about 5 g heavy metal (HM) which corresponds to about 8000 TRISO particles per pebble. The fuel kernel is made of UO₂ with 17 w% enrichment in ²³⁵U. The TRISO geometric specifications are given in table 5.2^[65].

The reactor can be continuously recharged with new or recycled pebbles from the top, while pebbles are discharged from below. The average residence time of the pebbles in the core is 1080 equivalent full power days (EFPD). An average burn up of 80 000 MWd/tHM is reached^[66].

The HTR-10 test reactor reached criticality in December 2000.

**Figure 5.2:** The Chinese HTR-10^[67]**Figure 5.3:** The Japanese HTTR^[61]

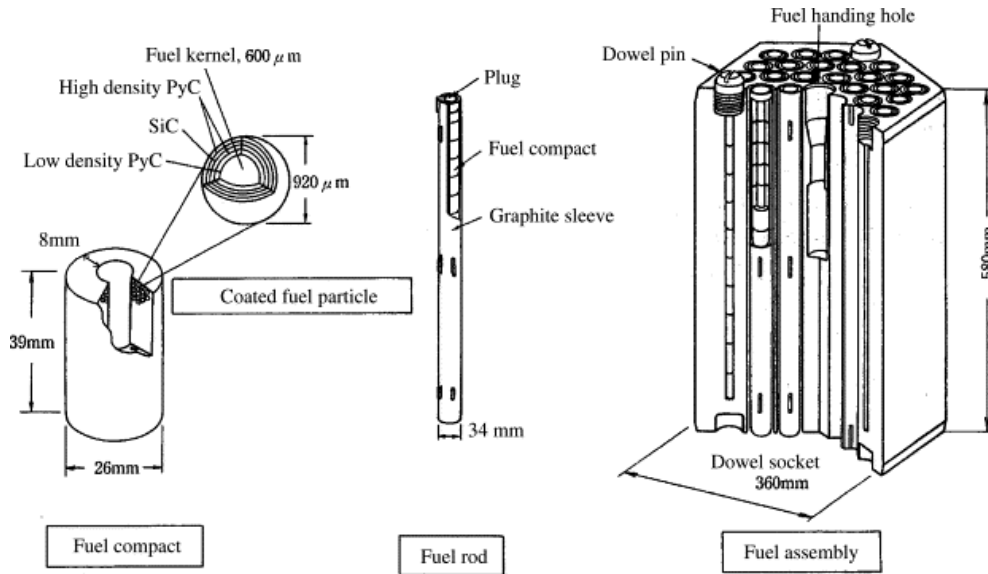


Figure 5.4: The HTTR fuel compact, rod and assembly^[61]

HTTR

The High Temperature Engineering Test Reactor (HTTR) was designed by the Japan Atomic Energy Research Institute (JAERI) and constructed at the Oarai Research Establishment in 1996^[61,68,69,70]. The main objectives of this reactor are to establish and upgrade the technology basis for advanced high temperature gas-cooled reactors and investigate high temperature heat applications. The HTTR uses prismatic fuel blocks and is designed to give a helium outlet temperature of 950°C and a thermal output of 30 MW. The first criticality was attained on November 10th in 1998 with an annular core of 19 columns, while full power operation was reached on December 7th 2001 with an average helium outlet temperature of 850°C. The aim is to have a hydrogen production test facility coupled to the HTTR by 2015.

The HTTR core has an annular design in order to ensure that the fuel temperature does not exceed 1600°C in case of loss of coolant accident. The annular design enhances the decay heat removal since the maximal heat transfer pass is reduced. The decay heat will be transferred through the fuel region, the side reflector and the reactor pressure vessel without any active cooling system needed.

The core is composed of prismatic hexagonal blocks of 580 mm in height and 360 mm in width across the flats. These blocks are either fuel assemblies, control rod guide blocks, replaceable reflector blocks or irradiation blocks. The active reactor core is in height 290 cm and 230 cm in diameter and consists of 30 fuel columns and 7 control rod guide columns (see figure 5.3). Each fuel column consists of 2 top reflector blocks, 5 fuel assembly blocks and 2 bottom reflector blocks. The replaceable reflector ring consists of 12 reflector columns, 9 control rod columns and 3 irradiation columns. The replaceable reflector ring is surrounded by the permanent reflector, which has an outer diameter of 425 cm and a height of 525 cm.

A block type HTR design has the possibility of fuel zoning and of burnable poison introduction compared to the pebble bed design. However an on-line refueling like for pebble bed reactors is not possible. Further, the entire active part of the HTTR core has

to be replaced at the end of a cycle.

Figure 5.4 shows the design of a fuel assembly. Depending on the location of the fuel assembly 31 or 33 fuel pin channels are bored into the hexagonal graphite block in addition to a fuel handling hole and three burnable poison holes. A fuel rod consists of graphite sleeve containing 14 fuel compacts. Each fuel compact contains about 13,000 coated TRISO fuel particles, which are embedded in a graphite matrix. 12 different low uranium enrichments (2-6 % ^{235}U) of fresh UO_2 fuel kernel are used throughout the core in order to flatten the axial and the radial power distribution^[71].

HTR-MODUL and HTR-PM

The HTR-MODUL reactor^[72,73] is the first HTR design concept which relies completely on inherently safety aspects. Its concept is based on a standardized pebble bed reactor unit of 200 MW which exhibit the inherently safety features of small high temperature reactors. By combining several units, it is possible to transfer these inherent safety features to power plants of any desired power rating^[63].

The HTR-MODUL is designed in a way that even in the case of complete loss of coolant and failure of all active cooling systems the temperature of the fuel elements remains within the limits at which there is practically no release of radioactive fission products. This temperature is 1600°C for the used fuel elements. An active core cooling system is not necessary for the decay heat removal during accidents since passive mechanisms for the heat removal are sufficient to keep the core within the designed temperature limit. Graphite is used as moderator and reflector materials. Unlike the common reactor designs, the HTR-MODUL has a ratio of height to diameter of about 3/1. This special design makes it possible to place the shut down and control rods solely in the reflector elements. No in-core absorber rods are necessary which would have to penetrate into the hot pebble bed by force. This requirement determines the maximal diameter of the active core to 3 m. The average active height of the core is about 9.4 m. The mean power density is limited to 3 MW/m³ and the mean core outlet temperature to 700°C. The maximum fuel element temperature during normal operation is 850°C.

The spherical HTR-MODUL fuel elements (6 cm diameter in total, 5 cm diameter of TRISO matrix) contain 7 g of uranium packed in about 11 600 TRISO particles. The ^{235}U enrichment is 7.8 %.

The HTR-PM is the next step of the HTGR development in China after the HTR-10 test reactor. The HTR-PM is based on the HTR-MODUL design concept with a slightly increased power^[62] while conserving the inherently safety features. The HTR-PM plant will consist of two nuclear steam supply systems, namely the core modules, which will feed one steam turbine. Each module consist of a single zone core with a power of 250 MW thermal and a steam generator.

The HTR-PM module has an active core diameter of 3 m and a height of 11 m offering space for about 420,000 fuel elements. The average power density is 3.22 MW/m³. Helium outlet temperature is 750°C permitting an electrical efficiency of 42 %. Similar fuel elements like for the HTR-MODUL and HTR-10 are used with a heavy metal loading of about 7 g per pebble. The UO_2 fuel of the TRISO particle is approximately 8.9 % enriched in ^{235}U since the design burn-up had been increased from 80 GWd/t to 90 GWd/t.

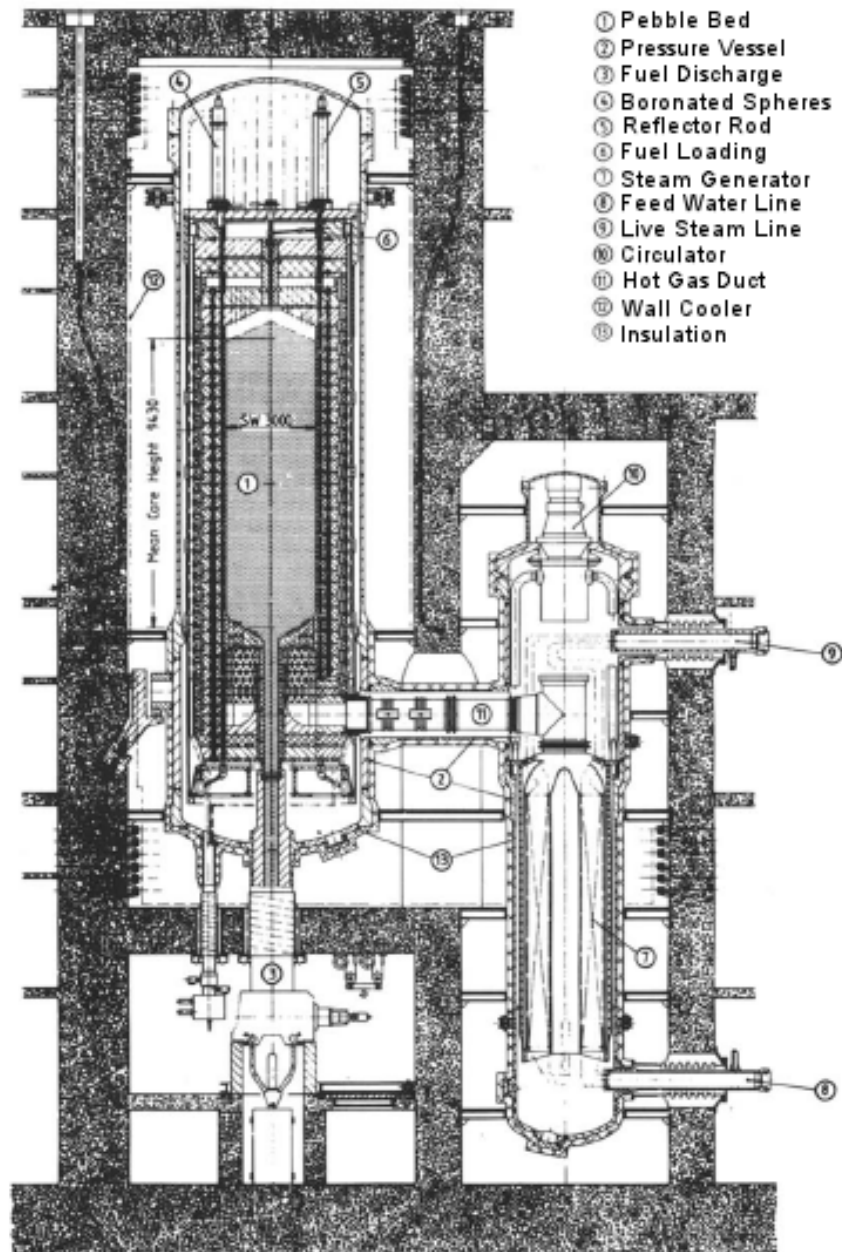


Figure 5.5: The HTR-MODUL reactor^[63]

5.2 HTR Unit Cell Calculations

Unit cell calculations are commonly used in deterministic codes to determine the neutron flux spectrum which is then used to condensate fine group or continuous cross section to broad group cross sections. In addition, for large reactor cores, where the leakage of neutrons out of the core is small, a unit cell calculation provides a good estimate of the core characteristics.

In this section, the impact of the resonance dependent scattering kernel on different unit cells is investigated. First, a unit cell consisting of TRISO particles in a graphite matrix is considered. Then, a unit cell with spherical fuel elements is investigated. Finally, the compact fuel elements are considered.

5.2.1 TRISO Matrix Unit Cell Study

The TRISO matrix, i.e. TRISO particles embedded in a graphite matrix, is the basis of the HTR concept. It is used by both the block type and pebble bed HTR designs.

In this section, the TRISO geometric design is similar to the HTR-10 TRISO design (see table 5.2). The enrichment of the UO_2 fuel is chosen to be 15 w% ^{235}U . Each layer is simulated explicitly. The TRISO particles are embedded in the matrix in a body cubic centered (BCC) way. Reflective boundary conditions are used at all six sides of the cubic unit cell. The temperature of the graphite matrix T_M is always kept constant at 1200 K.

A parametric study of the TRISO matrix with different TRISO packing fractions (TPF) and different kernel temperatures (T_f) is presented in the following. The TRISO packing factor is defined as the volume fraction of the TRISO particles in the matrix:

$$TPF = \frac{V_{TRISO}}{V_{MATRIX}} \quad (5.1)$$

Each calculation is performed twice: the first calculation is done with the standard MCNP version, the second one with the modified DBRC version of MCNP. The resonance dependent scattering kernel method is only used for ^{238}U . In this study, ^{238}U is expected to be the only nucleus influenced by the DBRC correction due to its well pronounced resonance structure. ^{235}U has as well a distinct resonance profile, however the neutron reaction rates are dominated by the fission process.

In the following, the impact of the resonance dependent scattering kernel on criticality and reaction rates is discussed. The influence of specific resonances and of the kernel size is analyzed.

Methodology of the Comparative Studies

All calculations are performed with MCNPX beta version 2.6f^[41,74] and JEFF3.1 cross section data^[13]. For the burn up studies the integrated burn up module CINDER of MCNPX is used.

An extended version of MCNPX beta version 2.6f is created which includes the DBRC scattering kernel. The improved resonance scattering treatment is carried out for energies of up to 210 eV if not otherwise specified. This energy range is chosen since it covers the first eight main S resonances of ^{238}U , which is the most important nucleus in this study.

It should be noted that the original scattering treatment in the relevant epithermal energy range is identical in MCNP(5) and MCNPX. The DBRC modifications are valid for both codes.

In the following, the corrected MCNP version will be referred as DBRC. The precision of the Monte Carlo calculations, i.e. the number of sampled histories per cycle and number per cycle, is chosen in a way that the results of the standard and DBRC MCNP-versions are well separated with regard to the standard deviations.

The DBRC version of MCNP need a higher computational effort compared to the standard version. This is mainly due to the multiple rejections of sampled targets. For unit cell calculation the computational time increases by up to 20 %. For full core calculations the increase is less than 5 %.

Influence of the DBRC Kernel on Criticality

The multiplication factor of the DBRC based ($k_{\infty,DBRC}$) and std. MCNP based ($k_{\infty,std.MCNP}$) calculations are depicted in table 5.3 for different TPF and fuel temperatures. The criticality shift:

$$dk/k = \frac{(k_{\infty,DBRC} - k_{\infty,std.MCNP})}{k_{\infty,std.MCNP}} \quad (5.2)$$

is plotted in figure 5.6. The criticality of the DBRC calculation is always lower than the one of the std. MCNP calculation. The difference increases with increasing packing fraction and fuel temperature up to -1.250 %. Here, the temperature is important since the deviation of the Wigner-Wilkins (and more over of the 0 K scattering kernel) to the resonance dependent scattering increases with temperature. The fuel to moderator

Table 5.3: Criticality of the TRISO matrix in dependence of TRISO packing fraction (TPF) and fuel temperature

TPF [%]	DBRC		std. MCNP	
	$k_{\infty,DBRC}$	sdev. (1σ)[10^{-5}]	$k_{\infty,std.MCNP}$	sdev. (1σ)[10^{-5}]
T _f =800 K				
1	1.68391	25	1.68467	26
10	1.27481	36	1.27975	38
25	1.04738	31	1.05227	32
35	1.0099	31	1.01431	27
T _f =1200 K				
1	1.67476	31	1.67579	29
5	1.44815	36	1.45363	39
10	1.2333	38	1.23986	37
15	1.11494	38	1.12196	42
25	1.00772	32	1.01535	31
35	0.97467	29	0.9824	26
T _f =1800 K				
1	1.66486	26	1.66628	27
10	1.18638	37	1.19711	36
25	0.96151	36	0.97393	31
35	0.9349	29	0.94658	27

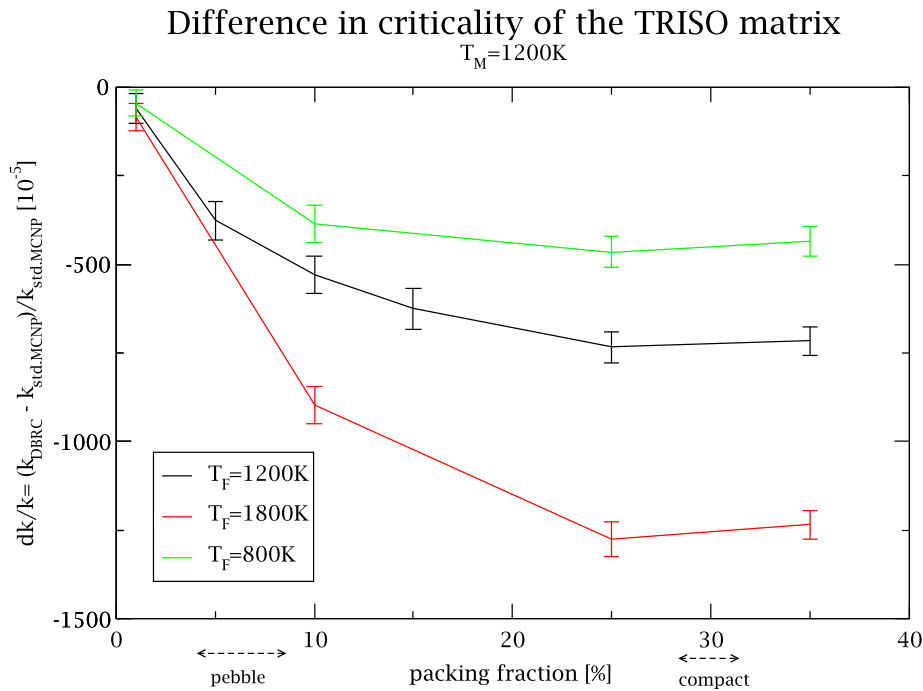


Figure 5.6: Difference of criticality between DBRC and std. MCNP based calculations for different TRISO matrix packing fractions and temperatures

ratio determines the neutron spectrum in the fuel kernels (see figure 5.7). The flux is shifted towards the resonance region with increasing TPF . Therefore the influence of the resonance dependent scattering model increases with the TRISO packing factor. The packing fraction of an HTR pebble ranges from 5 % to 10 %. In case of an HTR compact the packing fraction is about 30 %.

Influence of the DBRC Kernel on Reaction Rates

The influence of the resonance dependent DBRC kernel on the capture reaction rate of ^{238}U in the fuel kernel of the TRISO particles is studied for different TPF at $T_f=1200\text{ K}$ (see figure 5.8). Different energy groups are used. It is important to note that the first three main S resonances of ^{238}U at 6.67 eV, 20.87 eV and 36.7 eV are in energy groups two, four and five, respectively. The energy group seven gives the ^{238}U neutron capture reaction over the total energy range up to 10^7 eV . The main increase of the neutron capture of up to 6 %, due to the new DBRC model, takes place in the vicinity of the 20.87 eV and 36.7 eV resonances in groups four and five.

For higher TPF the neutron capture in the first three groups decreases to some extent. Due to the increased neutron absorption of the pronounced resonances in groups 4 and 5, the resonance escape probability of those resonances decreases. Therefore the flux, and consequently the absorption in these groups, decreases when the DBRC model is used.

The total neutron capture of ^{238}U increases by about 0.5 % to 1 % depending on the TPF. This increased neutron capture of ^{238}U leads to a decrease of the multiplication factor as shown in figure 5.6 and leads subsequently to a higher ^{239}Pu production as will

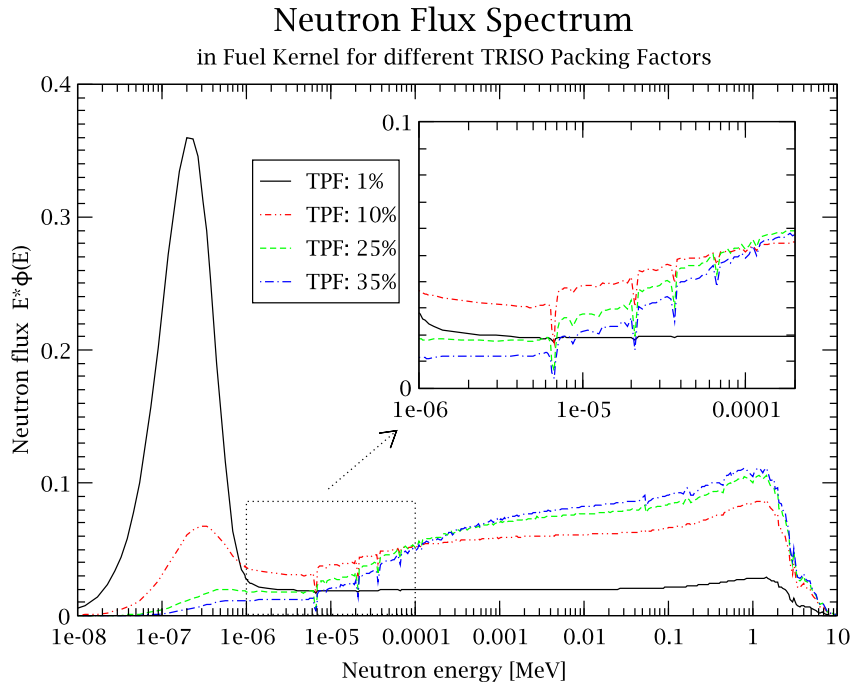


Figure 5.7: Neutron spectrum for different TPF at $T_f=1200$ K

be discussed in section 5.2.2.

Influence of DBRC Kernel of Specific Resonances on Criticality

The influence of the resonance dependent scattering kernel on reactor parameters differs strongly from each resonance. Evidently, the height of the resonance, e.g. σ_0 in the SLBW formalism, is important. The resonance energy is also of interest as it determines how strong the Doppler broadening effect on the scattering kernel is. And finally the ratio of the scattering to total Γ -widths Γ_n/Γ_t conditions the probability of a scattering event at the resonance energy. An important parameter is therefore the ratio Γ_n/Γ_γ which indicates whether a resonance is dominated by radiative capture or by scattering (see table 5.4). A low ration ($\Gamma_n/\Gamma_\gamma < 1$) implicates that capture is more probable than scattering.

Figure 5.9 shows the neutron flux in the vicinity of the first four main S resonances of ^{238}U of the DBRC and std. MCNP calculation. For this comparison, a high TPF of 35 % is chosen due to the well pronounced influence on the scattering model. For the 6.67 eV resonance, the neutron fluxes based on the different scattering models show only small deviations. This resonance is dominated by neutron absorption. The ratio of the scattering and radiative Γ -widths Γ_n/Γ_γ is about 0.064. In the vicinity of the 20.87 eV resonance the DBRC based neutron flux deviates from the standard MCNP flux on the lower energy side of the resonance. Standard MCNP calculations largely overestimates the flux. This resonance has a Γ_n/Γ_γ ratio of about 0.440 which enhances the importance of the resonance dependent scattering kernel. The 36.7 eV resonance flux with a Γ_n/Γ_γ ratio of 1.466 shows a similar behavior. Again an overestimation of the flux on the lower

Difference of Capture Reaction Rate for std. MCNP and DBRC Calculation

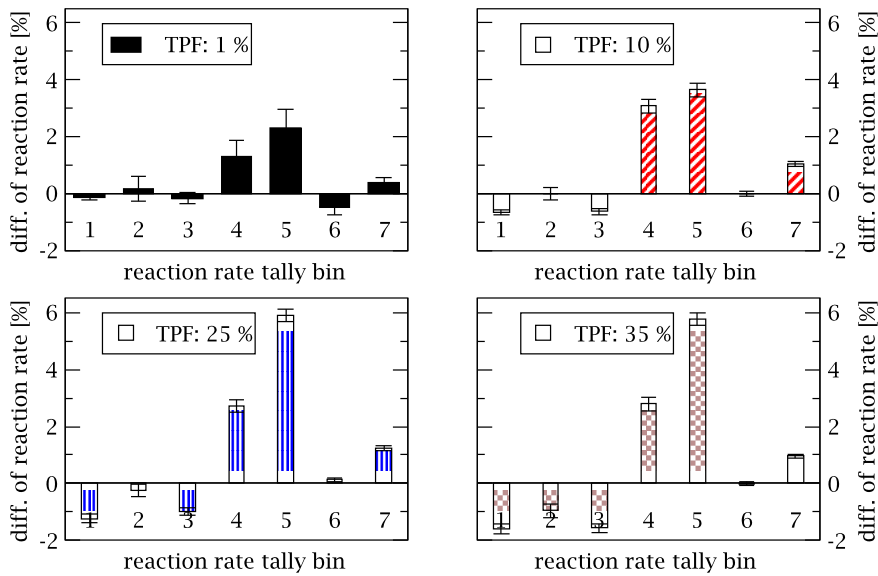


Figure 5.8: Relative difference of the (n,γ) reaction rate of ^{238}U of DBRC and std. MCNP based calculations for different packing fractions TPF ($T_f=1200$ K). Energy groups [eV]: 1: 0.0 - 4.0, 2: 4.0 - 9.877, 3: 9.877 - 15.97, 4: 15.97 - 27.7, 5: 27.7 - 48.05, 6: 48.05 - 10^7 , 7: total range

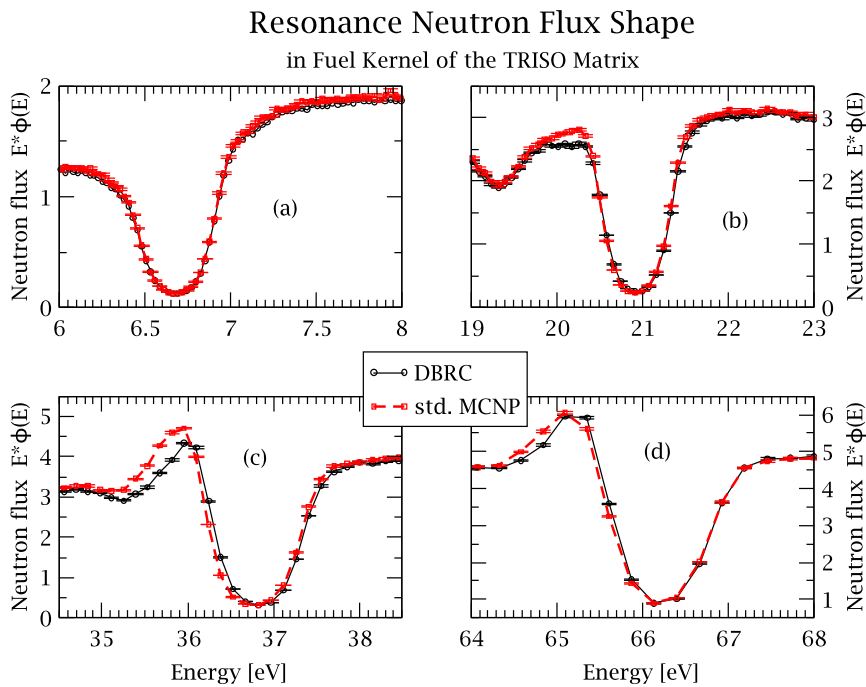


Figure 5.9: Comparison of neutron flux in the vicinity of four ^{238}U resonances for DBRC and std. MCNP based calculations (TPF=35 % and $T_f=1200$ K)

Table 5.4: Resonance parameter of ^{238}U s-wave resonances between 0 and 210 eV

E_0	Γ_t	Γ_n	Γ_γ	σ_0	Γ_n/Γ_t	Γ_γ/Γ_t	Γ_n/Γ_γ
6.673	2.448E-02	1.476E-03	2.300E-02	2.372E+04	0.060	0.940	0.064
20.871	3.298E-02	1.007E-02	2.291E-02	3.842E+04	0.305	0.695	0.440
36.682	5.644E-02	3.355E-02	2.289E-02	4.255E+04	0.594	0.406	1.466
66.030	4.759E-02	2.423E-02	2.336E-02	2.025E+04	0.509	0.491	1.037
80.747	2.488E-02	1.877E-03	2.300E-02	2.453E+03	0.075	0.925	0.082
102.557	9.445E-02	7.103E-02	2.342E-02	1.925E+04	0.752	0.248	3.033
116.893	4.833E-02	2.534E-02	2.299E-02	1.178E+04	0.524	0.476	1.102
145.665	2.441E-02	8.848E-04	2.353E-02	6.533E+02	0.036	0.964	0.038
165.316	2.726E-02	3.199E-03	2.407E-02	1.864E+03	0.117	0.883	0.133
189.681	1.939E-01	1.704E-01	2.356E-02	1.216E+04	0.879	0.121	7.231
208.525	7.285E-02	4.994E-02	2.291E-02	8.633E+03	0.686	0.314	2.180

based on *JEFF3.1*^[13] and *JANIS 3.0*^[14]

energy side of the resonance can be noticed. The fourth ^{238}U main S resonance at 66.0 eV has a Γ_n/Γ_γ ratio of about 0.512. Std. MCNP still overestimates the neutron flux but due to the higher energy the differences become smaller.

In order to investigate the influence of specific resonances on the criticality of the pebble unit cell the DBRC scattering model is applied only in certain energy intervals (see table 5.5). In the remaining energy interval up to 210 eV the Wigner-Wilkins scattering model is used. The energy segmentation is chosen in a way that the first 3 s-wave resonances lie within separated segments. The higher energy range is divided into three intervals. The DBRC kernel applied in the vicinity of the 36.7 eV resonance has the strongest impact on k_∞ compared to the case where only the Wigner-Wilkins kernel is applied ($k_{\infty,WW}$). The criticality shift is about -0.5 %. This shift reduces to -0.274 % in case of the influence of the 20.87 eV resonance scattering kernel. The influence of the first ^{238}U resonance is low due to the Γ_n/Γ_γ ratio of 0.064. The impact of the higher resonance is small. The criticality difference is only of the order of two standard deviations. Dagan^[4] found that in case of an LWR pin cell the influence of the higher ^{238}U resonances (50 eV - 210 eV) is less than 10 % of the total effect of the resonance dependent scattering kernel.

Table 5.5: Influence of the ^{238}U resonance dependent scattering kernel of specific energy intervals

DBRC energy range [eV]	k_∞	sdev. (1σ)[10^{-5}]	$k_\infty - k_{\infty,WW}$ [10^{-5}]	sdev. (1σ)[10^{-5}]
– ($k_{\infty,WW}$)	0.98255	27	–	–
4 - 13	0.98199	27	-56	38
13 - 28	0.97981	25	-274	37
28 - 50	0.97769	27	-486	38
50 - 90	0.98231	28	-24	39
90 - 150	0.98281	29	26	40
150 - 210	0.98236	27	-19	38
4 - 210	0.97467	29	-788	40

5.2.2 HTR Fuel Pebbles

In a pebble bed reactor, the above studied TRISO matrix is introduced in spherical fuel elements (pebbles). In most designs the pebbles consist of a spherical fuel matrix zone with a radius of 2.5 cm and a pure graphite protective layer of 0.5 cm thickness. These pebbles are then introduced in the reactor core. They occupy about 61 % of the core's volume when randomly distributed in the core i.e. the Pebble Packing Factor (PPF) is 0.61.

In this section, unit cells of pebbles with different heavy metal loading are studied in view of the resonance dependent scattering treatment and the introduced reactivity shift. The unit cell consists of Body Cubic Centered (BCC) arranged pebbles. The optimal PPF in a BCC lattice is 0.68. In the unit cell case the BCC pitch between the pebble is chosen to give a PPF of 0.61. This means that there is a small gap between the pebbles. The TRISO particles in the matrix of the fuel zone of the pebble are arranged in a BCC lattice as well. The TPF is chosen to give a specific heavy metal (HM) content per pebble. Each TRISO layer is model individually.

The reference pebble design is based on the HTR-10 pebble with the geometry data given in table 5.2. Due to the small sized core of the HTR-10 the neutron leakage is high (about 30 %^[65]). Therefore the enrichment of the fuel is relatively high (17 w% ²³⁵U). The HTR-10 reference heavy metal loading per pebble is 5 g which corresponds to a TPF of 5.3 %. The graphite temperatures of the matrix and of the pebble shell are constant in all studied cases and assumed to be 1200 K while the fuel temperatures varies from 800 K to 1800 K.

Influence of the DBRC Kernel on the Pebble Unit Cell Criticality

Table 5.6 gives the criticality of the unit cell calculations for the different considered cases. The standard MCNPX scattering model and the resonance dependent DBRC scattering model are used. The negative Doppler reactivity effect of the UO₂ fuel decreases the criticality with increasing fuel temperature for all cases. In addition, the criticality decreases with increasing heavy metal loading per pebble due to lower moderator to fuel ratio. The relative difference of the criticality dk/k depending on the scattering model are shown in figure 5.10. For all considered cases there is a clear trend to an increased negative reactivity shift with increasing temperature. The case of 12 g HM per pebble and 1800 K fuel temperature gives the most significant criticality shift of about -0.600 %. This shift can be related to a deviation of the neutron flux in the vicinity the ²³⁸U resonances and the corresponding increased neutron absorption in the same manner as it is show in section 5.2.1. At $T_F=1200$ K the neutron absorption of ²³⁸U is underestimated by standard MCNP of about 1.1 % and 1.3 % for the case of 5 g and 10 g HM per pebble, respectively.

Influence of the DBRC Kernel on the Doppler Reactivity Coefficient

Since the criticality shift between the approximating standard MCNP scattering model and the resonant dependent DBRC model increases with temperature it is of high interest to study the Doppler reactivity fuel coefficient. This temperature coefficient takes into account the increased neutron absorption by Doppler broadened resonances when the

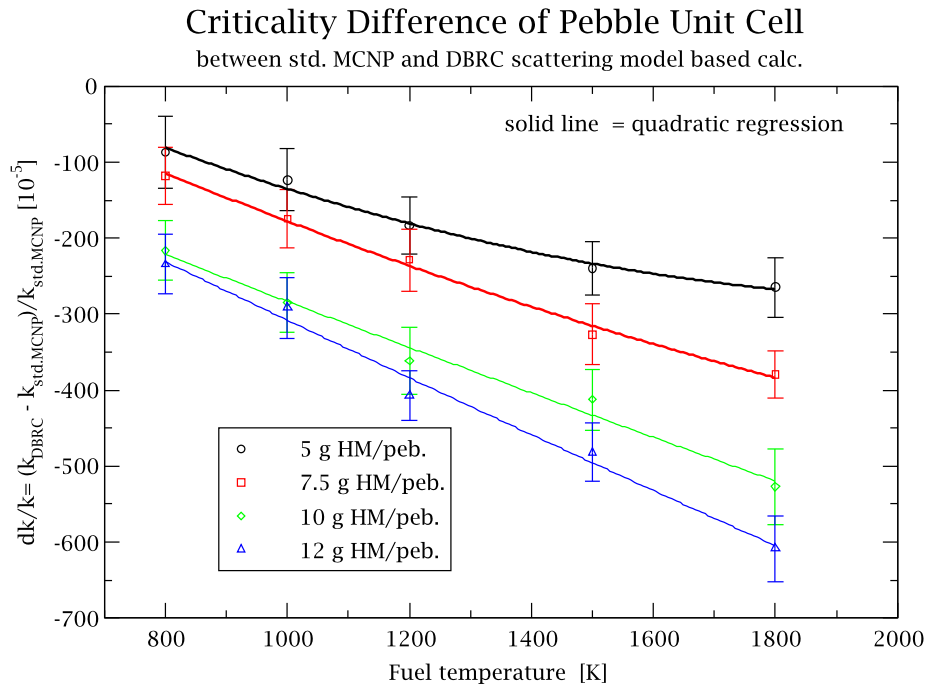


Figure 5.10: Difference in criticality between DBRC and std. MCNP based calculations for different HM contents and fuel temperatures

Table 5.6: Criticality of a pebble unit cell for different HM contents and fuel temperatures

HM/peb. TPF	5 g 5.3 %		7.5 g 7.54 %		10 g 10.05 %		12 g 12.06 %	
	k_{∞}	sdev.(1 σ) [10 ⁻⁵]	k_{∞}	sdev.(1 σ) [10 ⁻⁵]	k_{∞}	sdev.(1 σ) [10 ⁻⁵]	k_{∞}	sdev.(1 σ) [10 ⁻⁵]
<i>Fuel Temperature: 800 K</i>								
std. MCNP	1.63131	34	1.55031	26	1.47312	28	1.42845	27
DBRC	1.62989	34	1.54848	27	1.46993	27	1.4251	28
<i>Fuel Temperature: 1000 K</i>								
std. MCNP	1.61998	29	1.53625	29	1.45649	29	1.4105	30
DBRC	1.61737	29	1.53317	26	1.45195	27	1.40639	27
<i>Fuel Temperature: 1200 K</i>								
std. MCNP	1.61038	27	1.52349	32	1.44219	34	1.39549	33
DBRC	1.60775	25	1.52001	26	1.43698	28	1.38981	28
<i>Fuel Temperature: 1500 K</i>								
std. MCNP	1.59834	25	1.50823	28	1.42319	28	1.37566	28
DBRC	1.59451	25	1.5033	28	1.41732	29	1.36903	26
<i>Fuel Temperature: 1800 K</i>								
std. MCNP	1.58811	30	1.49472	31	1.40799	41	1.35897	32
DBRC	1.58391	25	1.48905	28	1.40057	28	1.3507	28

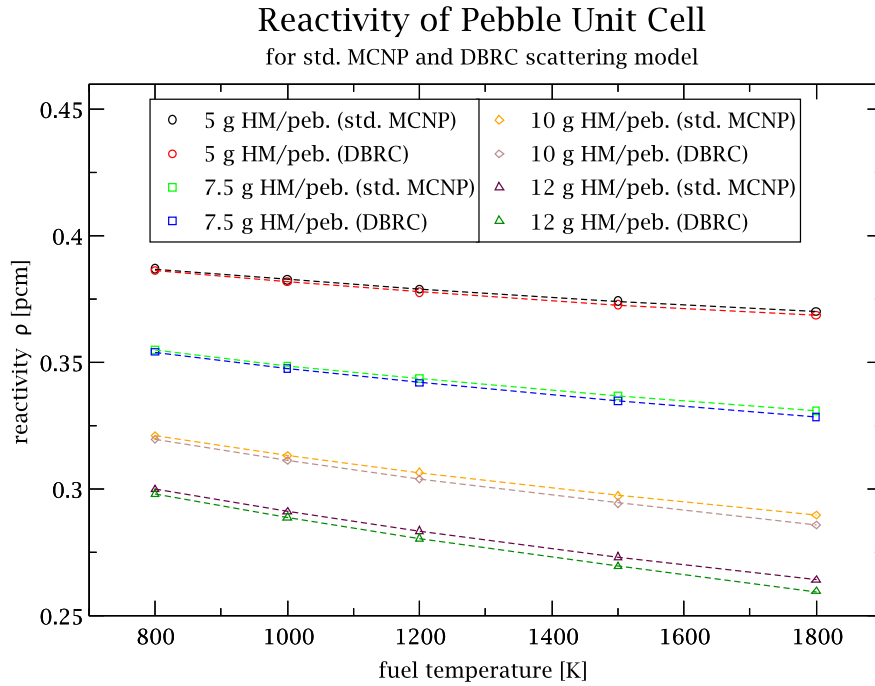


Figure 5.11: Pebble unit cell reactivity calculated with DBRC and std. MCNP for different HM contents per pebble and fuel temperatures

fuel temperature T_F increases. The Doppler effect is primarily due to the epithermal resonances of non fissionable fuel nuclei like ^{238}U .

It can be defined as^[8]:

$$\alpha_{T_F}^D = \frac{\partial \rho}{\partial T_F} \quad (5.3)$$

where ρ is the reactivity defined as:

$$\rho = \frac{k - 1}{k} \quad (5.4)$$

Figure 5.11 shows the reactivity ρ of the standard MCNP and DBRC based pebble unit cell calculations which correspond to the criticality values of table 5.6. Evidently, the reactivity shows the same behavior as the criticality i.e. with increasing temperature and heavy metal content, the reactivity decreases.

Cubic regressions are performed in order to fit an equation $\rho(T)$ to the reactivity values of figure 5.11. The derivation of these equations give the Doppler reactivity coefficients as a function of temperature $\frac{\partial \rho(T)}{\partial T}$ with respect to the standard deviations of the initial criticality calculation. Figure 5.12 indicate the trend of the temperature dependent Doppler reactivity coefficient. For higher fuel temperatures the feedback becomes smaller i.e. the coefficient gets less negative. The feedback increases with the HM content due to higher amount of the main resonance absorber ^{238}U . For all considered pebbles and temperatures the DBRC based Doppler reactivity coefficient calculations (dashed lines) are more negative than the standard MCNP based coefficient (solid lines). The difference between the two calculations range from 5 % to 10 %. In other words, the standard version of

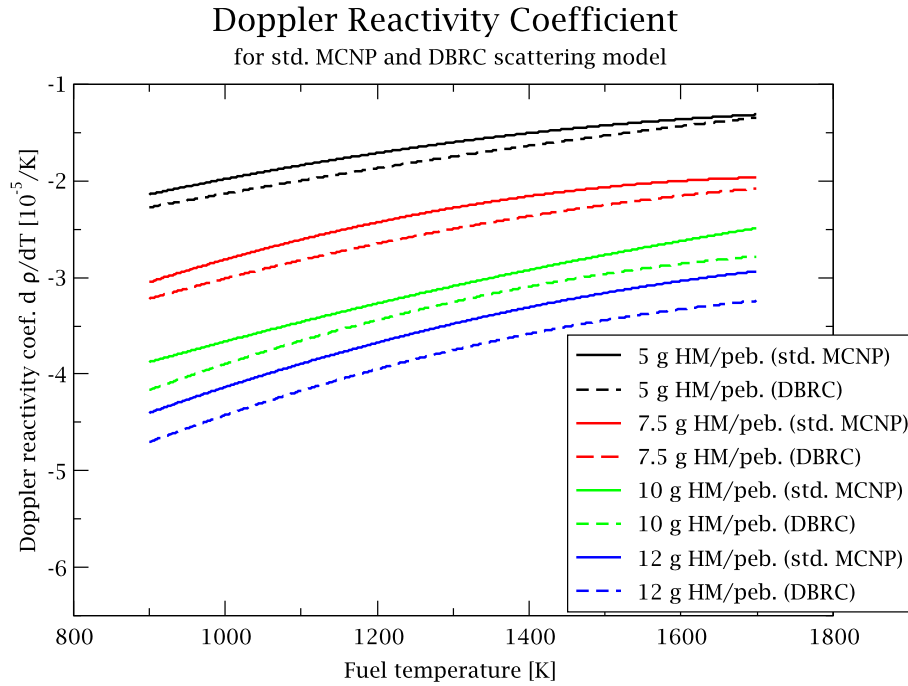
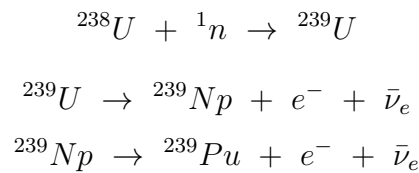


Figure 5.12: Pebble unit cell Doppler reactivity coefficient calculated with DBRC and std. MCNP for different HM contents and fuel temperatures

MCNP largely underpredicts the Doppler reactivity feedback especially for higher HM content pebbles.

²³⁹Pu Concentration and Criticality during Burn up

The previously discussed reactivity shift between the standard MCNP model and the resonance dependent DBRC scattering model is due to an increased neutron capture of ²³⁸U. This leads to an increased production of the fissile Pu isotope ²³⁹Pu via the production chain of a neutron capture and two subsequent beta decays:



where ²³⁹U and ²³⁹Np decay (β^- decay) by emission of an electron e^- and an antineutrino $\bar{\nu}_e$ with the half life of $T_{1/2}^{239\text{U}}=23.5$ min and $T_{1/2}^{239\text{Np}}=2.33$ days, respectively.

The 5 g and 10 g heavy metal per pebble units cell cases are used to perform burn up studies. An HTR-10 like power density of 370 W per pebble is chosen. Fuel and graphite temperatures are 1200 K. It is assumed that solely the fuel composition changes during burn up. All TRISO fuel kernels deplete uniformly up to a burn up rate of about 140 GWd/t. This rate is larger than the reference HTR-10 BU of 80 GWd/t. Collision rates of ²³⁸U are calculated with an uncertainty of less than 0.1 % in order to achieve a sufficient precision for the ²³⁹Pu concentration.

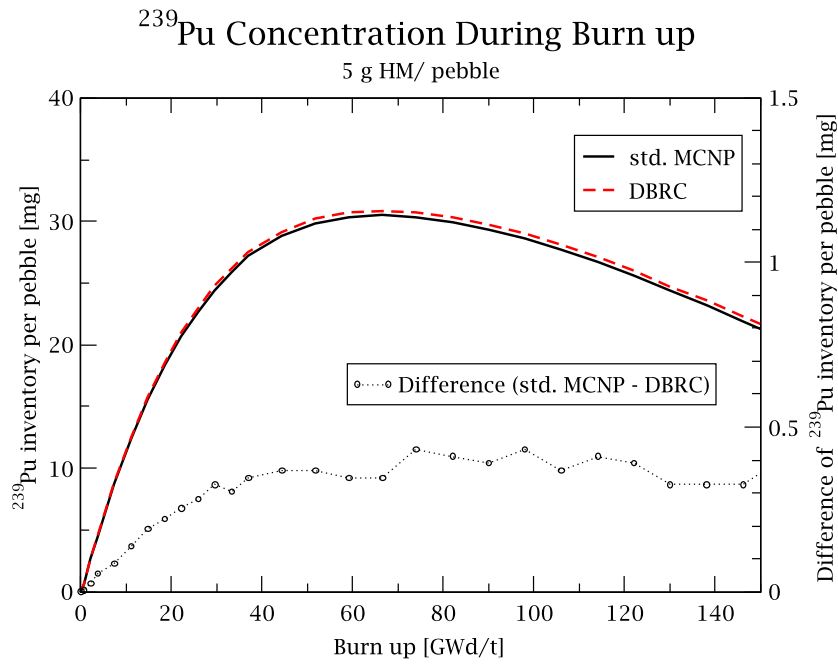


Figure 5.13: ^{239}Pu inventory per pebble during burn up and difference depending on scattering model (5 g HM per pebble case)

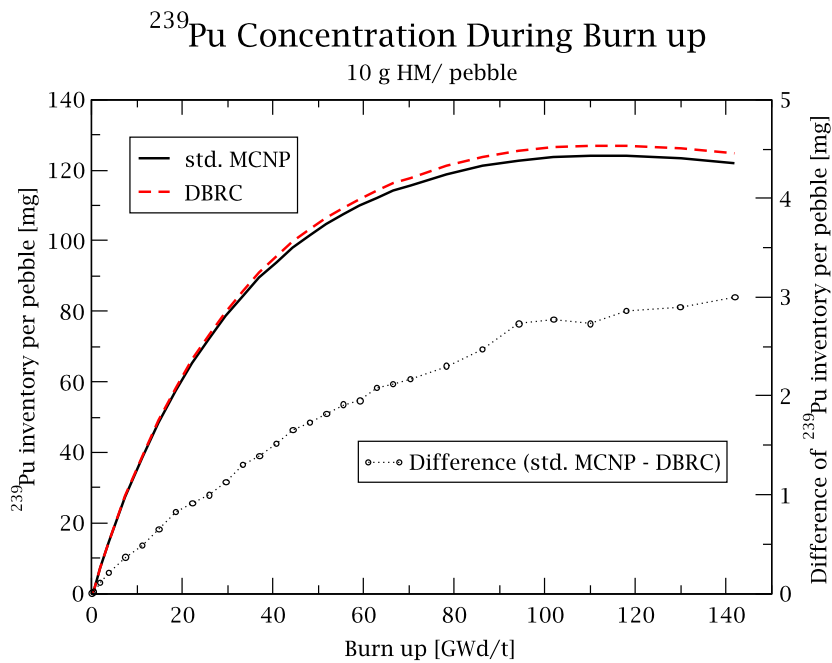


Figure 5.14: ^{239}Pu inventory per pebble during burn up and difference depending on scattering model (10 g HM per pebble case)

Figure 5.13 and 5.14 show the evolution of the ^{239}Pu content per pebble and the difference depending on the scattering treatment for both considered cases of 5 g and 10 g heavy metal per pebble initial loading. The ^{239}Pu concentration at the beginning is zero and increases during burn up due to neutron capture of ^{238}U . A peak concentration depending on the heavy metal content is reached. At this point the production of ^{239}Pu is equal to the its removal by mainly fission. Afterwards the ^{239}Pu concentration decreases again. The decrease of the ^{235}U concentration as main fissile material is compensated by burning ^{239}Pu . Due to a lower ^{235}U content per pebble the peak ^{239}Pu concentration is reached earlier for the case of the lower HM content per pebble. In addition, the peak amount of ^{239}Pu per pebble is higher in the case of higher HM loading per pebble due to a higher flux in the resonance region of ^{238}U . Both cases indicate that the resonance dependent scattering kernel of the DBRC calculation leads to a higher ^{239}Pu build up compared to the standard MCNP calculation. After the high burn up of 140 GWd/t the ^{239}Pu content of the DBRC based calculation is increased of about 2.0 % and 2.4 % compared to std. MCNP calculation for the low and high heavy metal content cases, respectively.

Impact of ^{240}Pu Resonant Scattering Kernel

The plutonium isotope ^{240}Pu is mainly produced by a neutron capture of ^{239}Pu . ^{240}Pu is significantly less fissile than its precursor ^{239}Pu . The ^{240}Pu thermal and epithermal cross section is dominated by capture and elastic scattering. It exhibits, among other resonances, a remarkably large scattering and absorption resonance at 1.056 eV as well as a scattering dominated resonance at 66.2 eV with a Γ_n/Γ_γ ratio of 1.7. Therefore, the impact of the resonance dependent scattering kernel of ^{240}Pu is investigated in this section.

In order to investigate the maximum influence of the resonance dependent scattering kernel of ^{240}Pu a unit cell of a pebble with a high burn up (140 GWd/t) is studied. At this burn up the ^{240}Pu fraction amounts to about 0.55 % of the total actinide vector. Again, DBRC and std. MCNP based criticality calculations are compared.

The sensitivity study shows that the scattering model regarding ^{240}Pu has practically no influence on criticality and neutron flux shape. This is mainly due to the fact that the concentration of ^{240}Pu is very low compared to ^{238}U . In addition, the low energy range, including the 1.056 eV ^{240}Pu -resonance, is dominated by capture. Hence, it is very improbable that a neutron scatters with ^{240}Pu in the vicinity of a resonance and then undergoes a capture by the very same resonance. The lowest resonance with an acceptable ratio of scattering to total cross section is at 66.2 eV. However, this resonance overlaps with the 66.6 eV resonance of ^{238}U . This means that at this energy ^{238}U capture dominates the reaction rates.

Impact of the ^{232}Th Resonant Scattering Kernel

In the seventies and eighties, it was considered to employ a ^{232}Th fuel cycle for an HTR. A fuel cycle based on ^{232}Th can significantly reduce the production of nuclear waste. The build up of higher actinides, especially americium and curium, is strongly reduced due to the lower atomic number. The impact of a resonance dependent scattering kernel of ^{232}Th is investigated based on a pebble unit cell calculation. The analyzed pebble

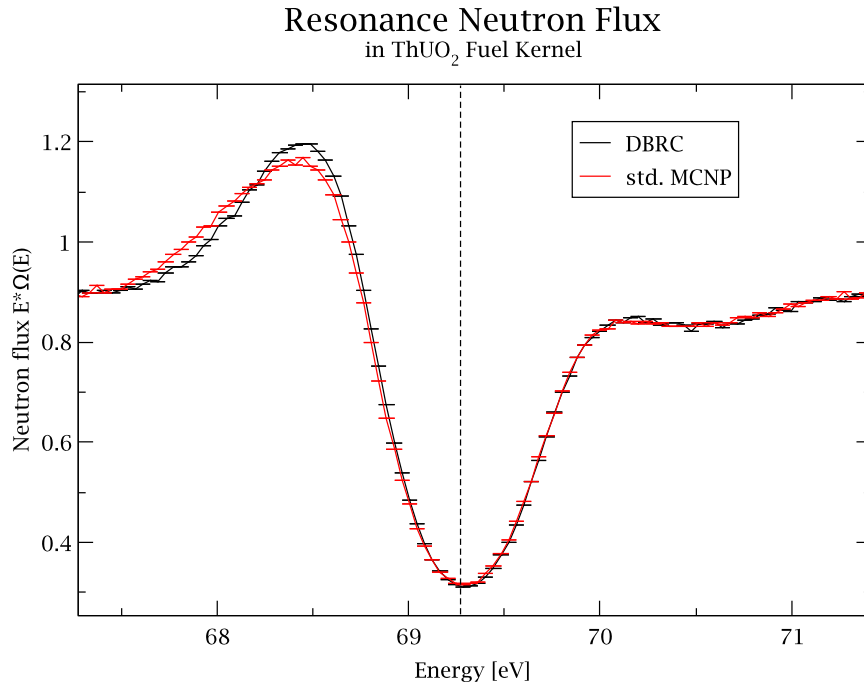


Figure 5.15: Neutron flux in the vicinity of the 69 eV ²³²Th resonance

contains ThUO₂ fuel with 12 g heavy metal. The heavy metal vector consists of 50% fertile ²³²Th and 50% of uranium (93 % enriched ²³⁵U). The TRISO and pebble geometries are the similar to the previous studies. All temperatures are considered to be 1200 K.

The impact of the ²³²Th resonance dependent scattering kernel is small considering the criticality of the unit cell. The shift is only about 0.040 % with a standard deviation (1σ) of $12 \cdot 10^{-5}$. The ²³²Th resonance at 69.2 eV is expected to show the strongest sensitivity on the scattering model due to a high Γ_n/Γ_γ ratio. Nevertheless, the neutron flux in the vicinity of this resonance is only slightly changed by the DBRC introduction.

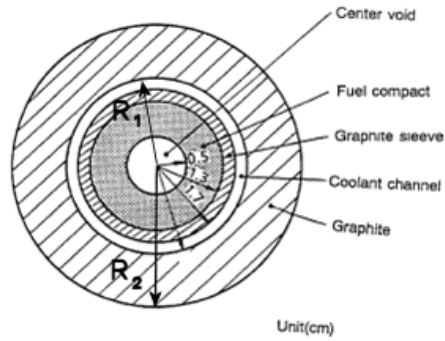


Figure 5.16: HTTR pin cell model^[71]

5.2.3 HTR Fuel Compacts

In this section, the impact of resonance dependent scattering kernel on block type HTRs is investigated. The TRISO matrix studied in section 5.2.1 is inserted into so-called compacts. The fuel design is based on the existing Japanese HTTR design (see 5.1.2). First a pin cell model of the fuel compact is studied, then hexagonal fuel element blocks are investigated.

Criticality of a Pin Cell Model

The HTTR pin cell model of the fuel block is of special interest to study with regard to the impact of the scattering model due to the high TRISO packing factors. Commonly, a one-dimensional pin cell model is used in deterministic codes to determine resonance group cross sections as it is done by Fujimoto et al.^[71] for the HTTR. The model itself represents just one fuel pin with surrounding coolant and graphite layers (see Figure 5.16). The thickness of the graphite layer is chosen according to the relative graphite volume of the hexagonal fuel blocks to one fuel pin. The cross section of the pin cell is therefore the same as the fuel block cross section divided by the number of fuel rods^[71]. Fuel kernels in the fuel compact are arranged in a cubic centered way. The specific TRISO packing factor of the modeled pin is conserved. Axial and radial reflective boundary conditions are applied.

Three different pin cells were investigated:

- Pin cell 1 represents a hexagonal fuel block (layer 1 and fuel zone number 4 of HTTR specifications^[71,69,70]) with a relatively high ²³⁵U enrichment of 9.9 w% and a TRISO packing factor of 29.6 %. The pin cell is based on a fuel block containing 31 fuel pins ($R_1=2.09$ cm, $R_2=3.41$ cm, see Figure 5.16).
- Pin cell 2 represents a fuel assembly (layer 2 and fuel zone 2^[71]) with an enrichment of 6.3 w% and packing factor 29.9 %. The corresponding fuel assembly contains 33 fuel pins ($R_1=2.10$ cm, $R_2=3.52$ cm).
- Pin cell 3 represents a fuel block (layer 3 and zone 1^[71]) with a low enrichment of 4.3 w% and a high packing factor of 30.5 %. The corresponding fuel assemblies contains 33 fuel pins ($R_1=2.10$ cm, $R_2=3.52$ cm).

Table 5.7: Fuel group cross section of HTTR pin cell models for std. MCNP and DBRC based calculations

WIMS group #: Energy range [eV]	pin cell 1			pin cell 2			pin cell 3			
	total	capture	el. scat. [b]	total	capture	el. scat. [b]	total	capture	el. scat. [b]	fission
28: 4.00 - 9.88	17.106	9.538	6.199	16.234	9.173	6.172	15.718	8.949	6.156	0.613
29: 9.88 - 16.0	8.341	1.494	5.593	7.385	1.022	5.558	6.844	0.754	5.539	0.552
30: 16.0 - 27.7	18.024	7.857	8.556	17.007	7.470	8.501	16.451	7.265	8.473	0.713
31: 27.7 - 48.1	19.096	5.296	12.360	18.203	4.961	12.317	17.719	4.781	12.304	0.634
32: 48.1 - 75.5	13.214	3.090	8.773	12.497	2.876	8.757	12.082	2.751	8.740	0.592
33: 75.5 - 149.	13.213	2.641	9.835	12.811	2.505	9.836	12.590	2.433	9.837	0.320
34: 149. - 367.	11.986	1.624	9.739	11.703	1.538	9.768	11.537	1.488	9.777	0.271
tot.	10.229	1.320	6.420	9.493	1.158	6.367	8.960	1.036	6.298	1.501
standard MCNP (sdev.(1 σ): \pm 0.01 b)										
28: 4.00 - 9.88	17.158	9.590	6.202	16.298	9.235	6.177	15.791	9.017	6.161	0.613
29: 9.88 - 16.0	8.339	1.493	5.593	7.386	1.024	5.558	6.843	0.753	5.539	0.552
30: 16.0 - 27.7	18.352	8.093	8.648	17.372	7.733	8.602	16.807	7.521	8.573	0.713
31: 27.7 - 48.1	19.744	5.584	12.731	18.812	5.234	12.661	18.344	5.058	12.657	0.629
32: 48.1 - 75.5	13.237	3.104	8.780	12.522	2.893	8.764	12.113	2.770	8.751	0.592
33: 75.5 - 149.	13.207	2.639	9.833	12.812	2.507	9.836	12.597	2.437	9.839	0.320
34: 149. - 367.	11.975	1.621	9.731	11.696	1.538	9.761	11.518	1.486	9.761	0.272
tot.	10.244	1.330	6.429	9.507	1.167	6.376	8.974	1.045	6.306	1.498
DBRC (sdev.(1 σ): \pm 0.01 b)										
28: 4.00 - 9.88	0.30 %	0.55 %	0.04 %	0.40 %	0.67 %	0.08 %	0.46 %	0.77 %	0.07 %	-0.13 %
29: 9.88 - 16.0	-0.03 %	-0.06 %	0.00 %	0.03 %	0.17 %	0.00 %	-0.02 %	-0.11 %	0.00 %	-0.08 %
30: 16.0 - 27.7	1.82 %	3.01 %	1.07 %	2.14 %	3.53 %	1.20 %	2.16 %	3.52 %	1.18 %	0.02 %
31: 27.7 - 48.1	3.39 %	5.45 %	3.00 %	3.35 %	5.50 %	2.80 %	3.53 %	5.80 %	2.87 %	-0.84 %
32: 48.1 - 75.5	0.17 %	0.47 %	0.09 %	0.20 %	0.61 %	0.09 %	0.25 %	0.72 %	0.13 %	-0.03 %
33: 75.5 - 149.	-0.04 %	-0.09 %	-0.03 %	0.01 %	0.06 %	0.00 %	0.05 %	0.16 %	0.03 %	0.00 %
34: 149. - 367.	-0.09 %	-0.15 %	-0.09 %	-0.06 %	-0.01 %	-0.07 %	-0.16 %	-0.16 %	-0.17 %	0.04 %
tot.	0.14 %	0.73 %	0.14 %	0.15 %	0.83 %	0.14 %	0.16 %	0.86 %	0.12 %	-0.17 %
relative difference (sdev.(1 σ): \pm 0.15 %)										

bold if relative difference > 1 %

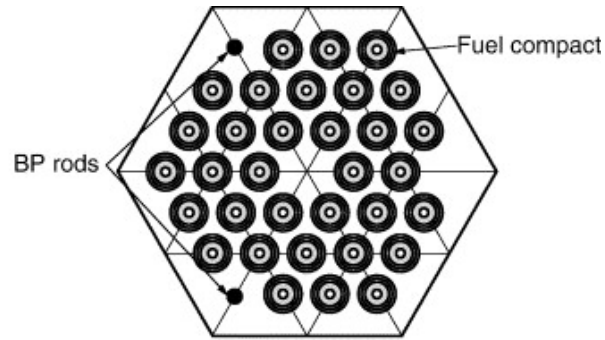


Figure 5.17: HTTR block model (33 pin fuel block)^[71]

The group cross section of the fuel kernels in specific groups of the 69 WIMS group structure^[75] at a temperature of 1200 K is calculated (see table 5.7). The shown groups are the epithermal groups of the lower resonance region from 4 eV to 367 eV. In addition, the one-group cross sections are given. The data are divided into two sets of the total, capture, elastic scattering and fission cross sections for the three considered cases. The first set is based on standard MCNP calculations, the second on DBRC calculations for ^{238}U . The relative difference of the cross sections is given as well. For some groups, especially the groups 28, 30, 31 and 32, the group constants calculated with std. MCNP and the DBRC version differ significantly. For these groups the total, capture and elastic scattering group cross sections are increased by up to 5.8 % when the DBRC scattering model is used instead of the standard MCNP model. The fission group cross section shows only a very small sensitivity to the scattering model. The group cross section is anyhow relatively small in the considered energy range. A difference of the one-group cross sections can merely be noticed for the capture cross section which increases by up to 0.86 %.

Overall, the impact of the scattering model is the largest for pin cell 3 which has the highest TRISO packing factor. This is in accordance to the conclusions of the TRISO packing fraction study of section 5.2.1.

This study shows that if the group constant generation for HTTR is based on pin cell calculations with a constant cross section scattering model, the introduced error for the group cross sections will be non negligible for resonance containing groups. The impact is not solely on the scattering cross section but influences the capture group cross section as well.

Impact of the DBRC Kernel on the Criticality of a Hexagonal Fuel Element

Three different HTTR fuel assemblies are considered which contain the previous studied different fuel compacts as well as burnable poison (BP) rods (see figure 5.17). Hexagonal block 1, 2 and 3 contain the fuel compacts of the pin cells 1, 2 and 3, respectively. The impact of the scattering model on the reactivity of an infinitive array of these fuel blocks at different fuel temperatures is investigated. The fuel temperature is set to 800 K, 1200 K or 1800 K, while the graphite, He-coolant and BP-temperature is always 1200 K.

Table 5.8 gives the multiplication factor k_{∞} for all considered cases and temperatures as well as the relative difference of the multiplication factor dk/k (see equation 5.2). A relatively large difference of the criticality can be noticed for the different enrichments,

Table 5.8: Criticality of a hexagonal block unit cells for different fuel temperatures

	hex. block 1		hex. block 2		hex. block 3	
number of pins	31		33		33	
TRISO p.f.	29.3 %		29.9 %		30.5 %	
²³⁵ U enrichment	9.9 w%		6.3 w%		4.3 w%	
	k_∞	sdev.(1σ) [10 ⁻⁵]	k_∞	sdev.(1σ) [10 ⁻⁵]	k_∞	sdev.(1σ) [10 ⁻⁵]
<i>Fuel Temperature: 800 K</i>						
std. MCNP	1.3372	18	1.20369	17	1.09634	17
DBRC	1.33463	18	1.20073	17	1.09403	17
dk/k [10 ⁻⁵]	-193	25	-247	24	-211	24
<i>Fuel Temperature: 1200 K</i>						
std. MCNP	1.31637	35	1.18285	35	1.07619	35
DBRC	1.31164	35	1.17748	35	1.07163	35
dk/k [10 ⁻⁵]	-361	49	-456	49	-426	49
<i>Fuel Temperature: 1800 K</i>						
std. MCNP	1.29143	34	1.15682	34	1.05272	34
DBRC	1.28415	34	1.14876	34	1.04557	34
dk/k [10 ⁻⁵]	-567	48	-702	48	-684	48

TRISO packing fractions and number of burnable poison rods comparing the different cases. The reactivity shift caused by the resonance dependent scattering kernel increases with temperature as already concluded in the previous studies. Hexagonal blocks 2 and 3 show a higher reactivity shift. These blocks have 33 fuel pins instead of 31 which decreases the overall graphite-to-fuel ratio and therefore increases the flux in the resonance region. The reactivity shift of blocks 2 and 3 are the same with respect to the standard deviations.

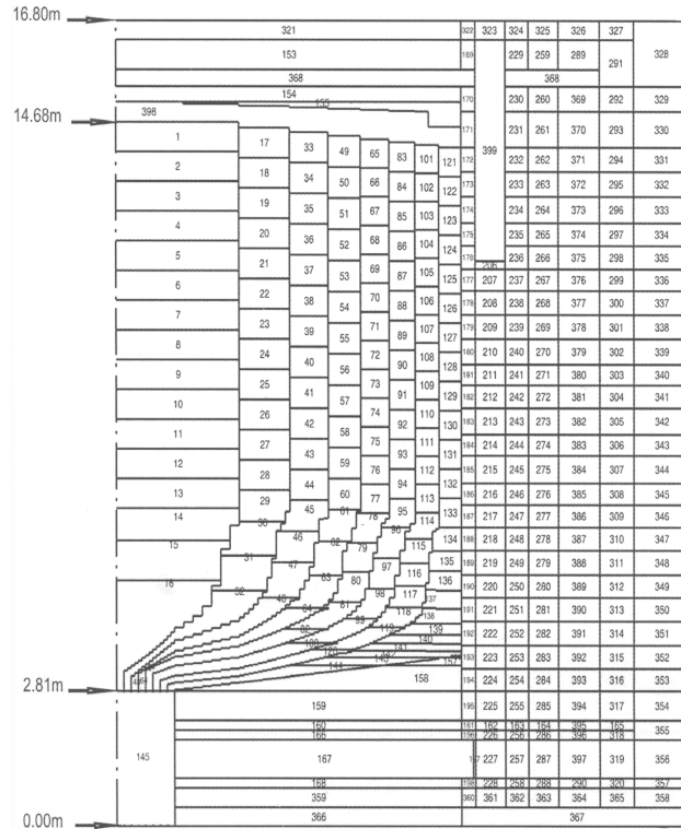


Figure 5.18: Spectral zones of HTR-PM in ZIRKUS

5.3 HTR-PM Core Calculations

A full core model of the Chinese HTR-PM modular reactor is studied with regard to the impact of the resonance scattering treatment. The following calculations are based on a complete MCNP model of the equilibrium core provided by the 'Institut für Kernenergetik und Energiesysteme' (IKE) of the University of Stuttgart, Germany. The equilibrium compositions were produced by the deterministic ZIRKUS code system^[76]. The model consists of 144 spectral fuel zones subdivided into eight radial pebble flow channels (zones 1-144 of figure 5.18). For these fuel zones the equilibrium nuclei composition were determined and converted into a MCNP input by IKE Stuttgart. All control and shutdown systems are fully modeled as well as axial and radial reflectors. In order to simulate the stochastic pebble packing fraction of 61 %, IKE uses equivalence pebbles. These pebbles have an increased radius of the pure graphite which surrounds the TRISO matrix and are cut on six sides to a cubic unit cell. This unit cell has then the theoretical ratio of coolant to pebble volume. TRISO particles are modeled as cubic centred arranged fuel kernels. The four TRISO shells surrounding the fuel kernel are not modeled explicitly but mixed with the matrix graphite. This methodology permits to keep the essential parameters of the double heterogeneity and moderator to fuel and coolant volume while reducing the storage demands and calculation time of the full scale HTR model.

The IKE model is very detailed in the temperature distribution. For every spectral zone fuel, matrix and pebble shell temperatures are given in addition to temperatures of the reflector and shutdown system zones. The fuel temperatures range from 550 K to up to 1150 K. A stochastic interpolation scheme is used in order to approximate the correct

Doppler broadened cross sections at the specific temperatures from a finite temperature grid. The created JEFF3.1 MCNP library contains cross sections for the temperatures 300 K, 400 K, 500 K, 600 K, 700 K, 800 K, 900 K, 1000 K, 1100 K, 1200 K, 1600 K, 1700 K, 1800 K and 2000 K as well as $S(\alpha, \beta)$ tables for graphite at 293 K, 400 K, 500 K, 600 K, 700 K, 800 K, 1000 K, 1200 K, 1600 K and 2000 K. Every nucleus at a specific temperature is then represented by a mixture of two nuclei of the same kind at different node temperatures T_1 and T_2 . The real atomic density of the nucleus is multiplied by the weighting factor w_1 and w_2 . A root interpolation is used as suggested among others by Brown^[77]:

$$\Sigma(T) \approx w_1 \cdot \Sigma_1 + w_2 \cdot \Sigma_2 \quad (5.5)$$

where:

$$w_2 = \frac{\sqrt{T} - \sqrt{T_1}}{\sqrt{T_2} - \sqrt{T_1}} \quad w_1 = 1 - w_2 \quad (5.6)$$

For comparison reasons a linear interpolation scheme is tested as well. The impact of the interpolation scheme on the k_{eff} value is found to be low for the HTR-PM equilibrium core and the used library.

5.3.1 Impact of the DBRC Kernel on the HTR-PM Criticality

Several MCNP calculations are performed using different scattering models. Each calculation simulates about 3,000 cycles with 10,000 neutron histories each in order to achieve a standard deviation (sdev.(1σ)) of the criticality of less than $20 \cdot 10^{-5}$. Table 5.9 summarizes the results of the different cases. The first case (std. MCNP) employs the Wigner-Wilkins approximation for neutrons with an energy of to $E_{up\ scat.} = 400 \cdot k_B T$. Up to this energy an energy transfer from a nucleus to the neutron is possible. At higher energies the asymptotic 0 K scattering kernel is used. This option is defined as the reference case. The range of the Wigner-Wilkins approximation is extended to 210 eV, 500 eV and 1000 eV for cases 2 to 4 (WW₂₁₀, WW₅₀₀, WW₁₀₀₀). Case 5 (0 K approx.) uses the Wigner-Wilkins approximation for the thermal range and starts at 4 eV to employ the 0 K approximation. This procedure is commonly used by deterministic codes. Cases 6, 7 and 8 (DBRC₂₁₀, DBRC₅₀₀, DBRC₁₀₀₀) employ the resonance dependent scattering

Table 5.9: Criticality of the HTR-PM reactor with different scattering models

	Scat. model	$E_{up\ scat.}$	k_{eff}	sdev.(1σ) [10^{-5}]	$k_x - k_{std.MCNP}$ [10^{-5}]	sdev.(1σ) [10^{-5}]
1	std. MCNP	$400 \cdot k_B T$	1.00281	9	–	–
2	WW ₂₁₀	210 eV	1.00245	13	-36	16
3	WW ₅₀₀	500 eV	1.00232	13	-49	16
4	WW ₁₀₀₀	1000 eV	1.00260	14	-21	17
5	0 K approx.	4 eV	1.00176	17	-105	19
6	DBRC ₂₁₀	210 eV	1.00084	9	-197	13
7	DBRC ₅₀₀	500 eV	1.00106	16	-175	18
8	DBRC ₁₀₀₀	1000 eV	1.00074	13	-207	16
9	DBRC ₂₁₀ (²³⁸ U + ²⁴⁰ Pu)	210 eV	1.00088	14	-193	17

kernel for ^{238}U and the Wigner-Wilkins approximation for other nuclei up to an energy of 210 eV, 500 eV and 1000 eV. The DBRC₂₁₀ MCNP version has been used as standard DBRC version in the previous studies. Case 9 (DBRC₂₁₀ ($^{238}\text{U} + ^{240}\text{Pu}$)) uses the DBRC₂₁₀ model for both, ^{238}U and ^{240}Pu .

Extending the range of the Wigner-Wilkins approximation has a small impact on k_{eff} . A decrease of up to 0.050 % (ca. 3σ) can be noticed. The use of the DBRC scattering kernel for ^{238}U however, decreases the criticality by about -0.20 %. Again, extending the up scattering range from 210 eV to 1000 eV shows little impact. The main contribution of the reactivity shift lies within the first 8 main S resonances of ^{238}U . Even though ^{240}Pu cross section has a pronounced resonance profile and in particular a strong resonance at the low energy of 1.056 eV the impact of a resonance dependent scattering model is low. This is due to the relative low concentration of ^{240}Pu compared to ^{238}U .

Case 5 shows a clear reactivity decrease as well. In this case the 0 K approximation is used in the entire resonance region. Using the asymptotic kernel instead of Wigner-Wilkins kernel leads to an increased down-scattering of neutrons from the higher energy side of ^{238}U resonances towards the resonance energies. Consequently the neutron absorption increases.

5.3.2 Impact of the DBRC Kernel on the HTR-PM Doppler Reactivity Coefficient

The impact of the resonance dependent scattering kernel on the calculation of the Doppler reactivity coefficient of the HTR-PM is studied. For this the fuel temperatures in the different spectral fuel zones are uniformly changed by a fixed temperature difference ΔT e.g. all fuel temperatures are increased by 100 K. Criticality calculations are performed with the standard and DBRC (for ^{238}U) versions of MCNP and the reactivity ρ is calculated (equation 5.4). Figure 5.19 shows the reactivities for fuel temperature changes of -300 K to 500 K for both scattering models. At $\Delta T = 0$ the calculated reference reactivity is slightly positive due to a criticality value k_{eff} larger than one. Third order polynomials are fitted by regression to the reactivity values:

$$\begin{aligned}\rho_{std.MCNP}(\Delta T) [10^{-5}] &= -8.578 \cdot 10^{-7} \Delta T^3 + 1.7304 \cdot 10^{-3} \Delta T^2 - 4.751 \Delta T + 266.3 \\ \rho_{DBRC}(\Delta T) [10^{-5}] &= -9.719 \cdot 10^{-7} \Delta T^3 + 1.7934 \cdot 10^{-3} \Delta T^2 - 5.023 \Delta T + 89.0\end{aligned}$$

where ΔT is given in Kelvin. There is clear reactivity difference over the entire considered temperature range which increases for higher temperatures. The derivations of the equations $\rho_{std.MCNP}(\Delta T)$ and $\rho_{DBRC}(\Delta T)$ gives the reactivity coefficients for both cases. They are plotted in figure 5.20. The Doppler reactivity coefficient based on the DBRC calculation is always found to be more negative than the one based on the standard MCNP calculation. At the equilibrium temperature distribution ($\Delta T=0$ K) the difference between the different calculations is at least 6 % and up to 8 % for higher temperature differences ΔT .

A more negative Doppler reactivity coefficient increases the inherent shutdown feedback due to a fuel temperature rise and therefore the safety of the reactor. However, the increase Doppler feedback has to be overcome during normal shut down of the reactor core. The calculated reactivity gain due to the temperature decrease is higher when the resonance dependent scattering kernel is considered. Therefore, stronger shut down rods

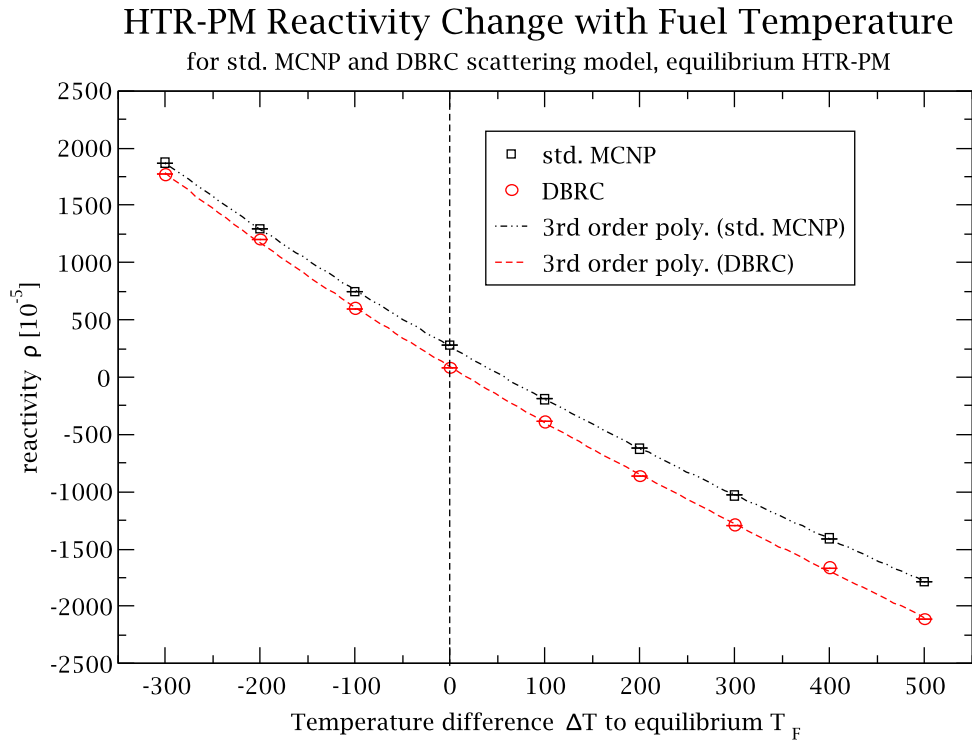


Figure 5.19: Reactivity of the HTR-PM equilibrium core at different fuel temperatures calculated with DBRC and std. MCNP

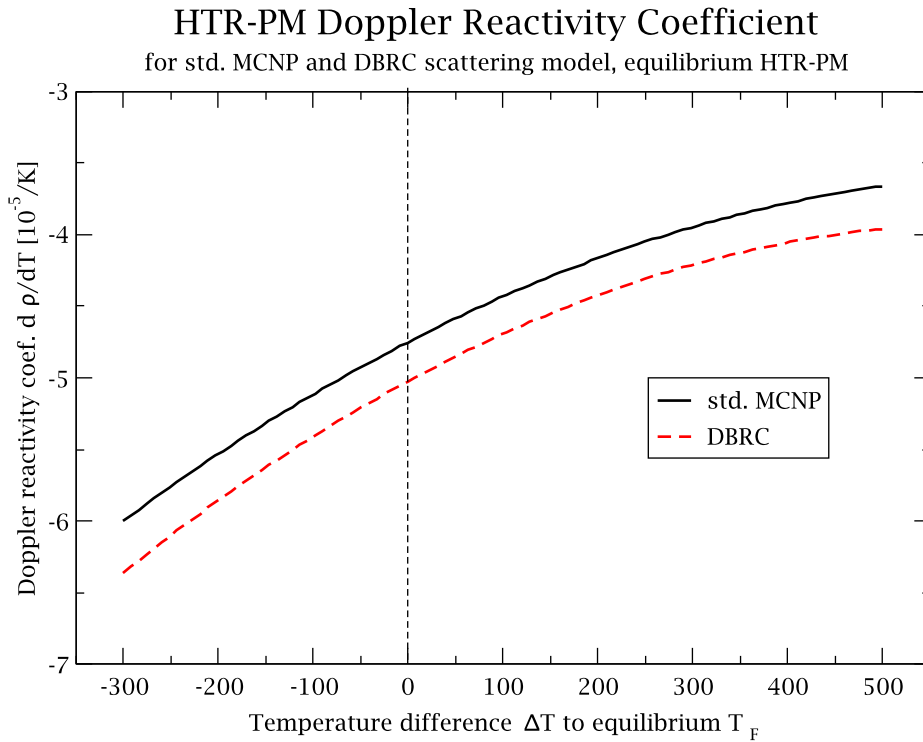


Figure 5.20: Doppler reactivity coefficient of the HTR-PM equilibrium core at different fuel temperatures calculated with DBRC and std. MCNP

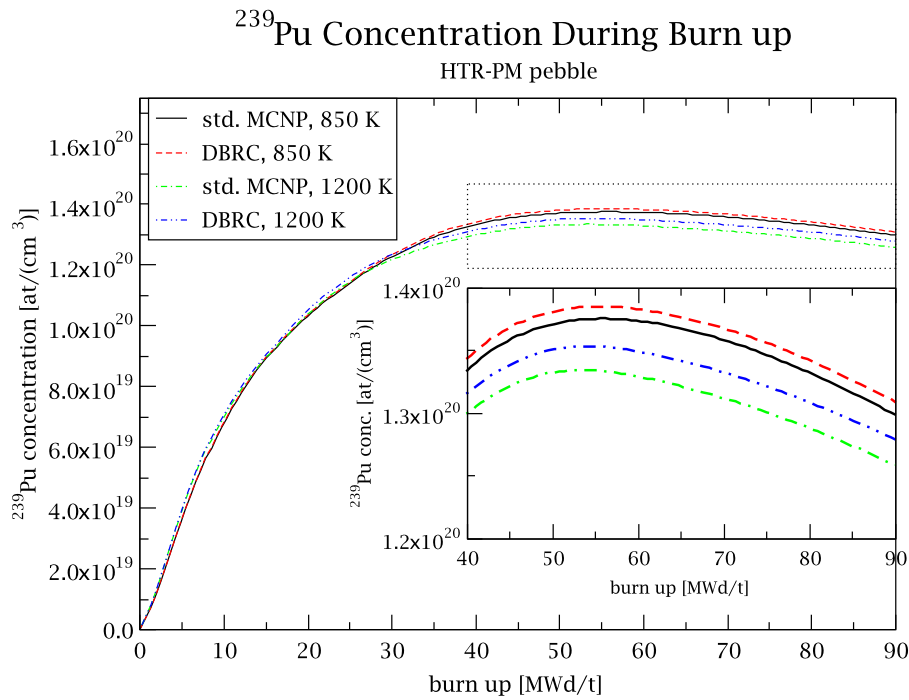


Figure 5.21: ^{239}Pu concentration during burn up of HTR-PM unit cell for different fuel temperatures calculated with the DBRC and with the standard. MCNP versions

are required or the final shut down temperature has to be increased.

5.3.3 Estimation of the Criticality Shift due to Higher ^{239}Pu Content

As mentioned in the previous unit cell studies (see section 5.2.2), the increased neutron absorption of ^{238}U leads to a higher ^{239}Pu production during burn up. The studied HTR-PM equilibrium core however is based on deterministic ZIRKUS calculations. Therefore the equilibrium compositions used previously does not include the effect of a resonance dependent scattering kernel for ^{238}U . This means that the ^{239}Pu equilibrium concentration is not exact. In this subsection, an estimate of the additional ^{239}Pu concentration is determined based on a unit cell burn up study.

The considered unit cell consists of BCC arranged pebbles. One half of the pebbles have an equilibrium composition while the other half are fresh pebbles. The equilibrium pebbles are mixed to the fresh pebbles to create an approximate HTR-PM equilibrium neutron spectrum. During burn up only the fresh pebbles changed their fuel composition while the equilibrium pebbles keep their initial composition.

The highest neutron flux in the core appears in the spectral zones 8 and 9 (see figure 5.18). Therefore, the equilibrium composition is chosen to be the same as in zone 9. Two different cases are considered. In the first case, the fuel, matrix and pebble shell temperatures are taken as of zone 9. The fuel temperature is 850 K. A special cross section set at this temperature is created in order to avoid interpolation by means of material mixing which would lead to an effective temperature change during burn up. In a second case, the fuel temperature is 1200 K. This case is deemed to give the maximum realistic

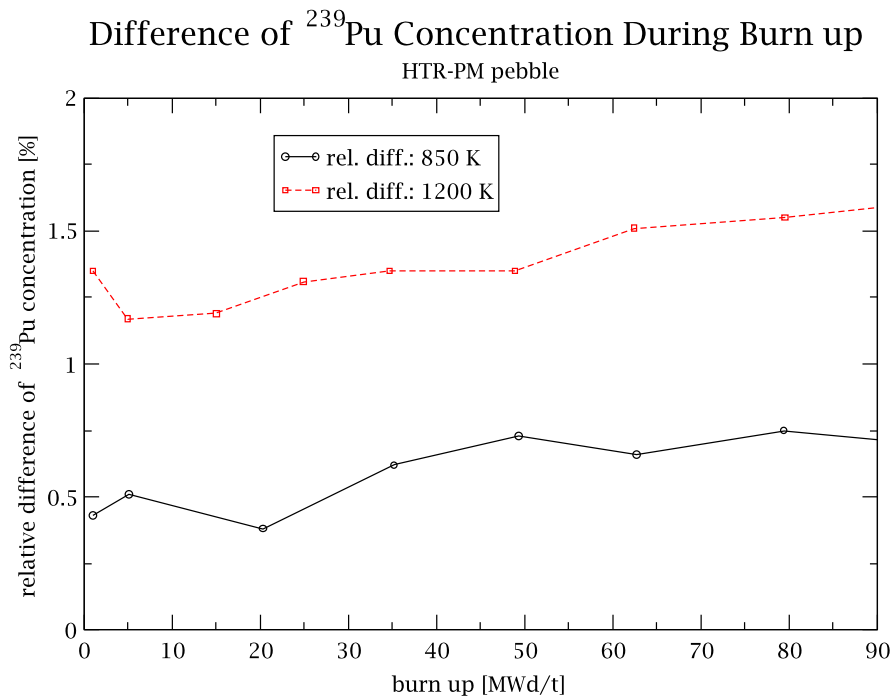


Figure 5.22: Increase of the ^{239}Pu concentration calculated with DBRC relative to standard MCNP calculation for an HTR-PM unit cell and different fuel temperatures

impact of the resonance dependent scattering kernel on HTR-PM ^{239}Pu concentration.

Figure 5.22 shows the ^{239}Pu concentration in the initially fresh TRISO kernels during burn up based on standard MCNP and DBRC calculations as well as the relative difference. Both studied cases are shown. The relative difference on the ^{239}Pu concentration between the std. MCNP and DBRC based calculations is significantly higher for the higher fuel temperature case. The difference at mid burn up of 45 MWd/t HM is about 1.5 % and 0.75 % for the 1200 K and 850 K, respectively. In order to investigate the impact of the DBRC kernel on the mean ^{239}Pu content the ^{239}Pu concentration is intergarted over the entire 90 MWd/tHM burn up. A differene of 0.66 % and 1.45 % is found for the first and second case, respectively.

The ^{239}Pu concentration in every spectral zone of the HTR-PM core model is increased by 0.66 % and 1.45 % in order to investigate whether the additional ^{239}Pu compensates the reactivity loss due to the resonance dependent scattering model compared to the standard MCNP model. Table 5.10 gives the criticality k_{eff} of the core for the different cases. The additional ^{239}Pu content in the pebbles increses k_{eff} to some extent. However,

Table 5.10: Criticality of the HTR-PM core with additional ^{239}Pu

Case	k_{eff}	sdev.(1 σ)[10 ⁻⁵]	$k_{DBRC}-k_{std.MCNP}$ [10 ⁻⁵]	sdev.(1 σ)[10 ⁻⁵]
std. MCNP	1.00281	9	–	–
DBRC	1.00084	9	-197	13
DBRC + 0.66 % ^{239}Pu	1.00139	14	-142	17
DBRC + 1.45 % ^{239}Pu	1.00188	13	-93	16

even with 1.45 % more ^{239}Pu , there is still a reactivity decrease between the standard MCNP calculation to the DBRC calculation with the additional ^{239}Pu .

5.4 Summary

The presented study of this chapter shows that the resonance dependent scattering kernel should be included in reactor physics calculation for HTR pebble bed reactors and in particular for block type HTRs. The error introduced by using an approximated model of the ^{238}U scattering kernel, like the asymptotic kernel or the Wigner-Wilkins kernel, can be significant for criticality and Doppler reactivity calculations. With these approximated kernels the breeding of ^{239}Pu by neutron capture of ^{238}U is systematically underestimated.

Conclusion and Outlook

Conclusion

The presented work concentrates on the mutual effect of nuclear cross section resonances and temperature influence, i.e. Doppler broadening, on the double differential part of the scattering cross section, namely the scattering kernel and on its subsequent influence on high temperature reactors. These two underlying phenomena of resonances and temperature dependence of cross section were discussed and common analytical formula were given.

The new code *DOPPLER-MC* was developed and is presented in this work. *DOPPLER-MC* performs stochastically Doppler broadening of cross sections as well as scattering kernels. In particular *DOPPLER-MC* takes the resonance shape of cross sections into account when the scattering kernel is concerned. The cross section Doppler broadening method of *DOPPLER-MC* is compared to the state-of-the-art Doppler broadening method of the NJOY code. Both codes produce exactly the same temperature dependent cross sections. The resonance dependent kernel broadening method of *DOPPLER-MC* is compared to the analytic equations given by Rothenstein and Dagan^[2]. The stochastic broadened kernel agrees very well with analytic broadened kernel in terms of the energy transfer as well as of the angular distribution of scattered neutrons.

As a direct consequence of the stochastic *DOPPLER-MC* code, a stochastic, resonance dependent scattering kernel broadening module (DBRC) is implemented into the MC transport code MCNP as suggested by Rothenstein^[3]. The DBRC method removes the current blatant inconsistency within MCNP, using Doppler broadened resonance cross sections but neglecting the resonances as far as the scattering kernel is concerned. This method represents an alternative to the use of $S(\alpha, \beta)$ tables by introducing the resonance scattering model into the MC code. Significant differences between the current MCNP model and the improved DBRC model are pointed out by comparing energy transfers, up- and down-scattering probabilities, energy moments, mean energy change, angular moments and the mean cosine of the scattering angle.

The new DBRC model is validated by two experiments: the nTOF capture experiment and in particular the RPI scattering experiment. In addition, DBRC based calculations are compared to $S(\alpha, \beta)$ based MCNP calculations. The $S(\alpha, \beta)$ tables are produced by using the analytic formula for the resonance dependent kernel. Criticality and reaction rates of the DBRC and $S(\alpha, \beta)$ calculation agree within the statistical uncertainty. It is concluded that a sufficient high degree of validation of the DBRC scattering model is reached.

The impact of the resonance dependent scattering kernel on HTRs is studied in detail. The DBRC corrected version of MCNP is employed. The HTR models used in this study are mainly based on the HTR-10, the HTTR and the HTR-PM. It is found that in

cell-calculations the importance of the scattering model in the resonance region of ^{238}U increases with increasing the TRISO packing factor (TPF) and a temperature increasing. Neutron flux deviations in the very vicinity of the resonance energy can be observed when the DBRC model is considered causing a negative reactivity shift. The shift is mainly caused by an increased neutron absorption of the 20.87 eV and 36.7 eV ^{238}U resonances.

A similar dependency on the heavy metal loading, i.e. on the TPF, and on the temperature is observed for pebble unit cell calculations. In addition, the Doppler reactivity coefficient is found to be more negative when the DBRC model is considered, especially for higher heavy metal content pebbles. Pebble burn up studies show that the increased neutron absorption of ^{238}U leads to a higher ^{239}Pu concentration at high burn up rates. The impact of the ^{232}Th scattering kernel model is investigated, but found to be low.

For the compact design, similar results are obtained as for the pebble design. However, due to the high TPF of the compact, the influence of the resonance dependent scattering kernel increases. For example, if an HTTR compact-pin-cell-model is used for group cross section generation, the total and the absorption group cross section are subject to an error of up to 5.8 %.

Finally, a full scale model of the HTR-PM core is analyzed in view of the impact of the resonance scattering kernel. When the DBRC model is used instead of the standard MCNP scattering model the reactivity decreases by about -0.20 %. The ^{239}Pu content of the equilibrium core increases by up to 1.45 %. However, the additional amount of ^{239}Pu does not compensate the loss of reactivity. In addition, the DBRC kernel renders the Doppler coefficient being more negative by about 6 to 8 %.

Outlook

The resonance dependent scattering kernel model should not only be included in MC codes but also in deterministic codes like it was already accomplished in case of the well known commercial code CASMO^[34].

In the very first step, namely the interpretation of time-of-flight experiments for cross section generation, data analyse codes (e.g SAMMY^[53], REFIT^[78], CONRAD^[79]) are used. They perform the cross section fitting based on various formalisms to the experimental measurements. However, the multiscattering models used by these codes, are based on the zero Kelvin approximation. It is evident that the basic cross section evaluation should also be based on the present resonance dependent model. In particular, Aerts^[51] showed that in the case of a ^{232}Th saturated resonances the code SAMMY fails to match the resonance shape which is attributed to the approximative multiscattering model.

A first step towards this achievement could be to integrate a DBRC like correction into a Monte Carlo code performing the multiple scattering correction for the data analysis code. The second step should consequently be to deduce an analytical correction of the current multiscattering treatment, based on the new DBRC version of MCNP presented in this work.

Bibliography

- [1] M. Ouisloumen and R. Sanchez. A model for neutron scattering off heavy isotopes that accounts for thermal agitation effects. *Nuclear Science and Engineering*, Vol. 107(3):189–200, 1991. ISSN 0029-5639.
- [2] W. Rothenstein and R. Dagan. Ideal gas scattering kernel for energy dependent cross-sections. *Annals of Nuclear Energy*, Vol. 25(4-5):209–222, March 1998. ISSN 0306-4549.
- [3] W. Rothenstein. Neutron scattering kernels in pronounced resonances for stochastic Doppler effect calculations. *Annals of Nuclear Energy*, Vol. 23(4-5):441–458, March 1996. ISSN 0306-4549.
- [4] R. Dagan. On the use of $s(\alpha, \beta)$ tables for nuclides with well pronounced resonances. *Annals of Nuclear Energy*, Vol. 32(4):367–377, March 2005. ISSN 0306-4549.
- [5] W. Rothenstein. Proof of the formula for the ideal gas scattering kernel for nuclides with strongly energy dependent scattering cross sections. *Annals of Nuclear Energy*, Vol. 31(1):9–23, 2004. ISSN 0306-4549.
- [6] Gen4. A technology roadmap for generation IV nuclear energy systems. Technical Report GIF-002-00, U.S. DOE Nuclear Energy Research Advisory Committee and the Generation IV International Forum, 2002.
- [7] G. I. Bell and S. Glasstone. *Nuclear Reactor Theory*. Van Nostrand Reinhold, 1970. ISBN 0442206844.
- [8] W. M. Stacey. *Nuclear Reactor Physics*. Wiley-VCH, 2 edition, July 2007. ISBN 3527406794.
- [9] F. H. Fröhner. Evaluation and analysis of nuclear resonance data. Technical Report, Nuclear Energy Agency, OECD Data Bank, 2000. JEFF Report 18.
- [10] J. E. Lynn. *The theory of neutron resonance reactions*. English. Clarendon P., (Oxford), 1968. ISBN 70379613.
- [11] H. A. Bethe. Theory of disintegration of nuclei by neutrons. *Physical Review*, Vol. 47(10):747, May 1935.
- [12] E. Vogt. Resonance theory of neutron cross sections of fissionable nuclei. *Physical Review*, Vol. 112(1):203, October 1958.
- [13] A. Koning, R. Forrest, M. Kellett, R. Mills, H. Henriksson, and Y. Rugama. The JEFF - 3.1 Nuclear Data Library. Technical Report, 2006. JEFF Report 21.

-
- [14] *JANIS 3.0 User's Guide*. NEA Data Bank OECD, June 2007.
- [15] N. Bohr. Neutron capture and nuclear constitution. *Nature*, Vol. 137(3461):344–348, 1936. ISSN 0028-0836.
- [16] L. Meitner and O. R. Frisch. Disintegration of uranium by neutrons: A new type of nuclear reaction. *Nature*, Vol. 143:239–240, 1939.
- [17] N. Bohr and J. A. Wheeler. The mechanism of nuclear fission. *Phys. Rev.*, Vol. 59: 426 – 450, 1939.
- [18] J. J. Duderstadt and L. J. Hamilton. *Nuclear Reactor Analysis*. John Wiley & Sons, Inc, 1987.
- [19] A. M. Lane and R. G. Thomas. R-matrix theory of nuclear reactions. *Rev. Mod. Phys.*, Vol. 30(2):257–353, Apr 1958.
- [20] N. M. Larson. Introduction to the theory and analysis of resolved (and unresolved) neutron resonances via SAMMY. Lecture given at the Workshop on Nuclear Data and Nuclear Reactors: Physics, Design and Safety LNS015001, Oak Ridge National Laboratory, Oak Ridge, TN, USA, Trieste, April 2000.
- [21] M. Herman. *ENDF- 6 Formats Manual*. Brookhaven National Laboratory, 2005. BNL-NCS-44945-05-Rev.
- [22] E. E. Lewis. *Fundamentals of Nuclear Reactor Physics*. Academic Press, February 2008. ISBN 0123706319.
- [23] M. M. R. Williams. *Slowing Down and Thermalization of Neutrons*. North-Holland Pub. Co., 1966. ISBN 0720401011.
- [24] D. E. Cullen and C. R. Weisbin. Exact Doppler broadening of tabulated cross sections. *Nuclear Science and Engineering*, Vol. 60:199–229, 1976.
- [25] RSICC. *NJOY99.0 - Code System for Producing, Pointwise and Multigroup Neutron and Photon Cross Sections from ENDFB Data*. Oak Ridge National Laboratory, Oak Ridge, TN, USA, 2000. PSR-480/NJOY99.0.
- [26] E. P. Wigner and J. E. J. Wilkins. Effect of the temperature of the moderator on the velocity distribution of neutrons with numerical calculations for H as moderator. Technical Report AECD-2275, Oak Ridge National Laboratory, Oak Ridge, TN, USA, September 1944.
- [27] G. L. Blackshaw and R. L. Murray. Scattering function for Low-Energy neutron collisions in a Maxwellian monoatomic gas. *Nuclear Science and Engineering*, Vol. 27:520–532, 1967.
- [28] A. Y. Kurchenkov and N. I. Laletin. Neutron-scattering indices at moving monoatomic-gas nuclei in the resonant energy region. *Atomic Energy*, Vol. 70(6): 451–457, June 1991.

- [29] O. Bouland, V. Kolesov, and J. L. Rowlands. The effect of approximations in the energy distributions of scattered neutrons on thermal reactor Doppler effects. In *Proceedings of the international conference nuclear data for science and technology. Volume 2*, Gatlinburg, TN (United States), December 1994. American Nuclear Society, Inc., La Grange Park, IL (United States).
- [30] R. Dagan and W. Rothenstein. The contribution of upscattering by heavy nuclides to the Doppler effect. In *Proceedings of the ICENES meeting - International Conference on Emerging Nuclear Energy Systems*, Herzlia, Israel, June 1998.
- [31] A. Kurchenkov and V. Sidorenko. Estimating changes in the Doppler effect in correcting for nuclear thermal motion and the resonant behavior of the scattering cross section in the scattering indicatrix. *Atomic Energy*, Vol. 82(4):313–315, April 1997.
- [32] H. Tellier, M. Coste, C. Raepsaet, and C. V. D. Guth. Heavy nucleus resonant absorption calculation benchmarks. *Nuclear Sciences and Engineering*, Vol. 113: 23–30, 1993.
- [33] R. Dagan and C. Broeders. On the effect of resonance dependent scattering-kernel on fuel cycle and inventory. In *Proceedings of the PHYSOR-2006 meeting*, Vancouver, Canada, September 2006.
- [34] D. Lee, K. Smith, and J. Rhodes. The impact of ²³⁸U resonance elastic scattering approximations on thermal reactor Doppler reactivity. *Annals of Nuclear Energy*, Vol. 36(3):274–280, April 2009. ISSN 0306-4549.
- [35] P. Oberle. *Application of a new resonance formalism to Pressurized Water Reactors*. PhD thesis, Universität Stuttgart, (to be published).
- [36] R. Dagan. A consistent formalism for the neutron scattering source term of the Boltzmann transport equation, May 2008. Habilitationsschrift Universität Stuttgart IKE 6-203.
- [37] X.-. M. C. Team. *MCNP - A General Monte Carlo N-Particle Transport Code, Version 5*. LANL, 2003. LA-UR-03-1987.
- [38] M. S. Milgram, R. Dagan, and B. Becker. Rate of convergence of antithetic transforms in Monte Carlo simulation. In *Proceedings of the International Conference on Mathematics, Computational Methods & Reactor Physics (M&C 2009)*, Saratoga Springs, New York, May 2009.
- [39] M. S. Milgram. On the use of antithetic variates in particle transport problems. *Annals of Nuclear Energy*, Vol. 28(4):297–332, March 2001. ISSN 0306-4549.
- [40] J. F. Briesmeister. *MCNP - A General Monte Carlo N-Particle Transport Code, Version 4C*. LANL, 2000. LA-13709-M.
- [41] D. B. Pelowitz. *MCNPX Users Manual - Version 2.6.0*. LANL, 2008. LA-CP-07-1473.
- [42] *MONK*. Serco, 2001. ANSWERS/MONK/REPORT/005.

- [43] J. Leppaenen. *PSG2 Serpent - a Continuous-energy Monte Carlo Reactor Physics Burnup Calculation Code*. VTT, 2009.
- [44] R. Y. Rubinstein and D. P. Kroese. *Simulation and the Monte Carlo Method*. Wiley & Sons, 2 edition, February 2008. ISBN 0470177942.
- [45] W. E. Lamb. Capture of neutrons by atoms in a crystal. *Physical Review*, Vol. 55 (2):190, 1939.
- [46] S. W. Lovesey. *Theory of Neutron Scattering from Condensed Matter: Nuclear Scattering: 1*. Clarendon Press, new edition edition, October 1986. ISBN 019852028X.
- [47] Y. Danon, E. Liu, D. Barry, T. Ro, and R. Dagan. Benchmark experiment of neutron resonance scattering models in Monte Carlo Codes. In *Proceedings of the International Conference on Mathematics, Computational Methods & Reactor Physics (M&C 2009)*, Saratoga Springs, New York, May 2009. American Nuclear Society, Inc., La Grange Park, IL (United States).
- [48] Y. Danon, R. C. Block, N. Francis, M. Lubert, M. Rapp, F. Saglime, R. Bahrn, C. Romano, J. Thompson, D. P. Barry, N. J. Drindak, J. G. Hoole, G. Leinweber, and M. Ernesti. Cross section measurements and analysis at Rensselaer: Report to CSEWG november 2008, 2008. Brookhaven National Laboratory, New York.
- [49] T. Ro, Y. Danon, E. Liu, D. P. Barry, and R. Dagan. Measurements of the neutron scattering spectrum from ^{238}U and comparison of the results with a calculation at the 36.68-eV resonance. *Journal of Korean Physical Society*, Vol. 55(4):1389 –1393, October 2009.
- [50] Y. Danon and R. Dagan. personal communication. 2009.
- [51] G. Aerts. *Mesure de la section efficace de capture neutronique du ^{232}Th à n_{TOF} au CERN*. PhD thesis, Université Paris XI Orsay, 2005.
- [52] F. Gunsing. personal communication. 2009.
- [53] N. M. Larson. *Updated Users' Guide for SAMMY: Multilevel R-Matrix Fits to Neutron Data Using Bayes' Equations*. Oak Ridge National Laboratory, Oak Ridge, TN, USA, October 2008.
- [54] G. Noguere. *Mesures et analyses des sections efficaces neutroniques totales et de capture radiatives des iodes 127 et 129 de 0.5 eV à 100 keV*. PhD thesis, Université Louis Pasteur, 2009.
- [55] Geant4 international collaboration. *Geant4: Physics Reference Manual*, December 2008.
- [56] D. Porsch, U. Hesse, W. Zwermann, and W. Bernnat. Spezifikation eines DWR-Brennelementes, UO₂ (4 w/o U-235) 18 x 18 -24, für Vergleichsrechnungen. Technical Report, AAA User-Group Workshop, Garching, Germany, 2004.
- [57] J. Bouchard and R. Bennett. Generation IV advanced nuclear energy systems. *Nuclear Plant Journal*, Vol. 26(5):2–4, Sep 2008. ISSN 0892-2055.

- [58] K. Kugeler and R. Schulten. *Hochtemperaturreaktortechnik*. Springer-Verlag GmbH, May 1992. ISBN 3540515356.
- [59] G. Lohnert, H. Nabielek, and W. Schenk. The fuel element of the HTR-module, a prerequisite of an inherently safe reactor. *Nuclear Engineering and Design*, Vol. 109 (1-2):257–263, September 1988. ISSN 0029-5493.
- [60] Y. Xu and K. Zuo. Overview of the 10 MW high temperature gas cooled reactor–test module project. *Nuclear Engineering and Design*, Vol. 218(1-3):13–23, October 2002. ISSN 0029-5493.
- [61] S. Shiozawa, S. Fujikawa, T. Iyoku, K. Kunitomi, and Y. Tachibana. Overview of HTTR design features. *Nuclear Engineering and Design*, Vol. 233(1-3):11–21, October 2004. ISSN 0029-5493.
- [62] Z. Zhang, Z. Wu, D. Wang, Y. Xu, Y. Sun, F. Li, and Y. Dong. Current status and technical description of Chinese 2 x 250 MWth HTR-PM demonstration plant. *Nuclear Engineering and Design*, Vol. 239(7):1212–1219, July 2009. ISSN 0029-5493.
- [63] G. Lohnert. Technical design features and essential safety-related properties of the HTR-module. *Nuclear Engineering and Design*, Vol. 121(2):259–275, July 1990. ISSN 0029-5493.
- [64] W. Steinwarz and X. Yuanhui. Status of design of the HTR test module China. *Nuclear Engineering and Design*, Vol. 121(2):317–324, July 1990. ISSN 0029-5493.
- [65] X. Jing, X. Xu, Y. Yang, and R. Qu. Prediction calculations and experiments for the first criticality of the 10 MW high temperature gas-cooled Reactor-Test module. *Nuclear Engineering and Design*, Vol. 218(1-3):43–49, October 2002. ISSN 0029-5493.
- [66] Z. Wu, D. Lin, and D. Zhong. The design features of the HTR-10. *Nuclear Engineering and Design*, Vol. 218(1-3):25–32, October 2002. ISSN 0029-5493.
- [67] Y. Yang, Z. Luo, X. Jing, and Z. Wu. Fuel management of the HTR-10 including the equilibrium state and the running-in phase. *Nuclear Engineering and Design*, Vol. 218(1-3):33–41, October 2002. ISSN 0029-5493.
- [68] M. Ogawa and T. Nishihara. Present status of energy in Japan and HTTR project. *Nuclear Engineering and Design*, Vol. 233(1-3):5–10, October 2004. ISSN 0029-5493.
- [69] M. Goto, N. Nojiri, and S. Shimakawa. Neutronics calculations of HTTR with several nuclear data libraries. *Journal of Nuclear Science and Technology*, Vol. 43 (10):1237–1244, 2006. ISSN 0022-3131.
- [70] T. K. Kim, T. A. Taiwo, and F. Szakaly. Evaluation of the high temperature engineering test reactor (HTTR) start-up experiments. Technical Report ANL-GenIV-059, Argonne National Laboratory, Argonne, 2005.
- [71] N. Fujimoto, N. Nojiri, H. Ando, and K. Yamashita. Nuclear design. *Nuclear Engineering and Design*, Vol. 233(1-3):23–36, October 2004. ISSN 0029-5493.

-
- [72] H. Reutler and G. Lohnert. Advantages of going modular in HTRs. *Nuclear Engineering and Design*, Vol. 78(2):129–136, April 1984. ISSN 0029-5493.
- [73] H. Reutler and G. H. Lohnert. Der modulare HTR - Ein neues Konzept für den Kugelhaufenreaktor. *Atomwirtschaft*, Vol. 27, January 1982.
- [74] J. S. Hendricks, G. W. McKinney, M. L. Fensin, M. R. James, R. C. Johns, J. W. Durkee, J. P. Finch, D. B. Pelowitz, L. S. Waters, M. W. Johnson, and F. X. Gallmeier. *MCNPX 26F Extensions*. LANL, 2008. LA-UR-08-1808.
- [75] B. Dodd, S. Basu, S. Paranjpe, and A. Trkov. WIMS-D LIBRARY UPDATE. Technical Report, International Atomic Energy Agency, Vienna, 2007.
- [76] W. Bernnat and W. Feltes. Models for reactor physics calculations for HTR pebble bed modular reactors. *Nuclear Engineering and Design*, Vol. 222(2-3):331–347, June 2003. ISSN 0029-5493.
- [77] F. B. Brown. The 2005 Frederic Joliot / Otto Hahn Summer School: Monte Carlo Advances & Challenges, 2005. Karlsruhe, Germany.
- [78] M. C. Moxon, T. C. Ware, and C. J. Dean. *REFIT-2007 A Least-Square Fitting Program for Resonance Analysis of Neutron Transmission, Capture, Fission and Scattering Data Users' Guide for REFIT-2007-08*, August 2007.
- [79] C. D. S. Jean, B. Habert, O. Litaize, G. Noguere, and C. Suteau. Status of CONRAD, a nuclear reaction analysis tool. In *ND2007*, Nice, France, 2008.

Nomenclature

Symbol	Unit	
A		mass number
A_k		energy moment
E	eV	neutron energy
E'	eV	secondary neutron energy
E_0	eV	resonance energy
E_B	eV	binding energy
E_T	eV	target energy
E^*	eV	excitation energy
$\langle E - E' \rangle_{av}$	eV	mean energy loss
$f(\vec{\Omega})$	$n/cm^{-2}/s$	neutron vector flux in direction $\vec{\Omega}$
g_c		spin factor
I		target spin quantum number
J		the total spin quantum number
k_B	eV/K	Boltzmann constant ($8.617343 \cdot 10^{-5} eV/K$)
k_∞		infinite multiplication factor
k_{eff}		effective multiplication factor
l		wave moment
m	kg	neutron mass
$M^T(V)$		Maxwell Boltzmann distribution
P_n		Legendre polynomial
$P(C, \mu_T)$		SVT probability density function
$p(V)$		velocity distribution of the target nuclei
R	cm	radius of the target nucleus
s		channel spin quantum number
T	K	temperature
T_F	K	fuel temperature
u	m/s	neutron velocity in the COM frame
u'	m/s	secondary neutron velocity in the COM frame
U	m/s	target velocity in the COM frame
U'	m/s	secondary target velocity in the COM frame
U_{cc}		collision matrix (S matrix)
v	m/s	neutron speed in the LAB frame
v_r	m/s	relative neutron speed in the TR frame
α_{TF}^D	K^{-1}	Doppler reactivity coefficient
Γ_x	eV	partial resonance width
λ_c	nm	de Broglie wave length of the neutron
μ_0		cosine of the scattering angle in the laboratory frame

μ_C		cosine of the scattering angle in the center-of-mass frame
μ_0^{TR}		cosine of the scattering angle in the target-at-rest frame
μ_t		cosine of the angle between incident neutron and target in the laboratory frame
$\bar{\mu}_0^{lab}$		mean cosine of the scattering angle
ϑ	<i>deg</i>	polar scattering angle
ρ		reactivity
σ_x	<i>b</i>	cross section of reaction type x
σ_{sn}	<i>b</i>	Legendre moment of scattering cross section
$\sigma_s(E \rightarrow E')$	<i>b/eV</i>	energy transfer scattering kernel from energy E to E'
$\sigma_s(E \rightarrow E', \vec{\Omega} \rightarrow \vec{\Omega}')$	<i>b/eV</i>	double differential scattering kernel from energy E to E' and from direction $\vec{\Omega}$ to $\vec{\Omega}'$
Σ_x	<i>cm⁻¹</i>	macroscopic cross section of reaction type x
φ	<i>deg</i>	azimuthal scattering angle
Φ	<i>n/cm²/s</i>	neutron flux
ξ		dimensionless neutron speed
$\psi + i\chi$		complex resonance shape function
$\vec{\Omega}$		angular direction

Institut für Kernenergetik und
Energiesysteme

Universität Stuttgart

Pfaffenwaldring 31

D-70550 Stuttgart

